Theoretical investigations of nuclear quantum effects in weakly bonded metal-molecular interfaces

Dissertation

zur Erlangung des akademischen Grades

Doctor rerum naturalium

(Dr. rer. nat.)

im Fach Physik: Theoretische Physik

eingereicht an der

Mathematisch-Naturwissenschaftlichen Fakultät der

Humboldt-Universität zu Berlin

von

Herrn M. Sc. Karen S. Fidanyan

Präsidentin der Humboldt-Universität zu Berlin:

Prof. Dr. Julia von Blumenthal

Dekanin der Mathematisch-Naturwissenschaftlichen Fakultät:

Prof. Dr. Caren Tischendorf

Gutachter/innen:

1. Prof. Dr. Caterina Cocchi
2. Dr. Mariana Rossi
3. Prof. Dr. Denis Usvyat

Datum der Einreichung: 5. Oktober 2022

Datum der mündlichen Prüfung: 25. November 2022

Acknowledgements

"Are Heracles and Jesus brothers?"

---

me, 3 y.o., seeking for the Theory of Everything. 24 years before this thesis.

Looking back at the path which led me to this point, I sometimes ask myself, whether I was a subject or an object of this development. There is no doubt that I was lucky with the people around me. Starting from my parents, who sacrificed so much of their everyday comfort in order to not just "grow" me and my brothers, but to give us as much as they could in all regards. If I asked a question, they would never send me away without an answer. Then, the school. Who knows Russian school, knows that choosing a job of a teacher means a lot of sacrifice as well. And yet, so many bright people took this path to give kids, including me, their chance in life. It would take the whole page to mention all the teachers that I'm grateful to, so I restrict the list to accurate sciences. In mathematics, to which I never expressed much talent, first Elena A. Korolyova† taught me to respect math even if I can't do it well, and the difference between "knowing how to solve" a problem and actually solving it. Then, during the STEM-oriented high school and bachelor, where my below-average math skills were obvious, every teacher I came across was patient enough to guide me through, and delicate enough to not embarrass me with my quite often failures. I am especially thankful to Vladimir D. Krylov†, Natalia V. Kruglova, Sergey A. Belyaev and Nazar Kh. Agakhanov. In physics, I acknowledge very pictorial and lively seminars of Yuriy P. Tsargorodtsev and Eduard M. Hohlov, and bright lectures of Andrey V. Gavrikov and Aleksey A. Abrikosov, Jr. I thank my computer science teacher Elena A. Karpunina for making me believe that programming is easy and fun. I thank Prof. Genri E. Norman who introduced me to the field of atomistic simulations and to the spirit of academia in general, and Dr. Vladimir V. Stegailov who supervised my work in Moscow and told me many things which took me quite some time to digest.

I'd like to thank the young fellows of the FHI and MPSD theory departments for all the good time we had and for lots of discussions which exposed me to cultures all around the globe. Thanks to Nathaniel, Yair, Haiyuan, Xiaojuan, Alaa, Alan, Eszter

and Paolo for being such a joyful and supportive team. Thanks Dmitrii Maksimov, Nikita Rybin, Nikita Kuldyushev and Galina Kuldyusheva for making sure that I don't spend holidays home alone.

Finally, I'd like to express my deep gratitude to Mariana: for guiding this work, motivating me, caring about us as persons and not just "labor", and for shielding me from the winds that arose recently.

Hamburg, September 2022 *K. F.*

Zusammenfassung

Schwach gebundene Grenzflächen, bei denen die Bindung zwischen einem Substrat und einem Adsorbat durch van-der-Waals-Kräfte und andere nicht-kovalente Wechselwirkungen bestimmt wird, kommen in einer Vielzahl von Anwendungen vor, von der Katalyse bis zu metallorganischen elektronischen Vorrichtungen, und sind ein Gegenstand umfangreicher experimenteller und theoretischer Forschung. In solchen Systemen beeinflussen die Wechselwirkungen zwischen den kollektiven Eigenschaften der Oberfläche, z. B. die Abschirmung von langreichweitigen Dispersionswechselwirkungen und der Ladungstransfer zwischen einem Metall und adsorbierten Molekülen, das Verhalten des Systems erheblich, und man muss diese Effekte in theoretischen Modellen berücksichtigen, um interessante Eigenschaften, die sowohl mit der nuklearen als auch der elektronischen Struktur zusammenhängen, korrekt zu modellieren. Aufgrund der ausgeprägten anharmonischen Bereiche in der potentiellen Energieoberfläche und der hohen Mobilität der Moleküle an solchen Grenzflächen tragen sowohl thermische als auch Quantenfluktuationen der Kerne zu deren Gleichgewichtseigenschaften bei. Trotz jahrzehntelanger theoretischer Untersuchungen ist es nach wie vor eine Herausforderung, über einfache Modelle wie die harmonische Näherung für die Bewegung der nuklearen Freiheitsgrade oder das Slab-Modell für eine Oberfläche hinauszugehen. Sie erfordert die neuesten und oft rechenintensiven Simulationstechniken, was hohe Anforderungen an die Software-Infrastruktur und die Rechenressourcen stellt.

In dieser Dissertation diskutiere ich theoretische Methoden zur Simulation von Grenzflächen zwischen Metallen und Molekülen auf atomarer Maßstabsebene, die für die Speicherung und Erzeugung ßauberer Energie von Bedeutung sind, und wende sie an. Wir verwenden die Dichtefunktionaltheorie für das elektronische Subsystem und verschiedene Methoden wie die (quasi-)harmonische Näherung und die Pfadintegral-Molekulardynamik, um die Quanteneigenschaften des nuklearen Subsystems zu berücksichtigen und zu bestimmen, welche Methoden ausreichen, um die wesentlichen Phänomene zu erfassen und gleichzeitig rechnerisch erschwinglich zu bleiben.

Wir berechnen den Isotopeneffekt auf die Arbeitsfunktion von Cyclohexan, das an der Rh(111)-Oberfläche adsorbiert wird, ein Effekt, der sich aus der Elektron-Phonon-Kopplung nur dann ergibt, wenn die nuklearen Freiheitsgrade quantenmechanisch be-

handelt werden. Deuteriertes Cyclohexan C_6D_{12} hat einen größeren Adsorptionsabstand als gewöhnliches Cyclohexan. Pfadintegral-Molekulardynamiksimulationen zeigen auch eine temperaturabhängige Renormierung der elektronischen Zustandsdichte in diesem System, die sowohl durch thermische als auch durch Quantenfluktuationen der Kerne verursacht wird.

Schließlich befassen wir uns mit Oberflächenreaktionen auf einer geladenen metallischen Oberfläche. Wir stellen unsere Implementierung der Nudged-Elastic-Band-Methode (NEB) im i-PI-Paket vor und diskutieren ihre Leistungsfähigkeit. Anschließend setzen wir die Methode ein, um die Energiebarriere der Wasserspaltungsreaktion auf einer Pd(111)-Oberfläche zu berechnen, die einem elektrischen Feld unterschiedlicher Intensität ausgesetzt ist. Wir zeigen, dass die niedrigste Dissoziationsbarriere auftritt, wenn das Feld eine Stärke erreicht, die eine geometrische Frustration des auf der Oberfläche adsorbierten Wassermoleküls hervorruft, und dass die Nullpunktenergiebeiträge zur Barriere dieser Reaktion über den weiten Bereich der auf das System angelegten elektrischen Feldstärken nahezu konstant bleiben. Wir erklären dies durch eine gegenseitige Aufhebung der Rot- und Blauverschiebungen einzelner Schwingungsmoden zwischen Reaktant und Übergangszustand.

Abstract

Weakly bound interfaces, in which the bonding between a substrate and an adsorbate is determined by van der Waals forces and other non-covalent interactions, appear in a vast range of applications, from catalysis to metal-organic electronic devices, and are a subject of extensive research, both experimental and theoretical. In such systems, the interplay between the collective properties of the surface, e.g. the screening of long-range dispersion interactions and the charge transfer between a metal and adsorbed molecules, affect the behavior of the system substantially, and one has to account for these effects in theoretical models to correctly model interesting properties, related both to nuclear and electronic structure. Due to the pronounced anharmonic regions in the potential energy surface and the high mobility of molecules in such interfaces, both thermal and quantum fluctuations of nuclei contribute to their equilibrium properties. Despite decades of theoretical investigation, it is still challenging to go beyond simple models such as the harmonic approximation for the motion of nuclear degrees of freedom or the slab model for a surface. It requires the most recent and often computationally expensive simulation techniques, thus posing high demands to both software infrastructure and computational resources.

In this thesis, I discuss and apply theoretical methods for simulating interfaces between metals and molecules of relevance to "clean" energy storage and production on an atomistic scale. We use density-functional theory for the electronic subsystem and various methods such as (quasi-)harmonic approximation and path integral molecular dynamics to account for quantum properties of the nuclear subsystem, determining which methods are sufficient to grasp the essential phenomena while remaining computationally affordable.

We calculate isotope effect on the work function of cyclohexane adsorbed on Rh(111) surface, an effect that emerges from electron-phonon coupling only when the nuclear degrees of freedom are treated quantum-mechanically. Deuterated cyclohexane C_6D_{12} has larger adsorption distance than ordinary cyclohexane. Path integral molecular dynamics simulations also show a temperature-dependent renormalization of the electronic density of states in this system, induced by both thermal and quantum fluctuations of nuclei.

Finally, we address surface reactions on a charged metallic surface. We present our implementation of the nudged elastic band (NEB) method in i-PI package and discuss its performance. We then employ the method to calculate the energy barrier of water splitting reaction on a Pd(111) surface subjected to electric fields of different strengths. We show that the lowest dissociation barrier takes place when the field reaches a strength that induces a geometric frustration of the water molecule adsorbed on the surface, and that the zero-point energy contributions to the barrier of this reaction remain nearly constant across the wide range of electric field strengths applied to the system. We explain this by a mutual cancellation of the red and blue shifts of individual vibrational modes between reactant and transition states.

Contents

Acronyms

AI-PIMD *ab initio* path integral molecular dynamics. x, 61, 63, 68, 69, 83, 84, 86, 87, 88, 91, 92, 111, 112

AIMD *ab initio* molecular dynamics. x, 68, 83, 84, 86, 87, 88, 91, 92

BFGS Broyden–Fletcher–Goldfarb–Shanno. x, 52, 57

BO Born-Oppenheimer. x, 10, 11, 36

CI-NEB climbing-image nudged elastic band. x, xix, 51, 102, 103, 104, 127

DFT density-functional theory. x, 4, 5, 11, 15, 23, 29, 31, 35, 53, 58, 59, 63, 65, 83, 87, 89, 128

DOF degree of freedom. x, 28, 37, 38, 53

DOS density of states. x, xix, 97, 99, 100

ESM effective screening medium. x, xiii, 28, 29, 92

FBZ first Brillouin zone. x, 23

GCSCF grand-canonical self-consistent field. x, 5, 29

GF Green's function. x, 4, 5, 30, 31, 108, 113, 129

GGA generalized gradient approximation. x, 14, 15

GLE Generalized Langevin eqiation. x, 41, 42, 68

HA harmonic approximation. x, 5, 6, 63, 71, 77, 108

HEG homogeneous electron gas. x, 14

HOMO highest occupied molecular orbital. x, 100

HSE06 Heyd–Scuseria–Ernzerhof-2006. x, xvi, 4, 65, 66, 73, 74, 75, 76, 78, 121

KS-DFT Kohn-Sham density-functional theory. x, 20, 25, 31, 35, 129, 130

LDA local density approximation. x, 14, 15

LEED low energy electron diffraction. x, 2, 63

LZK Lifshitz-Zaremba-Kohn model. x, 21

MBD many-body dispersion. x, 21, 22, 23, 24

MBD@rsSCS many-body dispersion with range-separated self-consistent screening. x, 23

MC Monte-Carlo. x, 40

MD molecular dynamics. x, xvii, xviii, 4, 6, 40, 41, 42, 43, 56, 68, 82, 83, 84, 85, 92, 108

MEP minimal-energy path. x, xiv, 49, 50, 51, 52, 53

NEB nudged elastic band. viii, x, xiv, xv, xix, xx, xxi, 49, 50, 51, 52, 53, 54, 55, 56, 57, 58, 59, 102, 103, 113, 126, 127, 128

nl-MBD non-local many-body dispersion. x, xvi, 65, 73, 74, 75, 121

NQE nuclear quantum effects. x, 63, 108

PBC periodic boundary conditions. x, 33

PBE Perdew–Burke-Ernzerhof. x, xvi, xviii, xx, xxiii, 14, 15, 16, 65, 66, 69, 70, 73, 74, 75, 76, 78, 79, 83, 93, 97, 98, 104, 105, 120, 121

PES potential energy surface. x, 38, 48, 54, 62, 83, 113

PIGLET path integrals with generalized Langevin equation. x, 42, 68

PIMD path integral molecular dynamics. x, xvii, xviii, 6, 40, 41, 42, 43, 65, 68, 69, 82, 83, 84, 85, 86, 88, 112

PL principal layer. x, 30, 128, 129

QH quasi-harmonic. x, 77, 79, 82

QHA quasi-harmonic approximation. x, 5, 61, 86, 87, 88, 111

QHO quantum harmonic oscillator. x, 24, 41, 42

SCF self-consistent field. x, xiii, 4, 20, 28, 29, 31, 58, 78, 92, 129

SFG sum-frequency generation spectroscopy. x, 2

SIE self-interaction error. x, 15

SL-RPC spatially localized ring polymer contraction. x, xiv, 43, 44, 63, 69, 84, 86, 89, 112, 117, 118

STM scanning tunneling microscopy. x, 63

TPD temperature-programmed desorption. x, xxiii, 70, 71

TST transition state theory. x, 47, 49

UPS ultraviolet photoemission spectroscopy. x, 62, 87

vDOS vibrational density of states. x, 71, 105

vdW van der Waals. x, xvi, 20, 73, 74, 75, 78, 89, 97, 104

XC exchange-correlation. x, 4, 14, 15, 16, 20, 23, 65, 73, 78, 93, 104, 112

ZPE zero point energy. x, xv, xvi, xx, xxiii, 37, 62, 67, 70, 71, 74, 75, 77, 78, 79, 87, 104, 105, 107, 108, 112

List of Figures

List of Tables

Chapter 1

Introduction

```
writeln('Hello World!');
```

me, 14 years before writing this thesis

1.1 Molecular physics of surfaces

Surface systems and, more particularly, weakly bound interfaces constitute a vast range of technologically important molecular systems, from catalysts [11, 12] to metal-organic junctions in electronic devices [13]. A class of surface-adsorbate systems is so interesting for technological applications because it offers high tunability: by tuning the molecules adsorbed on a surface, one gets access to a continuous spectrum of different electronic properties, such as work function, band gap etc [14, 15]. Stacking multiple layers increases the potential of such an approach even more. The term "weakly bound" in this context means that the main contribution to the surface-molecule bonding comes from the van der Waals and dipole-dipole interactions, in contrast to strong covalent or ionic interactions. Researchers studying heterogeneous catalysis base their development on the assumption that the ability both to activate a reactant molecule (i.e. to adsorb it and to modify its electronic structure) and to release later desired products of a chemical reaction defines a good catalyst. In such a context, "weak" bonding may be stronger than just van der Waals attraction. Metal-organic bonds typically involve a certain amount of electron transfer. However, bonds must be still much weaker than actual covalent bonding in order to release reaction products and

prevent poisoning of a catalyst. It has been known for a long time that platinum group metals (ruthenium, rhodium, palladium, osmium, iridium, and platinum itself) are good catalysts for various reactions [16, 17]. Although they find applications in large-scale industrial processes [18], such as the catalytic conversion of car exhaust gases, their high cost limits their use and motivates researchers to look for more affordable compounds with similar properties.

Both aforementioned technological fields are similar in their need to control precisely the structure and properties of an interface system, because both electronic properties and reaction chains are sensitive to fairly small changes in the geometry of an adsorbate. Theoretical simulation plays an important role in this field, because it gives unique resolution and helps to link molecular structure to existing experimental techniques. Development in surface-specific methods such as sum-frequency generation spectroscopy (SFG) [19, 20, 21], diffraction and energy loss spectroscopy of low-energy electrons (LEED/HREELS) [22] and scanning techniques (tunneling and atomic-force microscopy) pave ever broader ways for such research, and all of those methods benefit from theoretical support to match the experimental results with the actual structure of an investigated system. Most of the aforementioned methods deal with very clean setups under ultra-high vacuum conditions, which in the case of catalysts imposes a problem known as a "pressure gap": industrial catalytic processes occur at pressures of at least one atmosphere and higher, and reactive surfaces behave differently in such conditions [23]. In some cases, the methods based on X-ray adsorption, namely extended X-ray absorption fine structure (EXAFS) and near edge structure (XANES) can be applied at ambient pressure to overcome this [24], but they lack atomistic resolution and surface specificity and give only an averaged picture across the sample. SFG allows measurements in ambient conditions, but it is unclear whether its surface specificity remains in all interesting cases – for example, applying an electric field would break the central symmetry of the bulk liquid, especially if it consists of polar molecules like water [25]. At the same time, computer simulation allows modeling surfaces at ambient gas pressure [26] or in contact with a liquid [27, 28, 29], therefore providing a unique (to date) access to atomistic resolution in "difficult" environments.

From a computational point of view, the investigation of surface-adsorbate systems

by electronic structure methods is a relatively difficult task for a number of reasons specific to this kind of systems. One of the reasons is the strict necessity to have commensurate periodic structures for a substrate and an adsorbate to fit the system into a simulation box – even if they are incommensurate or very large-scale commensurate in nature[1], which often leads to large unit cells containing many hundreds of atoms. Simulation of an isolated adsorbate or a clean substrate typically requires much smaller unit cells. Another difficulty is related to a correct description of a surface: being neither an isolated cluster system nor periodic in all 3 dimensions, a surface does not fit seamlessly into the well-established methods of quantum chemistry. In most of the existing electronic-structure codes, the only way to simulate a surface is to approximate it with a slab which is periodic in two lateral dimensions and is isolated by vacuum from both sides in the third dimension, which, however, has to have periodic boundary conditions because of the software's architecture. Since a vacuum appears on both sides of a slab, it effectively has two surfaces, which increases the number of atomic layers needed to approximate a real surface.

To make the task even more difficult, weakly bound interfaces often demonstrate high mobility of molecules and highly anharmonic vibrational behavior. In the domain of applicability of the harmonic approximation for nuclear fluctuations, one can rely on well-established and fairly inexpensive computational techniques. Beyond this domain, one has to choose between performing very expensive dynamical simulations and building approximations.

1.2 State of the art

1.2.1 Electronic structure theory

Electronic structure simulations of surfaces started decades ago, and the basic concepts how to treat surfaces were established by the late 80s and early 90s. The main three directions (arranged by increasing complexity) are a) to set up an isolated in vacuum cluster large enough to capture some features of a surface; b) to extend the existing machinery of periodic bulk simulations in order to mimic a surface; and c) to describe

[1]For example, cyclohexane may form a $(2\sqrt{79} \times 2\sqrt{79})R17.0^\circ$ pattern on a Rh(111) surface[30].

a surface as a periodic semi-infinite bulk, which can be calculated in surface Green's function formalism, and an interface region where periodicity breaks. The cluster model is more of historical interest and is used mostly in cases where periodic boundaries are inaccessible for technical reasons (e.g. some techniques are not implemented for a periodic case in a particular code), or in order to benchmark new codes against older calculations. The other two models are actively developed.

The slab model is a working horse of surface simulations and with the currently available computational resources, it allows running long molecular dynamics (MD) simulations or using highly accurate hybrid exchange-correlation (XC) functionals such as Heyd–Scuseria–Ernzerhof-2006 (HSE06) [31] for fairly complex adsorbates [32]. Inclusion of potential bias in the slab model has no commonly used "default" approach so far, although a number of approximations were proposed and successfully applied [33, 3, 4, 34, 5, 35]. Different implementations of density-functional theory (DFT) make different approaches preferential. For example, packages with localized basis sets, such as FHI-aims [36] and SIESTA [37, 38], have a much lower computational penalty for the increase of the vacuum layer compared to plane-wave codes, therefore it is much easier to decouple periodic repetitions of the slab. The implementation effort on top of existing DFT codes varies for different models from nearly zero to rewriting the self-consistent field (SCF) procedure, the Poisson equation solver, etc. A very promising direction is a grand-canonical SCF with explicitly non-periodic boundary condition along the surface-perpendicular direction[5].

Electronic Green's function (GF) methods have the advantage of giving access to non-equilibrium properties such as electron transport [39] and have a naturally grand-canonical formulation. Although employed more than 30 years ago [40, 41, 42, 43], they did not earn as wide recognition as slab techniques, probably because of higher computational cost and somewhat excessive capabilities for many applications. Only recently GF implementations were incorporated smoothly in versatile *ab initio* packages [44, 45], although some implementations were available since early 2000s [46, 47, 48]. Finally, to my view, GF implementations (at least the openly available ones which I have tried) still suffer from technical problems which severely limit their applicability for diverse systems.

Although it is hard to predict the direction of scientific development, from my experience I would expect that more explicit and direct techniques, i.e. grand-canonical self-consistent field (GCSCF) or GF, will prevail over peculiarly constructed systems such as a doped electrode made of fictitious atoms (e.g. [34]), despite their higher implementation difficulty. They will prevail not because of their higher quality or efficiency, but rather because once implemented properly, they reduce the effort needed to set up the system and the number of external parameters to construct a desired molecular system. A more detailed discussion of the inclusion of potential bias in DFT simulations is given in the section 2.6.

1.2.2 Nuclear motion

For the nuclear subsystem, the current state of theory is also very advanced. A vast range of relevant systems is covered by the (quasi-) harmonic approximation (HA and QHA) for both thermodynamic and kinetic properties. Well-established models such as Eyring transition state theory [49, 50] or its adaptation for solids [51] give computationally inexpensive ways to calculate reaction rates. As an extension for harmonic approximation (HA), one can include phonon-phonon coupling by adding the 3rd order term to the Taylor expansion of energy [52]. Since HA and 3rd order expansion give access to many properties analytically, one can try to stretch this approach to the limit and to map anharmonic forces obtained from molecular dynamics onto an effective temperature-dependent harmonic potential, as proposed by Hellman, Abrikosov *et al.* [53, 54]. This approach may help to deal with systems that are dynamically stabilized at elevated temperatures, such as the BCC phase of zirconium or uranium [55, 56]. In the last decades, the frontier in this field has moved towards "badly behaving" systems, where models based on the harmonic approximation perform poorly. In fact, weak bonds almost certainly imply anharmonicity, therefore van-der-Waals-bound systems such as molecular crystals or physisorbed interfaces attract more and more attention as methodology improves [57, 58, 59, 32, 60, 61]. An accurate description of dispersion interactions is crucial to get accuracy in the binding energy of such systems [62]. VdW binding defines not only thermodynamical properties such as adsorption energy, but electronic properties of an interface as well: low-frequency vibrations

couple to the electronic levels and affect charge transfer, work function and other electronic properties which are relevant for applications [14, 13]. For a long time, pairwise semi-empirical van der Waals models stemming from the famous London's work [63] were the only viable option [64, 10], but recent advances in deriving non-local models paved the way to higher accuracy [65, 66, 67]. I discuss models for dispersion interactions in more detail in section 2.5. For such anharmonic systems, static methods such as (Q)HA are not sufficient anymore, and molecular dynamical simulations become necessary to sample their corrugated potential energy surface. One can calculate thermodynamical observables as well as some dynamical properties, such as power spectrum, straightforwardly, the only hurdle is the necessity to simulate long trajectories to get statistically converged results. Somewhat more difficult are reaction rates: for the majority of relevant chemical reactions, the barriers are high enough to make simple MD prohibitively expensive. In such case, one has to use methods of enhanced dynamics, such as Metadynamics, replica exchange and others [68, 69, 70, 71]. However, the aforementioned MD methods treat nuclei as classical particles and miss quantum contribution to thermodynamical, which in many cases is decisive. A well-known example of a quantum effect in an adsorption process is the different desorption energies between isotopologues, which are the result of the different zero-point energy of vibrations. Inclusion of quantum statistics into MD simulations is possible via path integral techniques which were introduced into the field by Rahman and Parrinello in 1984 [72] and gained some popularity since then [73, 74, 75, 76]. Compared to classical MD, path integral molecular dynamics (PIMD) is around another order of magnitude (or more) more expensive. I discuss these methods in detail in section 3.1.2.

1.3 Overview of the thesis

I give a more detailed description of the methods that we used for electronic and nuclear subsystems in Chapters 2 and 3, respectively. As one can see from the short review above, for both electrons and nuclei there are ladders[2] of approximations, the next steps of which promise higher accuracy, but at a higher price, and often *much* higher.

[2]Related to the electronic problem, people often call it the "Jacob's ladder" [77].

In this sense, the effort of a modern researcher can be oriented in different directions: developing new methods, reducing the cost of new or existing methods, or applying the existing methods efficiently, while keeping calculations accurate enough to grasp the decisive phenomena in a studied system. During the work underlying this thesis, I did not deal with the "paper-and-pen" development of new methods – instead, I was an "advanced user" and programmer of already existing ones, at points implementing them in new and more flexible code architectures and dealing with unavoidable numerical issues. This thesis summarizes these implementations and the applied studies of the two molecular systems which we investigated.

In Chapter 4, I describe our study of isotope effects in cyclohexane adsorbed at rhodium (111) surface. Isotope substitution is often used in experimental studies to clarify mechanisms of reactions, and activation of C–H bonds on metal surfaces is one of the important topics in chemical research, since it may be exploited in numerous applications from petrochemistry to reversible hydrogen storage [78, 79, 80]. Yoshinobu, Koitaya and others revealed changes in the electronic structure of C_6H_{12}–Rh(111) interface upon deuteration [8], which point toward anharmonic behavior of the C–H...Rh and needed to be explained theoretically.

In Chapter 5, I discuss our study of water splitting on a palladium (111) surface subjected to an electric field in order to mimic an electrochemical setup. Interaction of water and its decay products H and OH with metals is of crucial importance in a number of processes such as water splitting, oxidation of hydrogen in fuel cells, corrosion processes, etc. In many such cases, the surface is subject to a potential bias, being it an electrolytic electrode or cathodic protection against corrosion. The *ab initio* simulation of systems subject to potential biases is challenging. We show a study of the first basic step: the splitting of one hydrogen from a water molecule. In particular, we study how the reaction paths are modified by the presence of an electric field and how that changes zero-point energy contributions to the reaction barrier.

Chapter 2

Electronic structure theory

2.1 Electronic-nuclear Hamiltonian

The cornerstone of theoretical molecular and modern solid state physics is atomistic simulation. In order to shed light on microscopic processes, one needs to describe the motion of atomic nuclei and the interactions between them. If we neglect relativistic effects, the full interaction in a system of M nuclei and N electrons is described by the following Hamiltonian

$$\begin{aligned}\hat{\mathcal{H}} = &- \frac{\hbar^2}{2M_I}\sum_{I}^{M}\nabla_I^2 - \frac{\hbar^2}{2m_e}\sum_{i}^{N}\nabla_i^2 + \frac{e^2}{2}\sum_{I\neq J}\frac{Z_I Z_J}{|\boldsymbol{R_I}-\boldsymbol{R_J}|} \\ &+ \frac{e^2}{2}\sum_{i\neq j}\frac{1}{|\boldsymbol{r_i}-\boldsymbol{r_j}|} - e^2\sum_{i,I}\frac{Z_I}{|\boldsymbol{r_i}-\boldsymbol{R_I}|},\end{aligned} \tag{2.1}$$

where $\boldsymbol{R_I}, \boldsymbol{r_i}$ are the Cartesian coordinates of nuclei and electrons, respectively. Z_I, M_I and m_e are nuclear charges, masses and the mass of an electron.

A state of a quantum system is described by a wave function Ψ. Dynamics of such a system follows the Schrödinger equation

$$i\hbar\frac{d}{dt}|\Psi(t)\rangle = \hat{\mathcal{H}}|\Psi(t)\rangle. \tag{2.2}$$

In case we are interested in the stationary properties of a system, it boils down to the time-independent Schrödinger equation

$$\hat{\mathcal{H}}|\Psi_k\rangle = E_k|\Psi_k\rangle, \tag{2.3}$$

which is an eigenproblem with $\{E_k\}$ being the eigenvalues of the Hamiltonian, representing the energies of the corresponding stationary states $|\Psi_k\rangle$.

The Schrödinger equation, although very general, suffers from two problems. The first one is that it doesn't have a general analytical solution for a multidimensional electrostatic potential. The second problem is known as the "curse of dimensionality": if we try to solve the Schrödinger equation numerically, we have to represent it on a grid, the size of which increases exponentially with the number of degrees of freedom, which is $(3M + 3N)$ or $(3M + 4N)$ if we consider electronic spin. For a simplest H_2 molecule without spin and with just 10 grid points along each direction the total size of the grid becomes 10^9 points, and for O_2 molecule it reaches 10^{51} points. Therefore, practical approaches to solving them rely on a number of approximations.

2.2 Born-Oppenheimer approximation

Practical simulation of an atomistic system faces a controversy: on the one hand, in many cases, we are interested in processes occurring on the "nuclear" time scale, i.e. picoseconds and longer. On the other hand, electrons are much lighter than nuclei, and an accurate description of their dynamics requires simulation on a scale of *attoseconds*. This makes the treatment of a fully coupled system prohibitively expensive. The commonly used way to circumvent this problem is to sacrifice the exact coupling between electrons and nuclei and treat their dynamics separately. The fact that electrons move much faster than nuclei makes it reasonable to assume that electrons adapt rapidly to the changes caused by the slow motion of nuclei. Electrons thus always remain in their ground state, which changes as nuclei move. This model was proposed by M. Born and R. Oppenheimer in 1927 and is often referred to as the Born-Oppenheimer (BO) or the adiabatic approximation [81, 82]. The electronic Hamiltonian is

$$\hat{\mathcal{H}}_{\text{el}} = \hat{T}_{\text{el}} + \hat{V}_{\text{el}-\text{el}} + \hat{V}_{\text{el}-\text{nucl}} \tag{2.4}$$

with $\hat{T}_{\text{el}}$ being the electronic kinetic energy operator, $\hat{V}_{\text{el}-\text{el}}$ – the Coulomb interaction between electrons, and $\hat{V}_{\text{el}-\text{nucl}}$ – the Coulomb interaction between electrons and nuclei. We can formally write down the solution of the Schrödinger equation 2.3 for the

electronic Hamiltonian taking $\boldsymbol{R} = \{\boldsymbol{R_1}, ..., \boldsymbol{R_M}\}$ as a parameter:

$$\hat{\mathcal{H}}_{\text{el}}|\psi_k(\boldsymbol{R}, \boldsymbol{r})\rangle = E_k^{\text{el}}(\boldsymbol{R})|\psi_k(\boldsymbol{R}, \boldsymbol{r})\rangle, \tag{2.5}$$

For any $\boldsymbol{R}$, the eigenfunctions $\{|\psi_k\rangle\}$ form a complete basis in $\boldsymbol{r}$ subspace, therefore we can express the solutions of the full eq. 2.3 as a parametric expansion

$$|\Psi_i\rangle = \sum_k C_k^i(\boldsymbol{R})|\psi_k(\boldsymbol{R}, \boldsymbol{r})\rangle \tag{2.6}$$

If we substitute it into eq. 2.3 and multiply both sides by $\langle\psi_j|$, the equation becomes

$$\begin{aligned}&\left(\hat{T}_{\text{nucl}} + \hat{V}_{\text{nucl}-\text{nucl}} + E_j^{\text{el}}(\boldsymbol{R})\right) C_j^i(\boldsymbol{R}) \\ &\quad - \sum_I^M \sum_k \frac{\hbar^2}{2M_I} \left[\int d\boldsymbol{r} C_k^i \psi_j^* \nabla_{\boldsymbol{R}}^2 \psi_k + 2\int d\boldsymbol{r} \psi_j^* \nabla_{\boldsymbol{R}} \psi_k \nabla_{\boldsymbol{R}} C_k^i(\boldsymbol{R})\right] = E_i C_j^i(\boldsymbol{R}).\end{aligned} \tag{2.7}$$

The terms in square braces are responsible for electron-nuclear coupling, and the BO approximation takes them as zero, meaning that variations of the nuclear coordinates do not act on the electronic states. One can see that without those terms the full Schrödinger equation boils down to the equation for nuclei with a Hamiltonian $\hat{\mathcal{H}}_j^{\text{nucl}} = \hat{T}_{\text{nucl}} + \hat{V}_{\text{nucl}-\text{nucl}} + E_j^{\text{el}}(\boldsymbol{R})$, i.e. nuclei are moving on the j-th *potential energy surface* created by the j-th electronic state (plus nuclear Coulomb repulsion).

Once electronic and nuclear degrees of freedom are separated, one can choose different strategies to treat them. For many applications, it is enough to consider nuclei as classical particles – e.g. for heavy nuclei, or include their quantum behavior only up to a certain limit. We will discuss nuclear quantum effects in section 3.1.

The electronic subsystem can be treated on different levels of approximation. One remarkable approximation which I use throughout this work is density-functional theory (DFT), which will be described in the section 2.3.

2.3 The Hohenberg-Kohn theorem and Kohn-Sham equations

A breakthrough in attempts to escape the curse of dimensionality in electronic subsystem was achieved by P. Hohenberg, W. Kohn and L. Sham in 1960-s [83, 84]. First,

Hohenberg and Kohn proved that the ground state of an ensemble of electrons in a given external potential can be described by a *unique* electron density $\rho(\mathbf{r})$ [83]. The energy then becomes a functional of the density with the minimum at the ground-state density, and this functional is claimed to be universal for any external potential. This is a huge step forward from a $3N$-dimensional problem to a 3-dimensional one. However, finding the exact form of this functional appeared to be a very nontrivial problem, which has not been solved in almost 60 years separating us from the paper of Hohenberg and Kohn. I should mention that the density depends on a spin variable also, and it would be correct to write $\rho(\boldsymbol{r}, \sigma)$, but I omit spin to keep the derivation simple. Including spin does not change the essence of the derivation of the Kohn-Sham theory, except for the fact that the exchange energy depends on the spin state of the system.

In order to ease this task, it makes sense to deconstruct this potential into pieces. First, one can separate the two terms that are straightforward to calculate for a given density:

$$E[\rho] = \int v_{\text{ext}}(\boldsymbol{r})\rho(\boldsymbol{r})d\boldsymbol{r} + \frac{1}{2}\int\int \frac{\rho(\boldsymbol{r})\rho(\boldsymbol{r'})}{|\boldsymbol{r}-\boldsymbol{r'}|}d\boldsymbol{r}d\boldsymbol{r'} + T[\rho] + E_{\text{xc}}[\rho], \tag{2.8}$$

where the first term comes from the external potential v_{ext} coming from interaction with nuclei and an external electric field, the second one gives the classical Coulomb repulsion between electrons, and the rest two are the kinetic energy of electrons $T[\rho]$ and so-called exchange-correlation energy $E_{\text{xc}}[\rho]$, responsible for everything that is not covered by the other terms. I will discuss E_{xc} later. While the first two terms are self-explanatory, the kinetic energy of an electron density of correlated electrons is unknown. In order to overcome this, Kohn and Sham proposed to consider a fictitious system of N non-interacting electrons which would have the same electron density $\rho(\boldsymbol{r})$ [84]. The density of these so-called Kohn-Sham orbitals is

$$\rho(\boldsymbol{r}) = \sum_{i}^{N} \phi_i^*(\boldsymbol{r})\phi_i(\boldsymbol{r}). \tag{2.9}$$

Since the electrons in this fictitious system do not interact, its ground state is a Slater determinant constructed from the single-particle wavefunctions ϕ_i. Then, the kinetic energy is simply given by

$$T = \sum_{i}^{N} \langle\phi_i| -\frac{1}{2}\nabla^2|\phi_i\rangle \tag{2.10}$$

We now can rewrite equation 2.8 in terms of Kohn-Sham orbitals ϕ_i:

$$E[\rho] = \sum_i^N \langle\phi_i| -\frac{1}{2}\nabla^2 + v_{\text{ext}}(\boldsymbol{r})|\phi_i\rangle + \sum_{i,j}\langle\phi_i,\phi_j|\frac{1}{|\boldsymbol{r_i}-\boldsymbol{r_j}|}|\phi_i\phi_j\rangle + E_{\text{xc}}[\rho]. \tag{2.11}$$

Now, we can find a set of wavefunctions $\{\phi\}$ satisfying several conditions: they should be orthonormalized and $E[\rho(\{\phi\})]$ must be minimal across all possible sets $\{\phi\}$, which can be expressed in a form of a variational condition

$$\int \delta\rho(\boldsymbol{r})d\boldsymbol{r}\left\{\frac{\delta T[\rho]}{\delta\rho} + v_{\text{H}} + v_{\text{ext}} + v_{\text{xc}}\right\} = 0, \tag{2.12}$$

where v_{H} is a so-called Hartree potential

$$v_{\text{H}} = \int d\boldsymbol{r'}\frac{\rho(\boldsymbol{r'})}{|\boldsymbol{r}-\boldsymbol{r'}|}, \tag{2.13}$$

and v_{xc} is an exchange-correlation potential

$$v_{\text{xc}} = \frac{\delta E_{\text{xc}}[\rho]}{\delta\rho(\boldsymbol{r})}. \tag{2.14}$$

The orthonormality constraint and eq. 2.12 lead to a Schrödinger-like eigenvalue problem

$$\left[\hat{T} + v_{\text{H}} + v_{\text{ext}} + v_{\text{xc}}\right]\phi_i = \epsilon_i\phi_i. \tag{2.15}$$

The solutions are obtained simply by diagonalizing the Hamiltonian matrix representing the brackets in equation 2.15. I will refer this matrix as h_{ij}^{KS}. After the eigenfunctions and eigenvalues are obtained, these single-particle states are populated with electrons in ascending energy order up to a total number of electrons N. After that, the density is built according to eq. 2.9 and the energy functional can be constructed again. Since the Hamiltonian depends on the total electron density non-trivially, there is no guarantee that the resulting electron density induces the same energy functional that was used to obtain that density. Therefore this procedure should be iterated under the constraint that N is kept fixed [1], until the density becomes self-consistent. Now, the only missing piece of this puzzle is the exchange-correlation potential, which I discuss right below.

[1] Although this constraint follows from eq. 2.9, it may be lifted and replaced by a constraint on a chemical potential in order to model an open system such as an electrode connected to a battery [4].

2.4 Exchange-correlation functionals

Since the exact form of the exchange-correlation potential is not known so far, one needs some approximation in order to do practical calculations. The main approximation that is done in most cases is the locality of the potential: instead of being the potential of the whole density $v_{\mathrm{xc}}[\rho](\boldsymbol{r})$, it is chosen to be a function of a density at single point only $v_{\mathrm{xc}}[\rho(\boldsymbol{r})]$, or at a point and its near surrounding $v_{\mathrm{xc}}[\rho(\boldsymbol{r}+d\boldsymbol{r})]$. The first case is known in the community as the local density approximation (LDA), and the latter one as the generalized gradient approximation (GGA). The local density approximation (LDA) model utilizes the exchange energy $E_{\mathrm{X}}^{\mathrm{LDA}}$ and correlation energy $E_{\mathrm{C}}^{\mathrm{LDA}}$ of homogeneous electron gas (HEG), of which the first one is known analytically and the latter one was fitted from quantum Monte-Carlo simulations [85].

$$E_{\mathrm{XC}}^{\mathrm{LDA}}[\rho] = -\frac{3}{4}\left(\frac{3}{\pi}\right)^{1/3}\int \rho(\boldsymbol{r})^{4/3}d\boldsymbol{r} + E_{\mathrm{C}}^{\mathrm{LDA}}. \tag{2.16}$$

The model that I used the most throughout my electronic structure calculations is the generalized gradient approximation (GGA) Perdew–Burke-Ernzerhof model, widely known as PBE [86]. For the following discussion, the inclusion of spin is necessary. The Perdew–Burke-Ernzerhof (PBE) functional is constructed as an expansion on top of the XC of HEG. The correlation part is then

$$E_{\mathrm{C}}^{\mathrm{GGA}}[\rho_\uparrow,\rho_\downarrow] = \int d\boldsymbol{r}\rho[\epsilon_{\mathrm{C}}^{\mathrm{unif}}(r_s,\zeta) + H(r_s,\zeta,t)], \tag{2.17}$$

where $\zeta = (\rho_\uparrow - \rho_\downarrow)/\rho$ is the relative spin polarization, and $t \propto |\nabla\rho|/\rho$ is a dimensionless density gradient defined in a particular way [86], and r_s is the local Seitz radius which characterizes the distance between electrons in the HEG having the density ρ^{HEG}, which in a 3-dimensional case read as

$$\frac{4}{3}\pi r_s^3\rho^{\mathrm{HEG}} = 1 \quad\Leftrightarrow\quad r_s = \sqrt[3]{\frac{3}{4\pi\rho^{\mathrm{HEG}}}}. \tag{2.18}$$

Without going into all the details, the main physical requirements to satisfy are the second-order proportionality to the density gradient in the limit of a small gradient

$$H \xrightarrow{t\to 0} O(t^2), \tag{2.19}$$

and vanishing of the correlations in the limit of very fast varying density

$$H \xrightarrow{t\to\infty} -\epsilon_{\mathrm{C}}^{\mathrm{unif}}. \tag{2.20}$$

There is a third requirement that the correlation energy remains the same under the simultaneous scaling of a space and a density $\boldsymbol{r} \to \lambda \boldsymbol{r}$, $\rho(\boldsymbol{r}) \to \lambda^3 \rho(\lambda \boldsymbol{r})$. For the details, I address a reader to the original papers [86, 87].

The exchange contribution has to satisfy the same scaling relation, and another one for spin scaling:

$$E_{\mathrm{X}}[\rho_\uparrow, \rho_\downarrow] = \left(E_{\mathrm{X}}[2\rho_\uparrow] + E_{\mathrm{X}}[2\rho_\downarrow]\right)/2. \tag{2.21}$$

In simple words, I see the underlying idea of the PBE functional as keeping all the properties of the well-established XC energy of LDA, and, at the same time, ensuring that the term H, which comes from the density gradient, restores scaling relations where is it known that the LDA model fails to satisfy them. Interestingly, these fully *ab initio* conditions are enough to have a robust model which covers a vast variety of atomistic systems. However, there are still significant weaknesses of the PBE functional. The main two are its poor behavior on strongly correlated systems and the self-interaction error (SIE). Self-interaction is a general problem of the DFT approach: in the real world, an electron does not have Coulomb interaction with itself, only with other particles. But in the density representation, we do not have the resolution for single electrons anymore and therefore cannot distinguish between an electron's "own" density and the surrounding one. A textbook example of complete failure of PBE is the dissociation of symmetric ions, e.g. H_2^+ into H and H^+ [88]. Although there is progress in understanding the nature of SIE [89], it seems that there is no simple way to apply a correction to the PBE functional, and the methods that correct SIE are more computationally expensive than PBE, because typically they include a fraction of exact exchange. Some of them are discussed in [90, 91, 31]. Despite these problems, PBE has shown many times its fair accuracy for energetics and structure properties of small molecules[92, 93] and solids [94, 95]. Particularly for water, which is of interest for Chapter 5, a review [96] shows that PBE performs "not great, not terribly" compared to other models: it overamplifies hydrogen bonding and therefore predicts overstructured liquid water, but predicts energies not much worse than hybrid PBE0 model and many others. Another built-in weakness of any (semi-)local functional, is its inability to capture long-range correlations. These terms are typically added as corrections on top of GGA functionals, I discuss them in the following section.

2.5 Van der Waals interactions

Most of the existing XC functionals, including PBE, are local and therefore miss any long-range interactions beyond electrostatic ones. A very important class of non-local correlations are so-called dispersive interactions, which connect local perturbations of the electronic density with their distant counterparts. Even though the ground-state electron density is static in absence of time-dependent external forces, the electrons which constitute that density are not static – in contrast, they are in constant movement and create instantaneous dipoles which interact with each other. The long-range attractive interactions between molecules were first proposed empirically by J. D. van der Waals to improve the description of gases beyond the ideal gas model, and to explain the condensation phenomenon [97]. By the beginning of the 1930s, it was clear to the community that the attraction must be caused by the dynamical polarization of molecules due to the fast movement of electrons [98]. J. Lennard-Jones considered a harmonic oscillator model and showed that the interaction energy of two distant harmonic oscillators has $1/R^6$ dependence – the same as in his famous potential [99]. The theoretical description of such interactions for realistic molecular systems was proposed by F. London in 1936 [63]. London derived the expression for the interaction of two molecules, each of them being represented by a set of periodically oscillating dipoles. One can interpret these dipoles as possible excited states available for an electron if there is an external perturbation. London shows the connection of these oscillating dipoles to molecular polarizability in general frequency dependent form $\alpha(\omega)$, and, as a particular case, static polarizability $\alpha(0)$[2]:

$$\alpha(\omega) = \frac{2}{3} \sum_l \frac{\mu_l^2 \nu_l}{\nu_l^2 - \omega^2}, \tag{2.22}$$

$$\alpha_k^0 \equiv \alpha_k(0) = \frac{2}{3} \frac{\mu_k^2}{\nu_k}, \tag{2.23}$$

where μ_l, ν_l are the dipole moment and the frequency of the l-th oscillating dipole of the molecule, and μ_k, ν_k denote a single oscillator with the maximal contribution, which dominates over the contributions of the rest. The energy of interaction between

[2]Compared to the original paper of London, I use atomic units, therefore there is no h here.

two molecules characterized by their dominant states ρ and k is then

$$E_{\rho k} = \frac{3}{2R^6} \cdot \alpha_k^0 \alpha_\rho^0 \frac{\nu_k \nu_\rho}{\nu_k + \nu_\rho}, \tag{2.24}$$

where R is the distance between the molecules. Interestingly, London shows on the experimental data, that ν_k for real atoms corresponds to the ionization energy, not to the $0 \rightarrow 1$ transition. I find this fact counterintuitive.

Later, H. B. G. Casimir and D. Polder (1948) considered dispersive interactions using the formalism of quantum electrodynamics, in which the interaction is mediated by the fluctuating electromagnetic field [100]. For the interaction of two atoms or molecules, they arrived at the expression for the R^{-6} coefficient C_{6AB}, the so-called Casimir-Polder integral:

$$C_{6AB} = \frac{3}{\pi} \int_0^\infty d\omega \, \alpha_A(i\omega) \alpha_B(i\omega). \tag{2.25}$$

We note that α is now a function of imaginary frequency $i\omega$. This is due to the fact that $\int_0^\infty \alpha(i\omega) d\omega = \int_0^\infty \mathrm{Im}[\alpha(\omega)] d\omega$. A rigorous explanation of the underlying math is quite bulky, an interested reader may find it in § 123 of Vol. 5 of Landau-Lifshitz [101]. Casimir and Polder showed also, that at very long distances, longer than the wavelengths associated with excitations of atoms, the retardation of the field leads to dipole oscillations of the atoms being out of phase, which leads to R^{-7} dependence instead of R^{-6}. For the interaction between a perfectly conducting surface and an atom they obtained

$$E_{\mathrm{surf-atom}}^{\mathrm{vdW}} = -\frac{1}{16R^3} \sum_n \left(|\mu_{n^x}^x|^2 + |\mu_{n^y}^y|^2 + 2|\mu_{n^z}^z|^2 \right), \tag{2.26}$$

where $\mu_{n^i}^i$ are the dipole components associated with the n^i-th excited state, $i = x, y, z$.

E. M. Lifshitz (1956) derived the dispersion interaction of two arbitrary solid surfaces based on their dielectric functions $\epsilon(\omega)$ solely, restoring both Casimir's result for ideally conducting surfaces and London's result for atoms as a low-density limit $\epsilon \rightarrow 1$ [102]. The results of Lifshitz were further used by E. Zaremba and W. Kohn to describe surface-molecule interaction [103]. Zaremba and Kohn were interested in interactions that are short-range $Z << \lambda_\nu$ (but still long enough to have no overlap of electron densities), meaning that the definition of the exact position of the surface plane Z_0 (see fig. 2.1) becomes important, and also considered real crystalline surfaces,

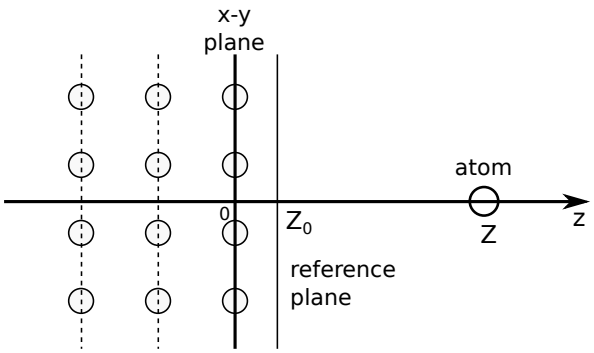

Figure 2.1: Schematic representation of atom-surface system discussed in sec. 2.5. Z_0 corresponds to the Lifshitz-Zaremba-Kohn reference plane position.

which means that the definition of a "surface plane" becomes vague. They managed to express the leading term in the van der Waals energy and the reference plane position as functions of imaginary-frequency-dependent polarizability $\alpha_{\mathrm{mol}}(i\omega)$ of a molecule, the dielectric function $\epsilon_{\mathrm{surf}}(i\omega)$ of a surface, and an additional property $\bar{z}(i\omega)$, which is, simply speaking, the weighted average z-coordinate showing at which z the density response to an external field of the frequency $i\omega$ is the most pronounced:

$$E^{\mathrm{vdW}}_{\mathrm{surf-mol}} = -C_3 \left(Z - Z_0\right)^{-3} + O\left(\left(Z - Z_0\right)^{-5}\right), \tag{2.27}$$

$$C_3 = \frac{1}{4\pi} \int_0^\infty d(\omega) \alpha_{\mathrm{mol}}(i\omega) \left(\frac{\epsilon_{\mathrm{surf}}(i\omega) - 1}{\epsilon_{\mathrm{surf}}(i\omega) + 1} \right), \tag{2.28}$$

$$Z_0 = \frac{\int_0^\infty d(\omega) \alpha_{\mathrm{mol}}(i\omega) \bar{z}(i\omega) \left(\frac{\epsilon_{\mathrm{surf}}(i\omega) - 1}{\epsilon_{\mathrm{surf}}(i\omega) + 1} \right)}{\int_0^\infty d(\omega) \alpha_{\mathrm{mol}}(i\omega) \left(\frac{\epsilon_{\mathrm{surf}}(i\omega) - 1}{\epsilon_{\mathrm{surf}}(i\omega) + 1} \right)} \tag{2.29}$$

In a more general form, the expression 2.27 for $E^{\mathrm{vdW}}_{\mathrm{surf-mol}}$ would also have a 4th order term, but Z_0 has a special property that if one measures the distance from Z_0, the 4th order term vanishes. These parameters are relatively easy to calculate, which paves the way to the practical use of this formalism, which I describe in the next section.

2.5.1 Tkatchenko-Scheffler van der Waals model for molecules

The theory described above gives van der Waals energy which a) is pairwise if we consider a surface as a single entity, and b) has simple power dependence on distance: either C_6/R^6 for molecules or C_3/Z^3 for surface-molecule interaction. These facts tempted

researchers to fit C_6 and C_3 parameters empirically and to perform practical calculations. Here I discuss the model that I was using throughout most of my simulations – the Tkatchenko-Scheffler (TS) model [64] and its adaptation for molecule-surface interaction [10].

Tkatchenko and Scheffler proposed a mixing scheme how to obtain C_6 coefficients for heteronuclear interactions given that the homonuclear ones are known

$$C_{6AB} = \frac{2C_{6AA}C_{6BB}}{\left[\frac{\alpha_B^0}{\alpha_A^0}C_{6AA} + \frac{\alpha_A^0}{\alpha_B^0}C_{6BB}\right]}. \tag{2.30}$$

A good estimate for $\alpha(i\omega)$ can be obtained from the London's expressions 2.22, 2.23 by keeping only the most important frequency ν in the summation in 2.22 (so-called Unsöld approximation [104]). We then get

$$\alpha(\omega) = \frac{\alpha^0}{1 - \omega^2/\nu^2} \tag{2.31}$$

and, correspondingly,

$$\alpha(i\omega) = \frac{\alpha^0}{1 + \omega^2/\nu^2} \tag{2.32}$$

One can show that the same expression remains valid beyond the Unsöld approximation [105].

Since the interaction is pairwise, the van der Waals energy is simply divided equally between two considered atoms. In the case of molecules, the electron density is a collective entity and is not attributed unambiguously to particular atoms. However, in practical calculations within the Born-Oppenheimer approximation, we are interested to know not only the energy of an interaction, but also *atomic forces*, just as in the atomic case in the theoretical works above. One could, of course, take the derivative of the energy numerically given that molecular vdW energy can be calculated for any geometry, but that would require the calculation of electron density $3N_{at}$ times. Instead, Tkatchenko and Scheffler distribute the total electron density of a system between its atoms using the Hirshfeld partitioning [106]. This partitioning is then used to define an atomic volume, which is proportional to atomic polarizability [107].

$$\alpha^{\text{eff}} \approx \frac{V^{\text{eff}}}{V^{\text{free}}}\alpha^{\text{free}}, \tag{2.33}$$

One can expect this approximation to fail in highly polarizable molecules, where the electron density is significantly delocalized, e.g. in large π-conjugated systems. For

example, one can look at the polarizability of anthracene: it is highly anisotropic and cannot be described by the sum of atomic polarizabilities [108].

Finally, a practical implementation of such a van der Waals correction should remain within its limit of applicability, i.e. in the range of distances where the overlap of electronic densities is negligibly small. For that purpose, one can introduce a damping function into the expression:

$$E_{\mathrm{vdW}} = -\frac{1}{2} f_{\mathrm{damp}}\left(R_{AB}, R_A^0, R_B^0\right) \frac{C_{6AB}}{R_{AB}^6}, \tag{2.34}$$

where R_A^0, R_B^0 are the vdW radii of the corresponding atoms. The proposed model of damping is empirical and based on the van der Waals radii, which are taken equal for the elements of the same row in the periodic table. The damping function in this method is Fermi-like:

$$f_{\mathrm{damp}}\left(R_{AB}, R_{AB}^0\right) = \frac{1}{1 + \exp\left[-d\left(\frac{R_{AB}}{sR_{AB}^0} - 1\right)\right]}, \tag{2.35}$$

with $R_{AB}^0 = R_A^0 + R_B^0$ and d, s fitted to existing highly accurate quantum-chemical calculations. The Tkatchenko-Scheffler model has the advantage that it is very cheap: the bottleneck is the cost of the Hirshfeld partitioning, which is very small compared to the cost of underlying Kohn-Sham density-functional theory (KS-DFT) calculation. There are two ways of applying the van der Waals (vdW) correction in FHI-aims code: one can calculate the electron density with a local/semilocal XC functional and calculate the vdW correction only once after SCF has converged, or one can explicitly make vdW a part of the energy functional which enters in each SCF iteration. For the systems discussed in this thesis, these two algorithms yield very close results. We use the first scheme because the calculation of forces is not implemented for the latter one. However, we note that the difference between these methods should be assessed for a particular system because it's not necessarily negligible.

2.5.2 Tkatchenko-Scheffler model for a surface-molecule interaction

The next challenge is to include collective effects present in a surface, such as screening, into the pairwise vdW interaction described above. The physical nature of the effect

is that the presence of other atoms around effectively creates a dielectric environment, which weakens the interaction of an atom with external perturbations. It was shown that if one applies the TS-vdW correction to a molecule adsorbed on a metallic surface, the lack of description of the collective nature of the surface will lead to an overestimation of the adsorption energy [109]. In the works [102, 103] it was noted that one can construct the R^{-3} response of a surface by integrating over the semi-infinite space filled with atoms, each of them interacting as R^{-6}:

$$E_{\mathrm{vdW}} \approx -\int dV n_s \frac{C_6^{As}}{R^6}, \tag{2.36}$$

where index A denotes a distant molecule, s now denotes an individual atom of the surface, and n_s is the number of atoms per unit volume of the surface. Comparing it with the expression 2.27, we can conclude that

$$C_3 = \frac{\pi}{6} n_s C_6^{As}. \tag{2.37}$$

Thus, if we calculated C_3 from the properties of the surface according to the equation 2.28 which has collective effects included, we can assign effective C_6^{As} coefficients to the surface atoms and use it in the simulations [10]. Such an approach is referred to in the literature as Lifshitz-Zaremba-Kohn model (LZK). The same mixing rule 2.30 for heteronuclear interactions is applicable. V. Ruiz, A. Tkatchenko and others calculated and published effective C_6^{LZK}, α_0 and R_0 properties for many metallic surfaces [110]. Throughout this thesis, I will refer to the LZK model with the parameters from Ruiz *et al.* as $\mathrm{vdW}^{\mathrm{surf}}$.

2.5.3 Many-body dispersion

The pairwise model for dispersion interactions has the obvious disadvantage that it misses collective effects. As we already saw in the case of surface, the pairwise model itself cannot describe interaction correctly and should include an additional physical insight from the electrodynamics of continuous media. This is true not only for surfaces – in fact, any system will show more and more collective interactions with increase of its density. Therefore, another approach is desired, which would be able to capture such effects. The many-body dispersion (MBD) [111] model considers a system of harmonic

oscillators having charges q_i, masses m_i, frequencies ν_i and centers $\boldsymbol{R_i}$. The opposite charges are located at $\boldsymbol{R_i}$ positions. The interaction is truncated at the dipole terms, resulting in a Hamiltonian

$$\hat{H}_{\mathrm{dipHO}} = \sum_i \frac{\hat{\boldsymbol{p}}_i^2}{2} + \sum_i \frac{1}{2} m_i \nu_i^2 |\hat{\boldsymbol{r}}_i - \boldsymbol{R}_i|^2 + \sum_{i<j} q_i q_j (\hat{\boldsymbol{r}}_i - \boldsymbol{R}_i) \cdot \hat{\boldsymbol{T}}(\boldsymbol{R}_j - \boldsymbol{R}_i) \cdot (\hat{\boldsymbol{r}}_j - \boldsymbol{R}_j), \quad (2.38)$$

where $\hat{\boldsymbol{r}}$, $\hat{\boldsymbol{p}}$ are positions and momenta of the oscillators, and $\hat{\boldsymbol{T}}(\boldsymbol{R}_j - \boldsymbol{R}_i)$ is a dipole-dipole interaction tensor. This Hamiltonian can be diagonalized and its eigenvalues and eigenvectors $\tilde{\nu}_i$, $\boldsymbol{\xi_i}$ can be obtained analytically.

$$\hat{H}_{\mathrm{dipHO}} = \sum_{i=1}^{3N} \left(\frac{\hat{p}_i^{\,2}}{2} + \frac{\tilde{\nu}_i \hat{\boldsymbol{\xi}}_{\boldsymbol{i}}^{\,2}}{2} \right) \quad (2.39)$$

In order to use this model, $\hat{\boldsymbol{T}}$ has to be defined. To include screening effects in the polarizability, it is first converted from atomic property to a continuous function $\alpha(\boldsymbol{r}, i\omega)$ via approximating atoms by Gaussian densities (because the ground-state wavefunction of a harmonic oscillator is indeed a Gaussian) [112]. Then, the self-consistently screened polarizability α^{SCS} is calculated as

$$\alpha^{\mathrm{SCS}}(\boldsymbol{r}, i\omega) = \alpha^{\mathrm{TS}}(\boldsymbol{r}, i\omega) \left(1 - \int d\boldsymbol{r'} \boldsymbol{T}(\boldsymbol{r} - \boldsymbol{r'}) \alpha^{\mathrm{SCS}}(\boldsymbol{r'}, i\omega) \right), \quad (2.40)$$

where α^{TS} is calculated by the formula 2.33. Gaussian electron density allows to take the integral in 2.40 analytically, which gives polarizability in a discrete form again:

$$\alpha_p^{\mathrm{SCS}}(i\omega) = \alpha_p^{\mathrm{TS}}(i\omega) \left(1 + \sum_{q \neq p}^{N} \boldsymbol{T_{pq}} \alpha_q^{\mathrm{SCS}}(i\omega) \right), \quad (2.41)$$

$$\boldsymbol{T_{pq}} = \frac{\partial}{\partial \boldsymbol{r}_p} \frac{\partial}{\partial \boldsymbol{r}_q} w^{\mathrm{GG}}(r_{pq}), \quad (2.42)$$

where $w^{\mathrm{GG}}(r_{pq})$ is the energy of Coulomb interaction of two Gaussians with the widths σ, σ', if one of them is centered at 0 and another at $\boldsymbol{r}_{pq}$

$$w^{\mathrm{GG}}(r_{pq}) = \frac{1}{(\pi\sigma\sigma')^3} \int\int d\boldsymbol{r} d\boldsymbol{r'} \frac{1}{|\boldsymbol{r} - \boldsymbol{r'}|} \exp\left(\frac{-|\boldsymbol{r}|^2}{\sigma^2} \right) \exp\left(\frac{-|\boldsymbol{r'} - \boldsymbol{r_{pq}}|^2}{\sigma'^2} \right)$$
$$= \frac{1}{r_{pq}} \mathrm{erf}\left(\frac{\mathrm{r_{pq}}}{\sqrt{\sigma^2 + \sigma'^2}} \right) \quad (2.43)$$

The widths of the Gaussians can be expressed via $\alpha(i\omega)$ [112, 113]:

$$\sigma(u) = \left(\frac{1}{3} \sqrt{\frac{2}{\pi}} \alpha(i\omega) \right)^{1/3}, \quad (2.44)$$

To summarize, the sequence of operations of the MBD method is the following:

1. Calculate α_i^{TS} for atoms according to 2.33;

2. Calculate widths of the Gaussians $\sigma_i(\alpha_i)$ by 2.44;

3. Calculate w_{ij}^{GG}, T_{ij} for each pair of atoms (2.43 and 2.42, respectively);

4. Estimate α_i^{SCS} using α^{TS}, $\boldsymbol{T}$ in the eq. 2.41;

5. Repeat 2-4 until self-consistency for α_i^{SCS} is reached;

6. Use the final $\boldsymbol{T}$ and diagonalize the Hamiltonian 2.38 and calculate the energy.

Similarly to the Tkatchenko-Sheffler method, range separation can be applied to $\boldsymbol{T}$ in order to switch it off smoothly at short distances, where the DFT XC functional is expected to capture local correlations well. Then, only the short-range interaction is used to calculate screened polarizability, while the long-range part is responsible for the calculation of the MBD energy, and the method is then called MBD@rsSCS [114].

Reciprocal-space formulation of MBD

In the case of a solid, real-space formulation becomes inconvenient, because one would need to account for formally infinite, and in practice for a large number of interactions to get the screening converged. A cutoff radius up to 120 Å may be needed to converge the self-consistent screening [115], which makes these calculations quite heavy. The corresponding $\boldsymbol{T}$ and $\boldsymbol{\alpha}$ have a dimensionality of $(3N_{\mathrm{at}}N_{\mathrm{cells}}) \times (3N_{\mathrm{at}}N_{\mathrm{cells}})$, where N_{at} is the number of atoms in a unit cell, and N_{cells} is the number of unit cells within the cutoff radius.

T. Bučko *et al.* (2016) proposed a reciprocal-space formulation [115]. Infinite summation over Gaussians in real space is replaced by summation within a single unit cell and integration over the first Brillouin zone (FBZ):

$$E_{\mathrm{vdW}} = \int_{\mathrm{FBZ}} \frac{d\boldsymbol{k}}{(2\pi)^3 \Omega_{\mathrm{u.c.}}} \int_0^\infty \frac{d\omega}{2\pi} \mathrm{Tr}_{\mathrm{u.c.}} \left[\ln \left(1 - \boldsymbol{\alpha}(\boldsymbol{k}, i\omega) \boldsymbol{T}^{\mathbf{LR}}(\boldsymbol{k}) \right) \right], \tag{2.45}$$

where the trace denotes summation over all atoms in the unit cell, $\Omega_{\mathrm{u.c.}}$ is the volume of the unit cell, $\boldsymbol{\alpha}(\boldsymbol{k}, i\omega)$ is a Fourier-transformed diagonal matrix of atomic polarizabilities α_p:

$$\alpha_p(\boldsymbol{k}, i\omega) = \sum_{\boldsymbol{b}} \boldsymbol{\alpha}_{\boldsymbol{r_p}, \boldsymbol{r_p}+\boldsymbol{b}}(i\omega) \cdot \mathrm{e}^{i\boldsymbol{k}\boldsymbol{b}} \tag{2.46}$$

with $\boldsymbol{b}$ being all possible Bravais vectors, and $\boldsymbol{T}^{\mathbf{LR}}(\boldsymbol{k})$ is a Fourier-transformed long-range part of $\boldsymbol{T}$: $\boldsymbol{T}^{\mathbf{LR}} = \boldsymbol{T} * f^{\mathrm{damp}}$ from the eq. 2.35. The element responsible for the interaction between atoms p and p' from the unit cell is

$$\boldsymbol{T}^{\mathbf{LR}}_{pp'}(\boldsymbol{k}) = \sum_{\boldsymbol{b}} \boldsymbol{T}^{\mathbf{LR}}_{r_p, r_{p'}+b} \cdot \mathrm{e}^{-i\boldsymbol{k}(\boldsymbol{r_p}-\boldsymbol{b}-\boldsymbol{r_{p'}})}. \tag{2.47}$$

Therefore, the real-space problem 2.38 of dimension $(3N_{\mathrm{at}}N_{\mathrm{cells}}) \times (3N_{\mathrm{at}}N_{\mathrm{cells}})$ decomposes into N_q problems of size $(3N_{\mathrm{at}}) \times (3N_{\mathrm{at}})$ with N_q being the number of k-points to integrate eq. 2.45.

Extending MBD to ionic systems

The last (to date) step of the evolution of the MBD family is the extension to ionic systems, whose polarizability is poorly described by atomic polarizabilities used above. In order to capture that, a substantial generalization of polarizability was done: instead of atomic or rsSCS polarizability, a semi-local functional of Vydrov-Van Voorhis (VV) [116] was applied to calculate the polarizability of a *density* [67]:

$$\alpha^{\mathrm{VV}}[\rho](\boldsymbol{r}, i\omega) = \frac{\rho(\boldsymbol{r})}{\frac{4\pi}{3}\rho(\boldsymbol{r}) + C\left(\frac{\nabla\rho(\boldsymbol{r})}{\rho(\boldsymbol{r})}\right)^4 + \omega^2}, \tag{2.48}$$

where C is an empirical parameter. This density polarizability is then "collected" into atomic ones via Hirshfeld partitioning of the density and used to construct the coupled-quantum harmonic oscillator (QHO)s Hamiltonian 2.38. For the sake of compactness, I do not discuss another model that was proposed to achieve the same goal, although it deserves acknowledgment. A reader can find another version of MBD for ionic systems in the paper of T. Gould, T. Bučko and coauthors (2016) [117].

2.6 Potential bias in metallic surface simulations

Metals have a macroscopically large number of electrons in the conduction band, which form a free electron gas and can travel very long distances within metal bulk to compensate for external perturbations of an electric field. The electronic state of a microscopic part of a system is described by its chemical potential rather than the number of electrons. If a metallic system is subjected to a potential bias, e.g. if it is connected to

a battery, this "infinite supply" of electrons easily charges the surface up to a very significant charge. Therefore, the charge in a surface region of metal is not conserved. In contrast to the real world, if one applies KS-DFT simulations to such situations, one typically has a very small number of atoms, in the range from dozens to a few hundreds, and by the construction of the method, the number of electrons in the system is defined *a priori*. These two facts limit the ability to model a potential bias applied to a surface. In addition, most of the existing electronic-structure packages do not allow a user to set mixed boundary conditions – either all 3 dimensions have periodic boundaries, or they all have no boundary, mimicking a cluster isolated in a vacuum. Since a surface has to be periodic in its lateral dimensions to describe its phonon and electronic band structures, those packages require the direction orthogonal to the surface to have a periodic boundary also. Therefore, a model of a surface has, in fact, two surfaces on two sides of a slab of a few atomic layers of metal. Another problem that appears in periodic boundary conditions is a divergence of the Coulomb potential if a unit cell has a non-zero net charge. In periodic bulk systems, it is typically solved by neglecting the zeroth Fourier component in the Ewald summation, which describes the "baseline" of charge distribution. It is equivalent to introducing a compensating background charge to make the cell as a whole neutral. If one does the same for a slab model, homogeneous background interacts with the charge localized in the slab and produces a spurious dipole, which scales up with the size of the vacuum layer (see for example [118]). In the following sections, I will discuss the methods how to simulate potential bias under the above-mentioned technical restrictions.

2.6.1 A cluster model

The simplest possible approximation for the semi-infinite bulk is a cluster isolated in a vacuum. Such a model has a bad surface-volume ratio, which means that in order to avoid interaction of surface regions, the size of the cluster should be quite large. In fig. 2.2 I show a rough estimate of the cluster necessary to mimic the bulk behavior under the adsorbate. If the adsorbed molecule itself is large, the requirements become even more challenging, and the model still misses the solid-state electronic band structure. If the molecule induces charge transfer, a cluster tends to accumulate

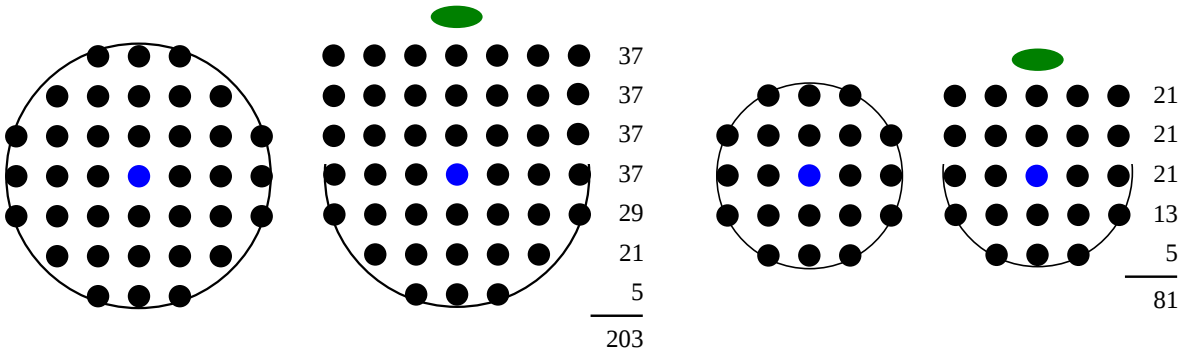

Figure 2.2: A cluster approximating a flat surface under an adsorbate, assuming the skin layer to contain 3 atomic layers (left) or 2 (right). The blue atom experiences bulk-like conditions, and the green ellipse denotes an adsorbate molecule. The number of atoms in each layer and the total number are given.

charge at the corners, which is unphysical. Therefore, we consider the cluster model impractical in most cases.

2.6.2 A slab in an external electric field

A more physical approximation for a surface is a slab in periodic boundary conditions, which is thick enough in the direction perpendicular to the surface. If we set an electric field, a thick slab will polarize so that it screens the field. Therefore, the condition for the slab thickness is to be larger than two skin-layers in order to get zero field in the middle of the slab. Since common electronic-structure codes do not allow to have a single non-periodic axis, an external electrostatic potential that generates the electric field must have a discontinuity. In order not to break any properties of the system, the discontinuity should be placed in a deep vacuum region, where there is no electron density (z_{vac} in fig. 2.3). One can show that such setup is equivalent to a capacitor cell with two electrodes fixed at a voltage $\Delta v = E * z_{\text{cell}}$ [2]. Such a setup is conceptually different from a real-world electric device. In a real device, say, a battery, the potential discontinuity is introduced by an electromotive force located *within* the conducting circuit, so that the electrostatic potential is positive on the positively charged electrode and negative on the negative one. In order to be consistent with the common convention, I will refer to the potential of the positively charged

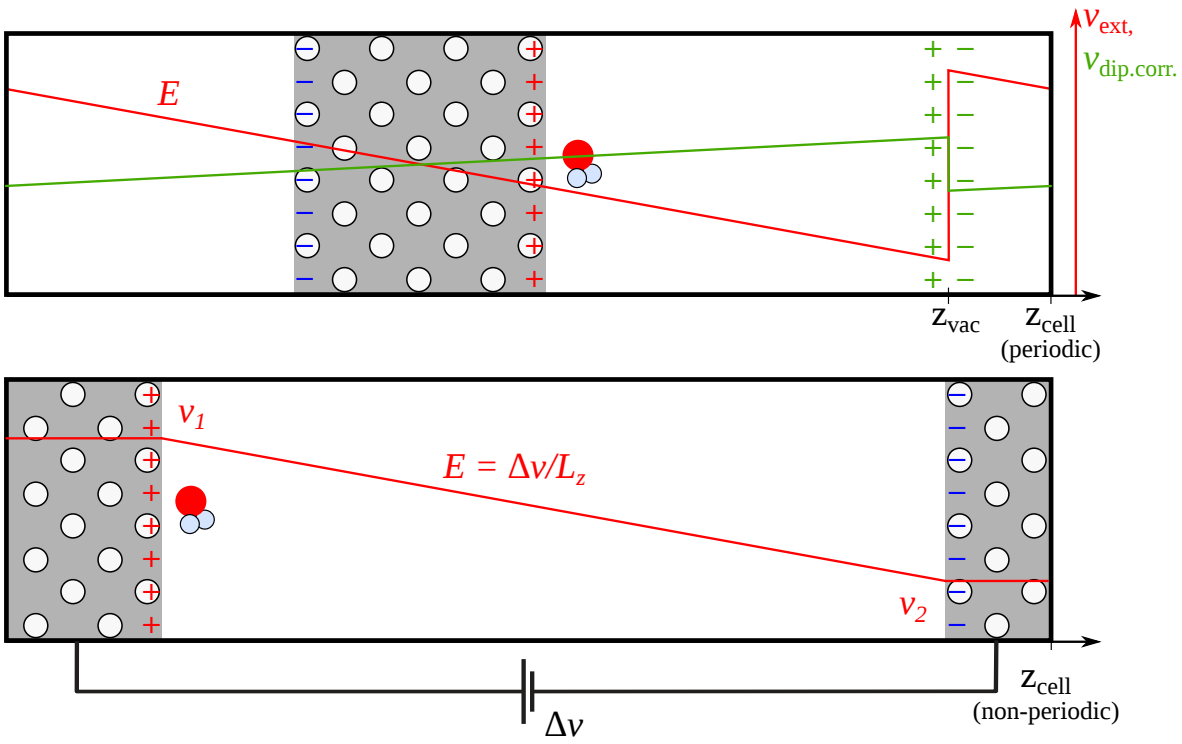

Figure 2.3: Top: a schematic representation of a slab in an external electric field with dipole correction [1] applied. The solid red line shows an external field, and the green line and charges show the potential of dipole correction and the counter-dipole which it mimics. Bottom: the equivalent 2D-periodic capacitor setup with two separately defined electrode potentials [2].

surface as positive.

Simulation of a slab in a periodic cell leads to spurious interaction between the slab dipole and its images along the z axis. In order to eliminate such interactions, one can use different techniques. One approach is to modify a solution of the Poisson equation and place semi-infinite dielectric media on both sides of a simulation cell [33, 119, 120]. This approach allows the use of a plane-wave basis set in essentially non-periodic conditions. Another approach is technically equivalent to the model for the electric field: one can calculate the total dipole of the simulation cell and add a counter-balancing electric field which corresponds to an oppositely-directed dipole placed in the vacuum region [1]. This technique is implemented in the FHI-aims code and was used in my calculations described in chapters 4 and 5.

2.6.3 Charge fluctuations in a simulation cell

A potentiostat approach

The slab model can be expanded to capture charge fluctuations on the surface more precisely if one removes the constraint of constant charge of the simulation cell. The potentiostat method proposed by Bonnet *et al.* in 2012 [3] does this separately from the SCF cycle: the charge is described as an additional degree of freedom and it can be exchanged between the system and the external reservoir (a potentiostat) which is held under a constant potential v_{PS}. The total energy of the system and a potentiostat is then the energy E of the system itself plus the cost of removing n_e electrons from the potentiostat:

$$\tilde{E} = E(\boldsymbol{R_i}, n_e) + n_e v_{\mathrm{PS}}. \tag{2.49}$$

Introducing fictitious mass M_{n_e} and momentum P_{n_e} for the charge degree of freedom (DOF), we get

$$\dot{n}_e = \frac{P_{n_e}}{M_{n_e}}, \quad \dot{P}_{n_e} = F_e = -\frac{\partial \tilde{E}}{\partial n_e} = \mu - v_{\mathrm{PS}}, \tag{2.50}$$

where $\mu \equiv -\partial E/\partial n_e$ is the electrode potential, i.e. the Fermi level of the simulation cell. F_e is then a thermodynamic force that acts on the charge in the direction to bring μ to v_{PS}. Such a system allows for oscillations of charge during the simulation, following the dynamics of a grand-canonical ensemble, while the effective screening medium

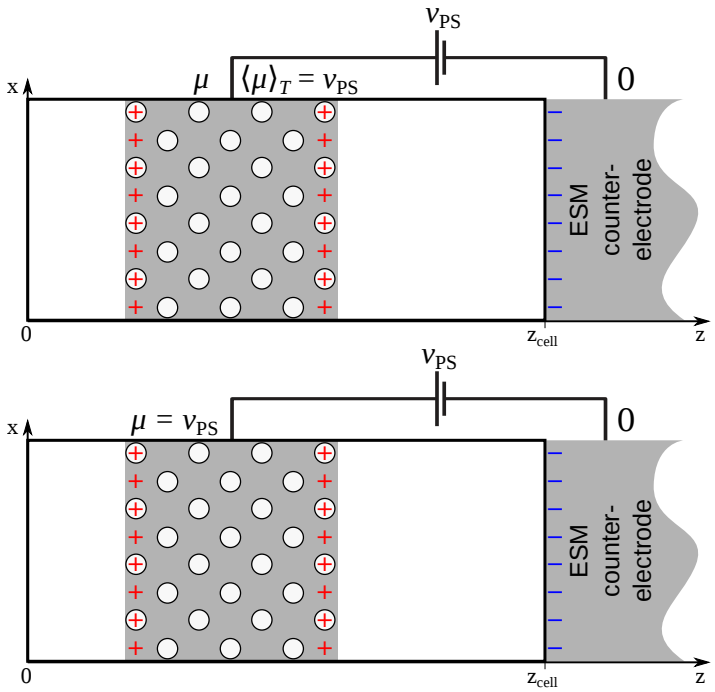

Figure 2.4: Schematic representation of a slab under a grand-canonical potentiostat of Bonnet *et al.* [3] (top) and grand-canonical SCF [4, 5] (bottom) with ESM.

(ESM) implicitly plays the role of a counter-electrode (see fig. 2.4), and its properties are defined analytically using a Green's function for the Poisson equation [33].

Grand-canonical self-consistent Kohn-Sham DFT

Otani and Sugino noted along with the introduction of ESM approach that the chemical potential can be imposed within the self-consistent Kohn-Sham procedure if the KS states are populated not up to a predefined number of electrons, but rather up to the desired potential:

$$\rho(\boldsymbol{r}) = \sum_{i}^{\epsilon_i \leq \mu} |\phi_i|^2 \tag{2.51}$$

with the symbols defined in 2.3. They noted, however, that this procedure is less stable than the interpolation of μ from multiple SCF calculations with a fixed number of electrons. Later, Sundararaman *et al.* developed a scheme to find the electron density [4], therefore one can expect that GCSCF method will become more common in the near future.

Electronic Green's functions formalism

Another method to simulate surfaces is with the use of Green's functions technique. The basic idea is to simulate a surface as a semi-infinite bulk consisting of periodically repeated "principal layers" (PL) and a non-periodic termination which includes a few layers of metal and an adsorbate, which we call "molecular part". We assume that all interactions are screened within a principal-cell distance, so that each principal layer (PL) interacts only with the adjacent PLs (see figure 2.5). Then, the Hamiltonian matrix of such a system has a block-3-diagonal form:

$$\mathcal{H} = \begin{pmatrix} ... & ... & ... & ... & ... \\ ... & \mathcal{H}_0 & \mathcal{H}_1 & 0 & 0 \\ ... & \mathcal{H}_{-1} & \mathcal{H}_0 & \mathcal{H}_1 & 0 \\ ... & 0 & \mathcal{H}_{-1} & \mathcal{H}_0 & \mathcal{H}_{BM} \\ ... & 0 & 0 & \mathcal{H}_{MB} & \mathcal{H}_M \end{pmatrix}, \tag{2.52}$$

where indices 0 and M correspond to interactions within the bulk PL and within the molecular part, respectively, while ± 1 and BM/MB correspond to the coupling between two adjacent PLs and between the last PL and the molecular part, respectively. A derivation of the Green's functions formalism is quite bulky and goes beyond the scope of this Thesis. I refer interested readers to the original papers [40, 43, 39]. In short, it is possible to construct the Green's function of such a semi-infinite system using the Bloch waves with real and imaginary k-vectors, which propagate or decay back and forth along the semi-infinite direction, and scatter on the "molecular" part. The Green's function gives access to the electron density at each energy value $\rho(\boldsymbol{r}, E)$ (or a reciprocal-space $\rho(\boldsymbol{k}, E)$), which can be integrated from $-\infty$ to the desired chemical potential μ, thus allowing the simulation of potential bias. The true power of GF method is that it can be straightforwardly extended to non-equilibrium systems, in which there are the source and the drain of electrons and a current flows through the system [121, 47, 48].

The main disadvantage of the GF method is its relatively high cost: integration in the energy domain has to be performed numerically and requires the calculation of the Green's function at each energy discretization point to perform a single iteration of the density. And each of those GF calculations implies inversion of a $N^{\mathrm{BS}} \times N^{\mathrm{BS}}$

matrix, where N^{BS} is a size of a basis set. It means in practice a factor of about 100 or more compared to the KS-DFT. Another problem which is so far not solved is the numerical stability of the SCF procedure: existing open-source general-purpose implementations [48, 44] are very sensitive to the initial guess for the electron density and even small perturbations, e.g. during geometry relaxation, may lead to divergence. These stability issues prevented me from using GF calculations in practical simulations.

2.7 Numerical solution of the electronic problem

The methods described above need to be implemented in a discrete form suitable for numerical solution. For efficient handling, the electron density should be expanded into a set of basis functions. For Kohn-Sham states ϕ_i and basis functions φ_j, it reads

$$\phi_i = \sum_j C_{ij}\varphi_j. \tag{2.53}$$

Different DFT codes choose different approaches for discretization. Popular basis sets are plane waves, atom-centered Gaussian functions and atomic-like orbitals. Plane-wave basis sets are orthogonal and easily convertible to the real space and back by fast Fourier transforms. They are also convenient for solid-state problems since the basis is naturally periodic. On the other hand, they have two important disadvantages. The first one is the non-locality of plane waves, which makes it difficult to describe heterogeneous systems like a slab in a vacuum. The second problem is that describing strong gradients of the density, which are to be expected near the nuclei, requires a very large number of harmonics. Therefore most plane-wave codes rely on pseudopotentials to describe the core electrons. Opposite to plane waves, localized basis sets are generally more efficient in describing core states and heterogeneous systems, but they need additional treatment to work in periodic boundary conditions, and, since they are non-orthogonal, the Kohn-Sham eigenproblem 2.15 takes the form

$$\sum_j \mathcal{H}_{ij}C_{jl} = \epsilon_l \sum_j S_{ij}C_{jl}, \tag{2.54}$$

where $\mathcal{H}_{ij}$ and S_{ij} are the Hamiltonian (see eq. 2.15) and overlap matrix elements, respectively, which are calculated by real-space integration on the grid:

$$\mathcal{H}_{ij} = \int d\boldsymbol{r}[\varphi_i^*(\boldsymbol{r})\mathcal{H}_{ij}^{\mathrm{KS}}\varphi_j(\boldsymbol{r})] \tag{2.55}$$

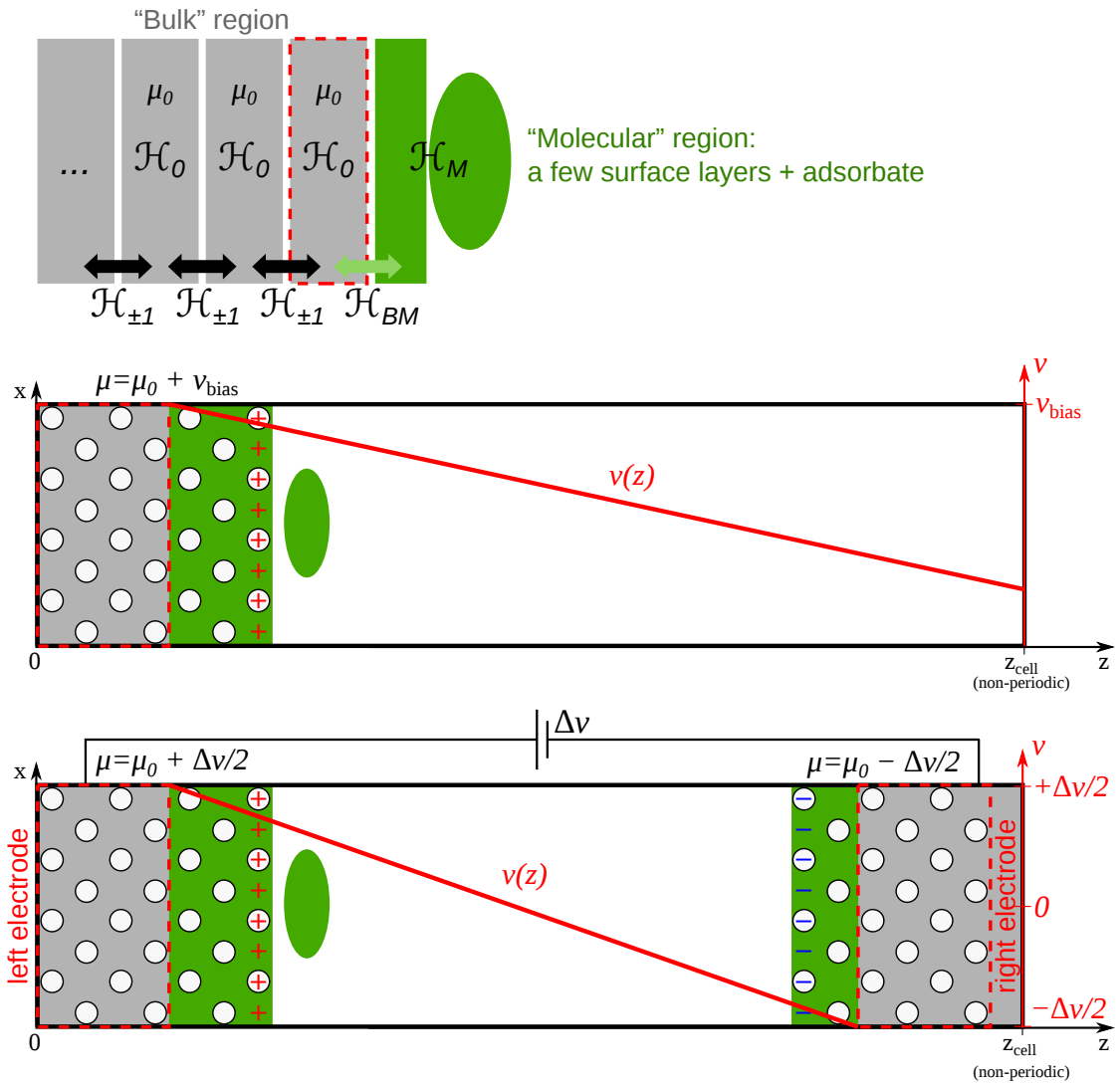

Figure 2.5: Schematic representation of a Green's function simulation setups. Top: division of a surface system into primitive blocks. The grey rectangles denote the principal layers of a bulk metal, and the green area – the non-periodic part consisting of a few metallic layers and an adsorbate. μ_0 is a Fermi level of the unbiased bulk. Middle: the simulation cell in a single-electrode setup with a potential bias applied. The red-dashed unit corresponds to the same in the top picture. Bottom: the simulation cell in a 2-electrode setup.

$$S_{ij} = \int d\boldsymbol{r}[\varphi_i^*(\boldsymbol{r})\varphi_j(\boldsymbol{r})] \tag{2.56}$$

During this work, I used mostly FHI-aims [36] code, and partially SIESTA [122]. Both use atom-centered atomic-like orbitals with a cutoff radius which makes the Kohn-Sham Hamiltonian and the overlap matrix sparse: the density overlap between the atoms beyond a cutoff distance is exactly zero. Real-space grids which host those tabulated orbitals are handled differently in these two codes: SIESTA uses a uniform grid spanning over the entire simulation cell, while FHI-aims uses atom-centered grids of increasing density towards the nuclei. The reason for that is that SIESTA simulates only the valence band explicitly and relies on pseudopotential to describe the lower shells, while FHI-aims includes all electrons explicitly. The species-specific basis sets in FHI-aims are organized in so-called "tiers" by increasing accuracy and computational cost, and several default settings are provided, called "light", "intermediate", "tight" and "really tight".

Treatment of periodic boundary conditions (PBC) in FHI-aims is done by constructing the Bloch-like states χ from the basis functions φ located in the unit cells translated by a translation vector $\boldsymbol{T}(\boldsymbol{N})$, $\boldsymbol{N} = (N_1, N_2, N_3)$:

$$\chi_{i,\boldsymbol{k}}(\boldsymbol{r}) = \sum_N \exp[i\boldsymbol{k} \cdot \boldsymbol{T}(\boldsymbol{N})] \cdot \varphi_i[\boldsymbol{r} - \boldsymbol{R}_{\mathbf{at}} + \boldsymbol{T}(\boldsymbol{N})] \tag{2.57}$$

The corresponding $\boldsymbol{k}$-dependent matrix elements $h_{ij}(\boldsymbol{k})$ are

$$\mathcal{H}_{ij}(\boldsymbol{k}) = \langle \chi_{i,\boldsymbol{k}} | \hat{\mathcal{H}}^{\mathrm{KS}} | \chi_{i,\boldsymbol{k}} \rangle = \sum_{\boldsymbol{M},\boldsymbol{N}}{}' \exp[i\boldsymbol{k} \cdot (\boldsymbol{T}(\boldsymbol{N}) - \boldsymbol{T}(\boldsymbol{M})] \cdot \int_{\mathrm{u.c.}} d\boldsymbol{r}\, \varphi_{i,\boldsymbol{M}}(\boldsymbol{r}) \hat{\mathcal{H}}^{\mathrm{KS}} \varphi_{j,\boldsymbol{N}}(\boldsymbol{r}), \tag{2.58}$$

where $\varphi_{j,\boldsymbol{M}}$, $\varphi_{j,\boldsymbol{N}}$ are the basis functions located in the $\boldsymbol{M}$th ($\boldsymbol{N}$th) unit cell. Because of the locality of the basis functions, the $\sum'_{\boldsymbol{M},\boldsymbol{N}}$ sum runs not over the infinite amount of cells, but only over a quite small set of those which have nonzero elements of the Hamiltonian and overlap matrices. This scheme turns out to be computationally efficient.

Chapter 3

Theory and methods for nuclear motion

Within the Born-Oppenheimer approximation, nuclei move subject to forces arising from nuclear-nuclear Coulomb repulsion and from the electron-nuclear interaction given by a single state of the electronic subsystem, which corresponds to the instant position of nuclei. "Position" here should be understood in a broad sense, meaning that nuclei can be described as quantum particles or approximated classically. Similarly to electrons, an analytical solution of the Schödinger equation for nuclei hits the dimensionality wall. One could reasonably propose to treat nuclear density in a way ideologically similar to KS-DFT. Two reasons make this approach impractical. The first one is that the nucleus-nucleus interaction is mediated by electrons via the Born-Oppenheimer potential energy surface, which has neither an analytical form nor a reasonably simple analytical approximation. The second problem is that the nuclear subsystem has multiple excitations with energies small compared to temperature. For example, the lowest rotational level of a water molecule lies at 28 cm^{-1}, which corresponds to 33 K [123]. It implies the need for at least time-dependent DFT treatment, which is computationally demanding. Alternatively, only some nuclear degrees of freedom are treated quantum-mechanically, and others classically. Although there are developments in the direction of electron-nuclear DFT [124, 125], it is far from being common approach. Instead, other methods are applied to solve the nuclear problem, and the level of theory depends on the properties that we are interested in. In my

work, I focused on equilibrium properties and chemical reaction rates. In the following sections, I will briefly review the theory which is applicable in these two cases.

3.1 Statistics of quantum nuclei

Within the BO approximation, the nuclear Hamiltonian is a function of the coordinates and momenta of nuclei $\hat{\mathcal{H}}(\hat{\boldsymbol{R}}, \hat{\boldsymbol{p}})$. Equilibrium statistical mechanics of a canonical ensemble of systems with N distinguishable nuclei each is described by the Gibbs partition function

$$Q(\beta) = \mathrm{Tr}\left[\mathrm{e}^{-\beta\hat{\mathcal{H}}}\right] = \sum_n \mathrm{e}^{-\beta E_n}. \tag{3.1}$$

where $\beta = 1/k_\mathrm{B}T$ and E_n are the eigenvalues of $\hat{\mathcal{H}}$, and the trace is taken in the eigenstate basis of $\hat{\mathcal{H}}$. Finding a partition function is thus identical to finding the spectrum of the Hamiltonian. Very few multidimensional Hamiltonians are easy to solve. In the following two sections, I will first discuss the most common analytical approximation, i.e. the harmonic approximation, and then I will review the treatment of arbitrary Hamiltonians by path integral molecular dynamics.

3.1.1 Harmonic and quasi-harmonic approximations

The harmonic approximation starts with the assumption that a molecular system, say, a molecule in a gas phase or a solid, performs small oscillations around its minimal energy position. It means that the temperature is much lower than the energy of possible chemical transformations, such as bond rotations or breaking. In many cases, it is a reasonable assumption, because characteristic reaction energies are in the range of hundreds of meVs and above, which is equivalent to the temperature of thousands of kelvins. Then, we can approximate the potential energy part of the Hamiltonian by a series expansion around the minimal energy position. The first non-zero term is of second order in $\boldsymbol{R}$[1], and we arrive at the harmonic vibrational Hamiltonian

$$\mathcal{H}_\mathrm{harm} = \sum_i^{N^\mathrm{DOF}} \frac{\hat{p_i}^2}{2m_i} + \frac{1}{2}\sum_{i,j}^{N^\mathrm{DOF}} \Phi_{ij}\hat{R}_i\hat{R}_j. \tag{3.2}$$

[1]We can always choose potential energy $V:\ V^\mathrm{eq} = 0$, and coordinates $\boldsymbol{R}:\ \boldsymbol{R}^\mathrm{eq} = \boldsymbol{0}$.

Here N^{DOF} is the number of degrees of freedom, which is $(3N-\alpha)$ with α depending on the constraints which our system is subject to. A macroscopically constrained crystal has $\alpha = 0$, a molecule in a vacuum has $\alpha = 5$ (linear molecule) or $\alpha = 6$ (nonlinear), and some exotic systems may have different numbers[2]. Φ_{ij} is an element of the so-called Hessian matrix $\partial^2\mathcal{H}/\partial R_i \partial R_j$. We can make a transformation $\boldsymbol{R} \to \boldsymbol{\xi}$ which diagonalizes the Hessian. I will keep using p_i and m_i for simplicity, but note that they were transformed also to satisfy the new commutation relations $[\hat{\xi}_i, \hat{p}_i] = i\hbar$. In the eigenbasis of $\mathbf{\Phi}$, the Hamiltonian looks simpler:

$$\mathcal{H}_{\mathrm{harm}} = \sum_i^{N^{\mathrm{DOF}}} \frac{\hat{p_i}^2}{2m_i} + \frac{1}{2}\sum_i^{N^{\mathrm{DOF}}} m_i\omega_i^2\hat{\xi_i}^2 \tag{3.3}$$

The N^{DOF}-dimensional problem is transformed into many 1D problems. Since we know the eigenvalues of a single harmonic oscillator $E_n = (n+1/2)\hbar\omega$, we can immediately substitute them into 3.1 and get the partition function and useful observables:

$$Q(\beta) = \prod_i^{N^{\mathrm{DOF}}} \sum_n^{\infty} \mathrm{e}^{-\beta(n+1/2)\hbar\omega_i} = \prod_i^{N^{\mathrm{DOF}}} \frac{\mathrm{e}^{-\beta\hbar\omega_i/2}}{1-\mathrm{e}^{-\beta\hbar\omega_i}}; \tag{3.4}$$

Harmonic free energy:

$$F_{\mathrm{harm}} = -\frac{1}{\beta}\ln Q = \sum_i^{N^{\mathrm{DOF}}} \frac{\hbar\omega_i}{2} + \frac{1}{\beta}\ln(1-\mathrm{e}^{-\beta\hbar\omega_i}); \tag{3.5}$$

Total energy:

$$E = -\frac{\partial}{\partial\beta}\ln Q = \sum_i^{N^{\mathrm{DOF}}} \hbar\omega_i\left(\frac{1}{2} + \frac{\mathrm{e}^{-\beta\hbar\omega_i}}{1-\mathrm{e}^{-\beta\hbar\omega_i}}\right) \tag{3.6}$$

The $\hbar\omega/2$ contribution is very important and has a purely quantum nature: as one can see, it exists even at zero temperature, thus the lowest energy state that a system can occupy is not zero. Instead, it exhibits fluctuations in the position space that satisfy the Heisenberg uncertainty relation. This energy contribution is called ZPE.

Quasi-harmonic approximation

In certain anharmonic systems, it is possible to separate a single anharmonic degree of freedom or a small number of them so that the other DOFs can be treated as harmonic

[2]For example, gas-phase molecules can have constrained translations (in an ion trap) or some of the rotations, if a strong orienting field is present.

ones. One well-known example is the thermal expansion of the crystal lattice. The vibrational energy of a crystal can be approximated harmonically quite well, however, in doing so we are not able to capture thermal expansion, as the mean position of atoms in a harmonic crystal (so-called Debye crystal) remains the same at any temperature. What we can do to overcome this problem, is to calculate multiple harmonic crystals corresponding to different lattice constants, then to obtain their free energy depending on temperature and thus to find the preferred lattice constants for each temperature as the ones that minimize the free energy. Another example is described in Chapter 4, where we treat the distance between the adsorbate and the surface as a parameter, and all the other DOFs harmonically to capture isotope effects in the adsorption distance. Eyring's transition state theory, which is discussed in section 3.2.1, and Vineyard's formulation of it for solids [51] are other examples of a quasi-harmonic approximation, because all but one normal modes at the saddle point are treated harmonically.

3.1.2 Path Integral Molecular Dynamics

If the nuclear DOFs of a system move in a considerably anharmonic potential, e.g. when a system has multiple energy minima within an energy range of few $k_{\mathrm{B}}T$ and migrates between them easily, the harmonic approximation to the potential energy surface (PES) may perform poorly, and other methods are needed to access quantum statistical properties. Let us consider a one-dimensional system with a Hamiltonian $\mathcal{H} = \hat{T} + \hat{V}$. The extension to higher dimensions doesn't change the basic ideas of the following derivation. In the position basis, partition function (3.1) reads

$$Q(\beta) = \int_{-\infty}^{+\infty} \langle x|\mathrm{e}^{-\beta\hat{\mathcal{H}}}|x\rangle dx \tag{3.7}$$

In a position representation, $\hat{V}$ can be evaluated straightforwardly, but $\hat{T}$ cannot. We would like to split $\hat{V}$ and $\hat{T}$, but since they do not commute, we cannot simply factorize the exponent. We circumvent this by applying the Trotter theorem (1959) [126]. This theorem states that for two operators $\hat{A}$ and $\hat{B}$, for which $[\hat{A}, \hat{B}] \neq 0$,

$$\mathrm{e}^{\hat{A}+\hat{B}} = \lim_{P\to\infty} \left[\mathrm{e}^{\hat{B}/2P}\mathrm{e}^{\hat{A}/P}\mathrm{e}^{\hat{B}/2P}\right]^P. \tag{3.8}$$

Then,

$$Q(\beta) = \lim_{P\to\infty} \int_{-\infty}^{+\infty} \langle x| \left[\mathrm{e}^{-\beta\hat{V}/2P}\mathrm{e}^{-\beta\hat{T}/P}\mathrm{e}^{-\beta\hat{V}/2P}\right]^P |x\rangle dx. \tag{3.9}$$

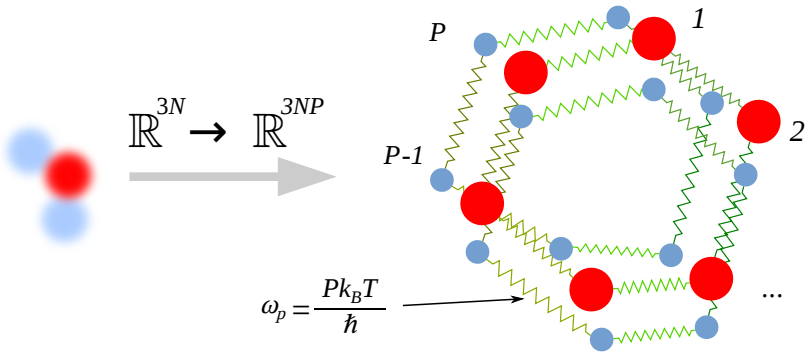

Figure 3.1: Ring polymer representation of a single water molecule. Instead of delocalized coordinates in $3N$ dimensions, the system has classical coordinates in $3N * P$ dimensional space. The "springs" come from the expression (3.12).

Inserting the identity operator $\hat{\mathbb{I}} = \int |x_{(k)}\rangle\langle x_{(k)}| dx$ between each of P multipliers and integrating out the kinetic energy terms, we get an expression that is, in its limit, identical to the partition function of another P-dimensional physical system [127]:

$$Q(\beta) = \lim_{P\to\infty} Q_P, \tag{3.10}$$

$$Q_P = \left(\frac{mP}{2\pi\beta\hbar^2}\right)^{P/2} \int dx_{(1)} \dots dx_{(P)} \mathrm{e}^{-\beta_P U_P(x_{(1)},\dots,x_{(P)})}, \tag{3.11}$$

$$U_P(x_{(1)},\dots,x_{(P)}) = \sum_{k=1}^{P} \frac{1}{2} m\omega_P^2 \left(x_{(k+1)} - x_{(k)}\right)^2 + V(x_{(k)}) \tag{3.12}$$

with m being the mass of the particle, $\beta_P = \beta/P$, $\omega_P = (\hbar\beta_P)^{-1}$ and $x_{(P+1)} = x_{(1)}$. One can see that U_P has a form of a ring chain of P particles connected by harmonic springs with stiffness $m\omega_P^2$ (see fig. 3.1). This object is typically called a "ring polymer", and its individual particles $x_{(k)}$ are "beads"[3].

Having the partition function, we can calculate any observable A which doesn't depend on momentum:

$$\begin{aligned}\langle A\rangle &= \frac{1}{Q(\beta)} \mathrm{Tr}\left[\hat{A}\mathrm{e}^{-\beta\mathcal{H}}\right] = \frac{1}{Q(\beta)} \int A(x)\langle x|\mathrm{e}^{-\beta\hat{\mathcal{H}}}|x\rangle dx \\ &= \lim_{P\to\infty} \frac{1}{Q_P} \left(\frac{mP}{2\pi\beta\hbar^2}\right)^{P/2} \int dx_{(1)} \dots dx_{(P)} \left[\frac{1}{P}\sum_{k=1}^{P} A(x_{(k)})\right] \mathrm{e}^{-\beta_P U_P(x_{(1)},\dots,x_{(P)})}.\end{aligned} \tag{3.13}$$

[3]For clarity, I will use bracketed indices (k) to indicate indexing over the dimensions of a ring polymer or over its normal modes. It has the same mathematical meaning as usual indexing.

Although only the limit $P \to \infty$ makes the ring polymer formalism exact, in practice, P is a convergence parameter, and including more and more beads we asymptotically approach the exact answer.

Thus, we have reformulated the problem of equilibrium properties of a quantum system into the problem of eq. properties of a classical system. This relation is referred as "classical isomorphism" [128]. One can notice some similarity between this approach, where the state of a quantum system is probed by multiple classical "instances" of the system, and the Feynman path integral formalism, in which a particle moves from one point to another along all possible trajectories simultaneously. Indeed, Feynman showed that statistical mechanics can be formulated in terms of path integrals if we rotate the time axis into the imaginary plane and consider only closed trajectories [129]. The Boltzmann operator $\mathrm{e}^{-\beta\hat{\mathcal{H}}}$ is formally equivalent to the time propagation operator $\mathrm{e}^{-i\hat{\mathcal{H}}\tau/\hbar}$, if we set $\tau = -i\hbar\beta$. From such a perspective, a ring polymer is a discretization of the Feynman path in imaginary time which starts and ends at the same point. Therefore, the ring polymer method for equilibrium properties received the name "path integral molecular dynamics" (PIMD)[4] or "path integral Monte-Carlo" (PIMC), depending on the way how we perform integration in (3.13). The Monte-Carlo (MC) approach is a straightforward numerical integration. The problem that one faces here is typical for MC methods: although the integral will eventually converge, sampling a high-dimensional space with Boltzmann weights requires calculating the potential energy, which is computationally expensive. The Metropolis algorithm [130] introduces importance sampling into the MC integration, and the maximal allowed Metropolis step becomes a control parameter which gradually transforms the original randomized MC into a very conservative localized sampling technique, which is somewhat reminiscent of molecular dynamics. Another approach was proposed by Parrinello and Rahman in 1984 [72]: since the ring polymer that we have constructed is a classical system, we can construct its Hamiltonian by reintroducing momenta and sample the equilibrium distribution just as we do in standard MD method. Parrinello-Rahman method appeared to be robust enough and became a de facto standard in the commu-

[4]One could say that "ring polymer molecular dynamics" is just as valid, but this label tends to be used for some approximations to *real*-time path integral methods

nity and a base for various improvements. It is important to remember, though, that it is derived for distinguishable particles and does not include nuclear exchange effects, and therefore cannot explain such phenomena as the superfluidity of liquid helium. Developments in the direction of modeling of indistinguishable particles go beyond the scope of this brief description.

Performance and acceleration of PIMD

For distinguishable particles, PIMD scales linearly with both the number of beads P and the number of particles N. Each atom of each bead interacts physically only with the atoms of the same bead and interacts by the springs only with the two nearest neighboring repetitions of itself. It means that for each bead PIMD imposes a negligible additional cost on top of the computation of the energy and forces within that bead, and the bottleneck of scaling remains in the calculation of single beads. Nevertheless, PIMD has new directions for acceleration in addition to standard MD techniques, which all aim at the same goal: reduce the number of calculations of the bead energies and forces.

A fruitful tree of methods stems from the generalized Langevin equation (GLE) thermostat with frequency-dependent noise [131, 132] (so-called colored noise, in contrast to the white noise in the original Langevin thermostat [133, 134]). Originally, Generalized Langevin eqiation (GLE) thermostats were designed to enhance sampling from the NVT ensemble in classical MD simulations, but later the same concept was expanded to quantum systems. One way is to introduce a thermostat which modifies the movement of classical particles so that it yields quantum statistics to a certain extent. The idea of the quantum thermostat (QT) [135] is to approximate the quantum statistics by exciting modes of a system at each frequency so that their fluctuations have a distribution corresponding to quantum fluctuations. For a single 1D QHO with frequency ω, the mass-scaled coordinate $\tilde{x} = x/\sqrt{m}$ and corresponding momentum $\tilde{p} = p\sqrt{m}$, quantum fluctuations have expectation values

$$\langle \tilde{p}^2 \rangle = \langle \omega^2 \tilde{x}^2 \rangle = \frac{\hbar\omega}{2} \coth\left(\frac{\hbar\omega}{2k_{\mathrm{B}}T}\right). \tag{3.14}$$

Having access to frequency-dependent dynamics, one can construct a thermostat that excites a multidimensional system according to all its frequencies.

In the case of PIMD, there are a few ways of applying (G)LE thermostats. The minimal necessary way is just to apply a white-noise Langevin thermostat to enforce the NVT ensemble on a ring polymer in order to satisfy the definition of PIMD. Such a way does not use special features of a ring polymer. Another, still quite simple way is to use the properties of a free ring polymer – a polymer without any physical forces acting on atoms. For a free ring polymer, one can perform analytical transformation to its normal modes: $\tilde{\boldsymbol{x}} = \{\tilde{x}_{(1)}, ..., \tilde{x}_{(P)}\} \rightarrow \boldsymbol{q} = \{q_{(1)}, ..., q_{(P)}\}$. Then, it is possible to apply Langevin thermostats on the normal modes separately, using the optimal parameters for each particular eigenfrequency $\omega_{(k)}$, with the only arbitrary parameter for a zero-frequency centroid mode – just as it would be required in classical MD with LE thermostat [136].

Alternatively, one can recast the QT for PIMD. Then, the fluctuations $\langle \tilde{x}^2 \rangle$ are obtained from a sum over the ring polymer normal modes:

$$\langle \tilde{x}^2 \rangle_P = \frac{1}{P} \sum_{k=0}^{P-1} \langle q_{(k)}^2 \rangle = k_\mathrm{B} T \sum_{k=0}^{P-1} \frac{1}{\omega_{(k)}^2} \xrightarrow{P \to \infty} \frac{\hbar}{2\omega} \coth\left(\frac{\hbar\omega}{2k_\mathrm{B}T}\right). \tag{3.15}$$

A single GLE thermostat is fitted to be applied on each bead separately so that the sum over the beads yields correct fluctuations. This approach was named PI+GLE [137].

Finally, one can improve PI+GLE further by imposing correct fluctuations for kinetic energy in addition to the fluctuations of positions and potential energy. Quantum kinetic energy K of a 1D QHO can be estimated by the centroid virial estimator [138, 139]

$$\begin{aligned} \langle K \rangle &= \frac{k_\mathrm{B}T}{2} + \frac{1}{2P} \sum_{k=0}^{P-1} \langle (q_{(k)} - \bar{q}) \cdot \nabla V(q_{(k)}) \rangle = \frac{k_\mathrm{B}T}{2} + \frac{1}{2P} \sum_{k=0}^{P-1} \langle (q_{(k)} - \bar{q}) \cdot \omega^2 q_{(k)} \rangle \\ &= \frac{k_\mathrm{B}T}{2} + \frac{\omega^2}{2P} \sum_{k=0}^{P-1} \langle q_{(k)}^2 \rangle - \frac{\omega^2}{2P} \left\langle \bar{q} \sum_{k=0}^{P-1} q_{(k)} \right\rangle = \frac{k_\mathrm{B}T}{2} + \frac{\omega^2}{2P} \sum_{k=0}^{P-1} \langle q_{(k)}^2 \rangle - \frac{\omega^2 \langle \bar{q}^2 \rangle}{2} \\ &= \frac{k_\mathrm{B}T}{2} + \langle V \rangle - \frac{\omega^2 \langle \bar{q}^2 \rangle}{2}, \end{aligned} \tag{3.16}$$

where $\bar{q} = \frac{1}{P} \sum_k q_{(k)}$ is a centroid coordinate of a ring polymer. It is easy to see that in order to have $\langle K \rangle = \langle V \rangle$, the centroid coordinate should have the classical distribution. Therefore, a path integrals with generalized Langevin equation (PIGLET) method [140] applies a classical thermostat to the centroid and the GLE constructed to satisfy eq. 3.15 to the other normal modes. Fitting all aforementioned GLE thermostats

can be quite tedious, a reader may find it in the original papers and their supplemental materials.

One common vulnerability of all aforementioned thermostats is that they are derived targeting harmonic systems and also use the normal modes of a free ring polymer, ignoring their possible coupling to the physical system. However, they are applied quite successfully and speed up convergence both in the length of MD trajectories and in the number of beads.

Another method to reduce the number of energy/force calculations, which is specific to PIMD, is a ring polymer contraction of various kinds [141, 142]. The underlying idea is that it is sometimes possible to decompose interatomic interactions into a long-range "less quantum" (slowly varying in imaginary time) part and a short-range more quantum (rapidly varying in imaginary time) part. Then, the long-range part can be evaluated on a contracted ring polymer which has fewer beads, while the short-range part is approximated with some cheaper potential. For a multidimensional system with nuclear coordinates $\boldsymbol{R}$, it reads:

$$\sum_{k=1}^{P} V\left(\boldsymbol{R}_{(k)}\right) \approx \frac{P}{P'} \sum_{k=1}^{P'} \left[V\left(\boldsymbol{R}'_{(k)}\right) - V^{\text{short}}\left(\boldsymbol{R}'_{(k)}\right)\right] + \sum_{k=1}^{P} V^{\text{short}}\left(\boldsymbol{R}_{(k)}\right), \tag{3.17}$$

where $\{\boldsymbol{R}_{(k)}\}$, $k \in \{1, .., P\}$ are the original coordinates of a ring polymer, and $\{\boldsymbol{R}'_{(k)}\}$, $k \in \{1, .., P'\}$ are the coordinates of a contracted ring polymer with P' beads, which is obtained from the Fourier transform of the original system by neglecting its $(P - P')$ higher modes and transforming back. One variant of a contraction that we used in this work is a spatially localized ring polymer contraction (SL-RPC), schematically depicted in figure 3.2. In weakly bound interfaces, one can approximate the overall interactions quite accurately by separating intramolecular interactions from molecule-surface interaction. Since the atoms of the surface are heavy, quantum effects are negligibly small within the surface, and therefore one can use much fewer beads to describe the surface. Since the bonds between molecule and surface are weak, the high-frequency vibrations of the molecule, where the quantum effects are the most pronounced, are defined by intramolecular interactions. The potential energy (and the corresponding forces) of the full system of P beads is approximated as a superposition of P replicas of the molecular part, $P' \ll P$ replicas of the full system, and additional

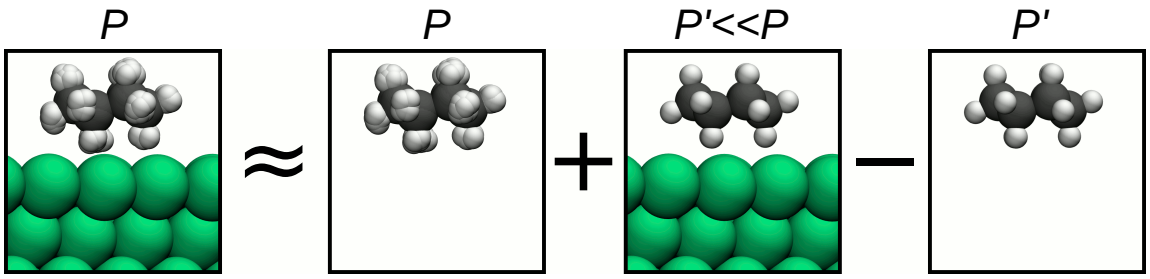

Figure 3.2: A scheme of the spatially localized ring polymer contraction (SL-RPC). The forces for a full ring polymer of P beads are approximated by a superposition of forces calculated for P beads at the molecular part, $P' < P$ beads of the full system, and a correction of P' beads at the molecular part.

P' of the molecular part with a negative sign, i.e.

$$V_P(\boldsymbol{R}) \approx \frac{P}{P'} \sum_{k=1}^{P'} \left[V_{\text{full}}(\boldsymbol{R}'^{\text{full}}_{(k)}) - V_{\text{mol}}(\boldsymbol{R}'^{\text{mol}}_{(k)}) \right] + \sum_{k=1}^{P} V_{\text{mol}}(\boldsymbol{R}^{\text{mol}}_{(k)}), \tag{3.18}$$

where "full" denotes the full system containing the surface and adsorbed molecules, and "mol" denotes the adsorbate simulated in the same unit cell, but without the surface.

This approximation, of course, does not come without errors. We can estimate the error which arises from SL-RPC by looking at how much the normal modes of the molecule change in proximity to the surface. [143]

$$\delta E^{\text{RPC}} = E^{\text{RPC}} - E^{\text{P beads}} = \sum_{i=1}^{3N} \frac{k_B T}{2} \sum_{k=P'}^{P-1} \left[\frac{\omega^2_{\text{mol}}}{\omega^2_{(k)} + \omega^2_{i,\text{mol}}} - \frac{\omega^2_{\text{full}}}{\omega^2_{(k)} + \omega^2_{i,\text{full}}} \right], \tag{3.19}$$

where $\{\omega_{i,\text{mol}}\}$ are the normal modes of the isolated adsorbate, and $\{\omega_{i,\text{full}}\}$ are the corresponding modes calculated by diagonalization of the part of Hessian matrix that describes molecular displacements. Equation 3.19 is slightly different from eq. 9 in the original paper [143], because I did not make the assumption of $\omega^2_{i,\text{mol}} - \omega^2_{i,\text{full}} \ll \omega^2_{(k)} + \omega^2_{i,\text{full}}$, as discussed in Appendix A.1.

Similarly, one can estimate the error in a harmonic quantum free energy at finite temperatures as

$$\delta F^{RPC} = \frac{1}{2\beta} \sum_{i=1}^{3N} \sum_{k=P'}^{P-1} \ln \left(1 + \frac{\omega^2_{i,\text{full}} - \omega^2_{i,\text{mol}}}{\omega^2_{(k)} + \omega^2_{i,\text{mol}}} \right), \tag{3.20}$$

the derivation is given in Appendix A.2.

A similar idea of separating slowly and fast varying parts of the potential may be applied to the real time axis (where these techniques have existed for much longer): the long-range part of the potential, e.g. Coulomb interaction, is expected to change slowly with time, which allows to use multiple-time stepping techniques and to update the "slow" part of a potential once in a few steps of "fast" varying potential [144, 145]. Typically, the problem here is to find an appropriate "fast" potential. The fastest vibrations correspond to covalent bonds, such as O-H and C-H, which implies that the fast potential must be both cheap to calculate and at the same time capable of describing intramolecular interactions, which in many cases is hard to fulfill.

3.2 Analysis of reaction pathways

In this section, I will discuss the problems appearing when one deals with the central problem of chemical kinetics: the calculation of reaction rates. For a hypothetical set of molecular compounds, A_i constituted from a given set of atoms, there are many possible reactions

$$A_i \rightarrow A_j, i, j \in \{1..M\}. \tag{3.21}$$

where M is the number of possible compounds. The problem then can be formulated very generally as the time evolution of the vector of the corresponding concentrations $\boldsymbol{n} = (n_1, n_2, ..., n_M)$:

$$\begin{aligned} \boldsymbol{n}(0) &= \boldsymbol{n_0} \\ \boldsymbol{n}(t) &= ? \end{aligned} \tag{3.22}$$

If we assume that populations n_i do not affect the probabilities of transition between the states A_i, we can write the Markovian master equation for this problem:

$$\frac{d\boldsymbol{n}}{dt} = \boldsymbol{A}\boldsymbol{n}, \tag{3.23}$$

where we collected the rates of individual transitions into the time-independent matrix $\boldsymbol{A}$. Then, the solution of the general problem boils down to determining all the matrix elements A_{ij}.

It is useful to remember that what we called "molecular compounds" A_i, are, in fact, the local minima of energy in the conformational space of the considered set of

atoms. These minima are surrounded by their basins of attraction, which are separated from each other by ridges. If the system has $3N$ degrees of freedom, then each ridge has $3N-1$ dimensions. Depending the height and the width of these ridges, one can use different approximations to find transition rates. If a barrier is comparable to or lower than the average kinetic energy of considered particles, one has to solve it as a scattering problem. If a barrier, in contrast, is much higher than the kinetic energy, the system will tend to spend a long time in a certain basin of attraction. In such a case, one can assume that the system reaches local equilibrium in that basin, and then, the Boltzmann statistics can be applied to describe the system within the basin. If the barrier is not wide enough to sufficiently suppress the under-barrier tail of the wave function before it reaches another basin, one has to consider tunneling, but such a case goes beyond the scope of this thesis. In the next sections, I will discuss the case of a high barrier by first setting the theoretical stage based on the so-called saddle point approximation, and then showing the computational methods used in practice.

3.2.1 Saddle point approximation

As stated in the previous section, the task of finding reaction rates can be formulated as a problem of two basins of attraction with a ridge that separates them. If we assume local thermodynamic equilibrium in the basin of reactants, then the relative probability p that the system reaches energies E_1 and E_0 obeys the well-known Boltzmann distribution:

$$\frac{p(E_1)}{p(E_0)} = p(\Delta E) = \exp\left(-\frac{\Delta E}{k_\mathrm{B}T}\right) \tag{3.24}$$

We can take the energy of the lowest point of the basin as E_0 and consider ΔE only. If we integrate over all possible microscopic states at the $(3N-1)$-dimensional ridge hyperplane, we obtain the total probability that the system reaches the ridge. Although this sounds clear, doing such integration in practice poses a significant problem. In addition to high dimensionality, the ridge hyperplane and its energy have no analytical representation in most cases. The same task of integrating functions multiplied by the Boltzmann exponent appears in many problems of statistical physics. The idea is very simple: since the exponent is a fast-decaying function, the most significant contribution comes from the points on the ridge hyperplane where ΔE takes its lowest

value. Then, we can employ Laplace's method [146] and approximate the potential energy landscape around the point with the lowest barrier up to the second order. The resulting value of the integral is proportional to the probability $p(\Delta E_0)$ to find the system having the energy of a saddle point ΔE_0 (also known as activation energy E_a). This simple model evolved since 1884 by the efforts of J. H. van 't Hoff [147], S. A. Arrhenius [148] and many others, until H. Eyring proposed its modern form in the 1930s, which is now known as transition state theory (TST) [49, 50]. The transition state theory (TST) gives a practical way to calculate the probability to reach the saddle point by calculating the partition function at the ground state and at the saddle point. For any given system in the gas phase, there are 3 translational degrees of freedom, 2 or 3 rotational ones, and the rest $(3N-6)$ or $(3N-5)$ are the vibrational ones. If we assume the ideal gas behavior, separability of rotational and vibrational states, treat a molecule as a rigid rotor, and assume vibrations to be harmonic, we end up with the following well-known expressions for their partition functions:

$$Z^{\text{transl}} = \prod_{\alpha} \frac{\sqrt{2\pi m k_{\text{B}} T} L_\alpha}{h} \tag{3.25}$$

with L_α being the "box length" available for free translation along the axis α;

$$Z^{\text{rot (linear)}} = \frac{8\pi^2 I k_{\text{B}} T}{\sigma h^2}, \tag{3.26}$$

$$Z^{\text{rot (nonlinear)}} = \frac{\sqrt{\pi I_A I_B I_C}}{\sigma} \left(\frac{8\pi^2 k_{\text{B}} T}{h^2} \right)^{3/2} \tag{3.27}$$

with σ being the symmetry number of a molecule, and I (I_α) being the moment(s) of inertia of a linear (non-linear) molecule;

$$Z^{\text{vib}} = \prod_{i}^{3N-6(5)} \frac{\exp\left(-\frac{\hbar\omega_i}{2k_{\text{B}}T}\right)}{1-\exp\left(-\frac{\hbar\omega_i}{k_{\text{B}}T}\right)} \tag{3.28}$$

with ω_i being the angular frequency of the i-th vibrational normal mode.

Combining all the terms together, we get an expression for the relative concentration of "activated complexes":

$$\frac{n_1}{n_0} = \frac{Z_1^{\text{transl}} \times Z_1^{\text{rot}} \times Z_1^{\text{vib}}}{Z_0^{\text{transl}} \times Z_0^{\text{rot}} \times Z_0^{\text{vib}}} \times \exp\left(-\frac{\Delta E}{k_{\text{B}} T}\right). \tag{3.29}$$

In addition to this, a factor of roughly 1/2 has to appear in the expression for the reaction rate in order to respect the fact that it's not enough to reach the ridge – the

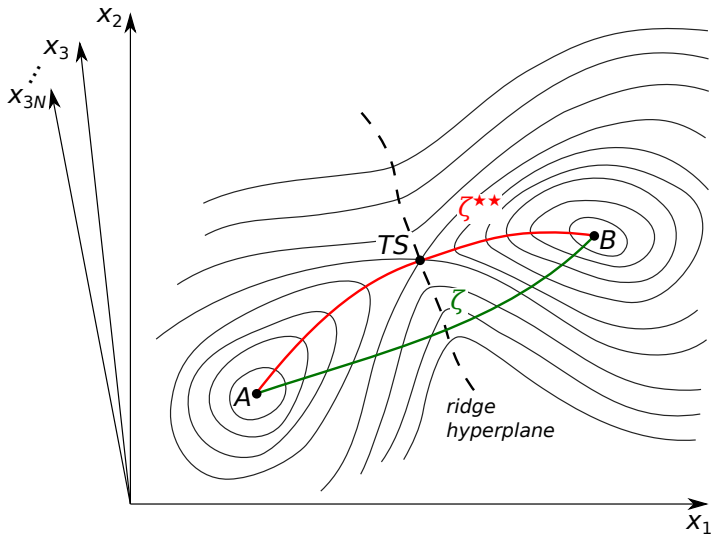

Figure 3.3: Schematic representation of a configurational space of N atoms with two stable compounds A and B and a single transition state on a ridge separating their basins of attraction. Any path ζ has to cross the ridge, and the minimum energy path $\zeta^{\star\star}$ crosses it at the transition state.

activated complex also should have the momentum pointing towards the products, not back to the reactants.

Once the transition state is known, all the terms in equation 3.29 can be calculated quite straightforwardly using standard electronic-structure methods. However, the task of finding the transition state itself is not easy. I discuss some aspects of this problem in the following section.

Search for a transition state

Let us consider a PES with two basins of attraction, each having one strict minimum (I denote them A and B). As was previously defined, a transition state is a point which is located on the ridge dividing the basins of attraction and, within this constraint, has the lowest energy. One can immediately see, that this is a very vague definition, because we have no indicating function to determine whether the point lies in the basin A, or B, or on the boundary between them. Exploiting the special property of a saddle point that it has exactly one imaginary vibrational normal mode does not guarantee finding the true activated complex, because the basins of attraction may contain saddle

points outside the ridge. Therefore, it is nearly impossible to define a search for the transition state *only* – we have to consider the TS in a wider context. We know that every trajectory $\zeta(t) : \mathbb{R} \to \mathbb{R}^{3N}$ which starts at point A and ends at B has to cross the ridge. And each such path has a point with maximal energy, which is the ridge for that particular path, although it doesn't necessarily lie at the true boundary of the basins. Having that in mind, we can reformulate the problem into a search for the *minimal barrier paths*, which can be defined as the paths $\zeta^\star(t)$ which have the lowest intrinsic maximum.

$$\max_t \left(E[\zeta^\star(t)]\right) = \min_\zeta \left(\max_t \left(E[\zeta(t)]\right)\right) \tag{3.30}$$

A stronger version of a minimal barrier path is a *minimal energy* path $\zeta^{\star\star}$ (see fig. 3.3), which satisfies an additional condition

$$E[\zeta^{\star\star}] = \min_{\zeta^\star} \left(\int_0^1 E[\zeta(t)]dt\right). \tag{3.31}$$

Although the requirement 3.31 is not necessary in the context of TST, it helps to ensure that the path doesn't lie in "unreasonable" areas that are unlikely to be visited in equilibrium.

There are various methods of saddle point search, such as eigenvector-following [149, 150], "dimer" method [151] and others. In the next section, I will describe the Nudged Elastic Band method (NEB) which became a de facto standard in the community and which I implemented in the i-PI code and used to calculate the barriers for water splitting reaction.

3.2.2 Nudged elastic band method

NEB is a chain-of-states method of local optimization designed to locate the minimum energy path. It was suggested by G. Henkelman and his colleagues in a series of papers [152, 153, 154]. By definition, a minimal-energy path (MEP) is a variational minimum for the path $\zeta(t)$:

$$\frac{\delta E}{\delta \zeta} = 0, \tag{3.32}$$

which implies that the atomic forces should not have any component perpendicular to the path:

$$\boldsymbol{\nabla} E \cdot \boldsymbol{\tau} = 0, \tag{3.33}$$

where $\boldsymbol{\tau} = d\zeta/dt$ is a tangent vector of the path. In what follows, I will assume $\boldsymbol{\tau}$ to be normalized to unit length, unless the opposite is stated explicitly.

If we discretize the path by a set of points $\boldsymbol{R}_i$ and optimize the path by moving these points, we want to keep the discretization of the path "good", which may mean different properties in different algorithms, but the most obvious criterion is that the points are distributed uniformly along the path. There are two closely related methods: NEB and String, which address the uniformity requirement in different ways. In the NEB method, the replicas $\boldsymbol{R}_i$ move according to two force components: a component of the physical force perpendicular to the path, and an additional spring force, connecting the i-th replica with its neighbors $i \pm 1$. The spring force, in opposition to the physical one, is projected to be parallel to the tangent at the considered point:

$$\boldsymbol{F}_i = \boldsymbol{F}_i^{\mathrm{s}}|_{\parallel} - \boldsymbol{\nabla} E(\boldsymbol{R}_i)|_{\perp}, \tag{3.34}$$

$$\boldsymbol{\nabla} E(\boldsymbol{R}_i)|_{\perp} = \boldsymbol{\nabla} E(\boldsymbol{R}_i) - \boldsymbol{\nabla} E(\boldsymbol{R}_i) \cdot \boldsymbol{\tau_i}, \tag{3.35}$$

$$\boldsymbol{F}_i^{\mathrm{s}}|_{\parallel} = k \left(|\boldsymbol{R}_{i+1} - \boldsymbol{R}_i| - |\boldsymbol{R}_i - \boldsymbol{R}_{i-1}| \right) \boldsymbol{\tau_i}, \tag{3.36}$$

where k is a spring constant, which is an adjustable parameter of the method. Such a projection of forces is shown in the figure 3.4. One can see that the forces become zero if the replicas of the system lie equidistantly on the MEP.

Climbing-Image NEB

One can see that the requirement of equidistance does not guarantee that the highest-energy replica lies on the saddle point. An additional procedure was proposed to bring the highest replica to the transition state. After the MEP is converged by the NEB algorithm, all the replicas except the highest one are frozen, and the physical force on the latter is modified so that the system "climbs" in the NEB tangent direction, while keeping all the orthogonal force components from the physical force:

$$\boldsymbol{F}^{\mathrm{climb}} = -\boldsymbol{\nabla} E + 2 \left(\boldsymbol{\nabla} E \cdot \boldsymbol{\tau} \right) \boldsymbol{\tau} \tag{3.37}$$

Stability and performance of NEB

Being formulated in the late 90s, the NEB method immediately became very popular, and soon it became clear that, despite its apparent simplicity and clear pictorial rep-

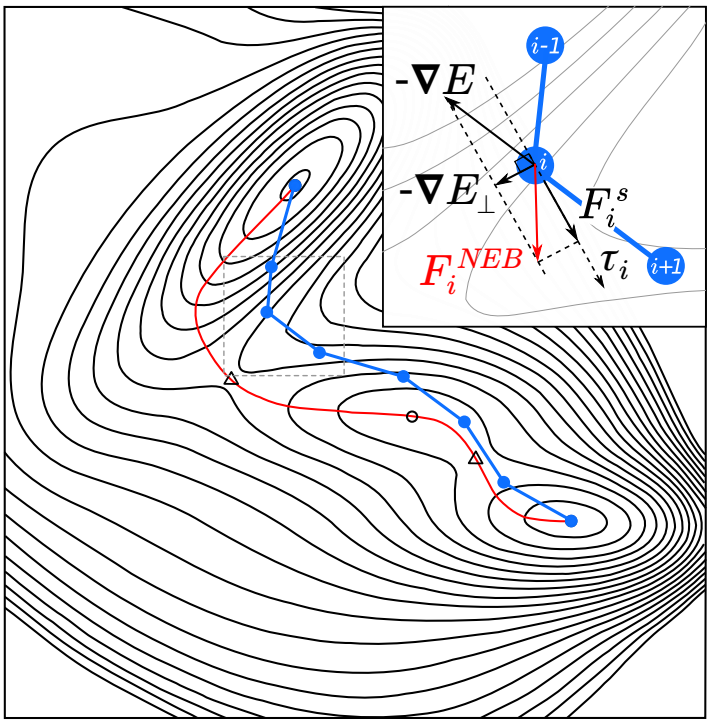

Figure 3.4: The forces acting on an atomic system during the NEB path optimization. The energy landscape is the Müller-Brown surface [6]. F^{s} is the spring force defined in 3.36, and $\boldsymbol{\nabla} E_{\perp}$ is the perpendicular component of the physical force, as defined in 3.35. The red line shows the true MEP, and the blue line with circles represents a hypothetical state of the NEB with 6 moving nodes during the optimization process.

resentation, in practice it often behaves not as one intuitively expects, and has severe issues with stability. It is hard to count all the papers that suggest modifications to the method, and this effort is ongoing. Interestingly, none of the dozens of suggested improvements became a mainstream replacement of the original climbing-image nudged elastic band (CI-NEB), as it was formulated in [153]. To name a few, researchers tried to improve an optimization algorithm [155], or varied the number of NEB nodes during the optimization [156, 157], introduced variable spring constants [153, 158, 159]. An interesting attempt to improve the behavior of the algorithm was done by replacing the piecewise-linear representation of the reaction path with a smooth spline representation, known as the String method [160, 161]. Force projection of the String method is shown schematically in fig. 3.5. The idea of the method is to remove the tangential component of the physical force, make an optimization step, and then to resample the

nodes equidistantly along the new spline-interpolated path.

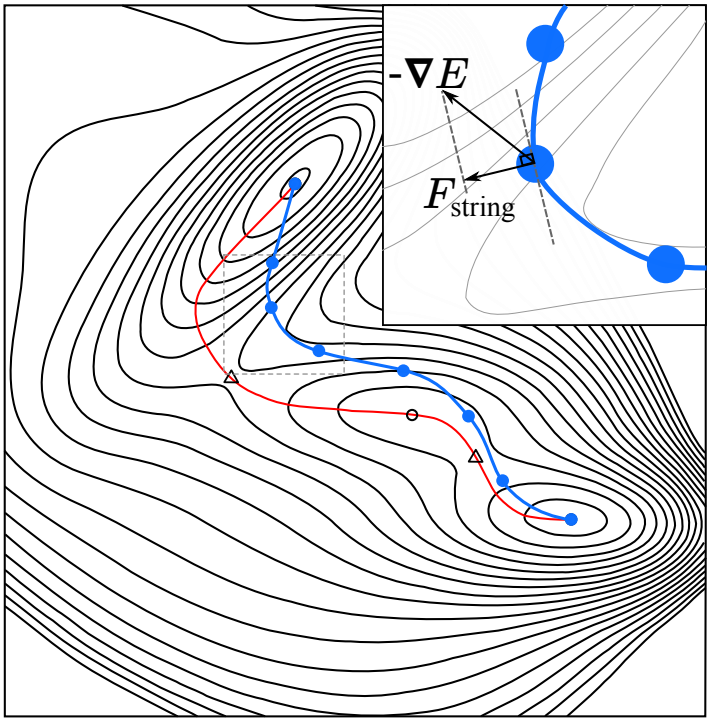

Figure 3.5: The force acting on an atomic system during the String path optimization. The energy landscape is the Müller-Brown surface [6]. F_{string} is the force component perpendicular to the tangent of the spline. The red line shows the true MEP, and the blue line with circles represents a hypothetical state of the String with 6 moving nodes during the optimization process.

A few years after the original paper, its authors reviewed the state of the art [162]. The most important observations, to my view, are the fact that the Hessian of the NEB is not Hermitian [155], and the fact that small differences in the implementation of the optimization algorithms, that are often not reported, can drastically affect the convergence of NEB. In fact, the choice of the upper limit for step size and the choice of a value to put on the main diagonal of the Hessian for the quasi-Newton Broyden–Fletcher–Goldfarb–Shanno (BFGS) algorithm continuously transform the algorithm from a very slow, conservative limit to a highly unstable one. Many people suggest using BFGS-family algorithms with a line search strategy for determining the optimal step length, or the Runge-Kutta method to move the replicas of the NEB or the String method. While it may increase the stability, the price to pay "on the spot"

is the necessity of multiple force evaluations within a single NEB/String step, which may easily override the gain in the number of the NEB steps.

Another observation that is worth mentioning is that the presence of degenerate degrees of freedom $x^{\text{degen.}}$, which have $\partial E/\partial x^{\text{degen.}} = 0$ (e.g. free translations and rotations), in combination with the discrete representation of the path and with the fact that the NEB procedure does not contain any penalty for elongating the path, leads to a completely distorted path, as present in the figure 3.6. In the context of quantum chemistry codes, where people casually use internal molecular coordinates, the problem of translations and rotations does not appear. However, in many popular general-purpose DFT codes the Cartesian representation is used, in which free rotations are not sorted out by default, therefore it becomes a responsibility of a developer of an algorithm. A similar effect was noticed by W. Yang and his coauthors, when the irrelevant DOFs are not completely degenerate, but are much softer than the relevant ones [163]. In such a case, a distorted path is not a stable solution, but irrelevant DOFs affect convergence and they often guide optimization to a very distorted path that never converges. The solution that was proposed by W. Yang and coauthors is rather *ad hoc*, because it relies on user-defined collective variables to define the distance between the NEB nodes.

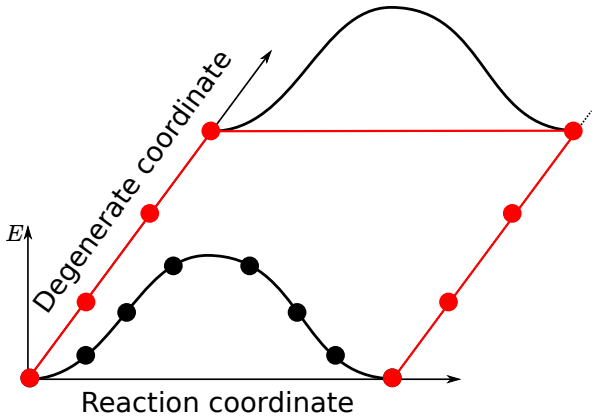

Figure 3.6: Behavior of the NEB path in presence of a degenerate degree of freedom. The black circles show reasonable equidistant MEP, and the red circles show the path that is lower in energy and therefore is preferred by the algorithm.

To summarize, it seems to me that no universal treatment of NEB has been pro-

posed, which would not require increasing the number of force evaluations. However, it is possible to reduce the cost in a different way: instead of trying to decrease the number of force evaluations, one could converge NEB on an approximate PES, which improves iteratively until the NEB path on this approximate PES stops changing with the refining of the approximation [164]. Thus, one can afford doing very small steps when moving the replicas while keeping the number of *ab initio* force evaluations small.

3.2.3 Implementation of NEB in i-PI

There are different ways to use NEB with the FHI-aims code. The first one is the aimsChain package distributed together with the FHI-aims code [36]. While being proven to be robust, it lacks several important features. To the present day, aimsChain is not up-to-date with the augmentations of the FHI-aims geometry file format, such as a specification of the vacuum level coordinate in periodic slab calculations and a specification of a homogeneous electric field, which both are necessary for the calculations described in the Chapter 5. The second problem, which is more difficult to fix, is that aimsChain does not offer parallel calculation of forces at different nodes of a path. This drawback makes calculations considerably longer. Considering these obstacles and also the possibility of using other *ab initio* codes, we chose to implement NEB in the i-PI code [76].

General architecture

A diagram of the implementation is given in the figure 3.7. I-PI provides the `Beads` class which handles multiple replicas of the same physical system. It performs energy and force calculations and ensures that their values are consistent with the geometry – if forces are requested somewhere in the code and geometry changed since the last calculation, the code enforces recalculation. However, it is implemented so that consistency is checked across the whole $3N \times P$ (P beads with N atoms) space simultaneously, which means that moving even one bead causes recalculation of the whole path. Changing the number of beads during the simulation is not designed in the i-PI workflow. To circumvent this, we created an additional `Beads` objects: of size $(P-2)$ to avoid recalculation of the fixed endpoints of the path, and of size 1, when climbing

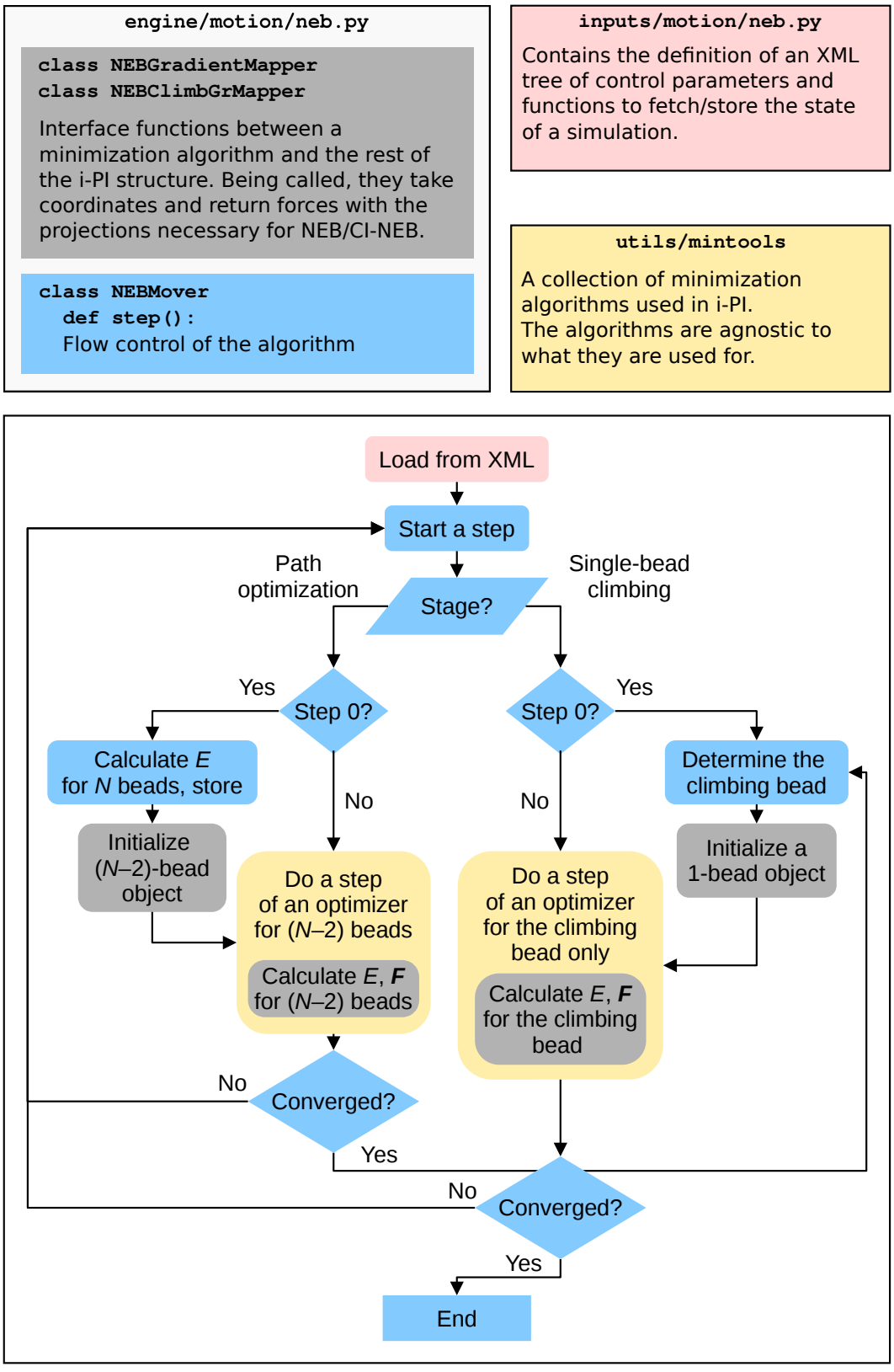

Figure 3.7: A diagram of the NEB implementation in the i-PI code. The colors in the flowchart show which part of the code is responsible for that particular part of the flow.

of a single bead is performed.

For the sake of unification with other optimization modules in i-PI, we implement a 4-component scheme (input class, flow controller, mapper, optimizer) in our NEB implementation. The idea of this scheme is the following: i-PI provides a collection of generic optimization algorithms, which are agnostic to the physical system at which they are called. They operate in abstract n-dimensional space and minimize the gradient of a given "mapper" function (some algorithms explicitly minimize the value of the function as well), while the flow control class, which is a descendant of `Motion` class, takes care of interpreting the inputs (parsed from an XML file by input class), checking convergence criteria and performing other necessary technicalities. Depending on inputs, the flow controller calls a particular optimizer to make a step and passes a particular mapper function to it. In case of NEB, the controller is the `NebMover(Motion)` class stored in `ipi/engine/motion/neb.py`. The mapper classes are `NEBGradientMapper` and `NEBClimbGrMapper`, dealing with $(P-2)$-bead object for optimization of the path with fixed endpoints and with a single-bead object to perform climbing-image optimization.

One drawback of the chosen architecture with task-agnostic optimizers (see fig. 3.7) became apparent during the implementation of the String method. The structure of dependencies in the i-PI code requires that the forces at the end of each step are consistent with the atomic positions, i.e. if atoms are moved after the forces are calculated, the forces have to be recalculated at the end of the step, otherwise the outputs of i-PI will be inconsistent. This requirement serves good service for MD algorithms, which are vastly present in i-PI, but causes complications in certain optimization algorithms. Thus, in order to perform a 2-step movement of the string (an optimization step and resampling of the spline), one has to incorporate resampling inside the optimization algorithm, so that an optimizer evaluates the quality of a step only after the spline is resampled – otherwise the forces are calculated twice per step, which is an unnecessary waste of resources. It is impossible to achieve with the existing optimizers from the `utils/mintools.py` collection. I implemented the String algorithm with two force evaluations per step in i-PI following the same architecture as was used for NEB, and further effort would be needed to achieve a scheme with a single force call. For the

implementation I did and the test systems I tried, the String method did not reduce significantly the number of steps to achieve convergence compared to NEB. Within this work, I did not pursue the String method further.

Optimization algorithms

I-PI provides a collection of the optimization algorithms in `mintools.py`, including several flavors of the efficient BFGS. However, their implementation relies on energy to determine the step size – either via the trust-radius method or via the line-search procedure. For NEB, only implementations which rely on forces solely are applicable, because the projections prescribed by the NEB scheme lead to non-conservative forces, and the energy is not consistent with them, even if we formally account for the spring energy terms [162]. Using such energy in algorithms like trust-radius BFGS may cause instabilities. Therefore, we have implemented a version of the BFGS algorithm which includes damping of the BFGS update as described in Procedure 18.2 in the well-known textbook of Nocedal and Wright [165]. BFGS provides the best performance when it works, but it fails in some tasks. More generally, it is known that Hessian-based methods may fail in cases when a system has non-Hermitian Hessian, which is true for NEB. We stabilize BFGS by incrementally adding small values to the main diagonal of its approximate Hessian in case its spectrum contains negative eigenvalues. We also implemented the gradient-based "fast inertial relaxation engine" (FIRE) [166] to handle cases when BFGS fails. In order to stabilize both algorithms further, the "quality" of each step is assessed by comparing the direction of the step with the direction of the NEB force. If the cosine of the angle between them is less than 0.5, the maximal allowed step length is halved, and if it's more than 0.6 (0.8), the maximal step is increased by a factor 1.1 (1.3). We thus try to achieve an algorithm which is assertive in areas of good behavior, which typically take place at the beginning of the optimization, but quickly becomes conservative if problems occur.

Interpolation of the path

An initial path for NEB/String optimization can be created from an arbitrary number of known points, which should necessarily include the endpoints, and expected inter-

mediate states can be included optionally. These initial points then can be interpolated either piecewise-linearly or with a cubic spline, and the resulting path is then sampled equidistantly with a requested number of beads. Such a design allows reusing the pre-calculated paths if the endpoints are slightly changed, which happens, for example, if one simulates the same chemical reaction on a surface with a different electric field applied. The script to perform interpolation is provided with the i-PI package and can be found in `tools/py/neb_interpolate.py`.

Other considerations

- From my experience I conclude that the geometry of a system has a major impact on the stability of a NEB relaxation. Whenever it is possible to run the same system with much cheaper calculation settings, being it a forcefield or much cheaper electronic structure calculation (e.g. I used only one or two layers of surface for testing), it is recommended to try it first. If the algorithm is stable for the cheap system, it highly likely will remain stable on the actual task, and, in addition, the converged geometry from the cheap calculation will be a reasonable initial guess for the more expensive calculation. This also helps when very conservative settings are required: starting from a linearly interpolated path and doing small steps takes a very long time.

- Another observation from converging problematic cases is that NEB is sensitive to the stiffness of its "springs", as was noted by others [158]. For dissociation of a single water molecule with 9 intermediate beads, quite stiff springs with $k \approx 40$ eV/Å showed the best convergence. It is higher than commonly suggested values of 0.5 to 5 eV/Å.

- When allocating computational resources, it is beneficial to align the number of moving beads with the number of i-PI "clients", i.e. instances of a code that calculates energies and forces. If the number of clients is the same as the number of beads, i-PI assigns the next task for a certain bead to the same client which calculated the previous step for this bead. In case of DFT, it gives a substantial gain in the number of SCF iterations. It also implies that path optimization and climbing stages need different computational setups to be efficient. To give an

idea, I used 9 single-node DFT calculations to optimize the NEB path with 9 intermediate beads, and then a single calculation on 4 nodes for the climbing-image optimization.

Chapter 4

Quantum nuclei at weakly bonded interface: cyclohexane on Rh(111)

This chapter summarizes our research of cyclohexane C_6H_{12} and its fully deuterated counterpart C_6D_{12} adsorbed on the Rh(111) surface. The properties of both molecules were studied by means of electronic-structure calculations using quasi-harmonic approximation (QHA), as well as *ab initio* path integral molecular dynamics (AI-PIMD). We studied the isotope effects in work function, adsorption energy and geometry of the adsorbate at thermal equilibrium at temperatures close to those used in experiments.

The results reported in this Chapter were published in collaboration with Dr. Ikutaro Hamada and my supervisor Dr. Mariana Rossi [7] under the open CC-BY-NC license[1]. Only the work that I did myself for that paper is included in this Chapter. The text and the figures from this publication and its supplementary materials were used in this chapter, therefore some fragments of the text repeat literally.

4.1 Isotope effects in cyclohexane-Rh(111) interface

In most cases, the electronic properties of interfaces do not depend strongly on the isotopic constitution of the atoms that compose them. The reason is that the electronic structure of different isotopes is the same, and nuclei can typically be considered

[1] `https://creativecommons.org/licenses/by-nc/4.0/`

classical particles, which move on the PES defined by that electronic structure and follow the statistical distribution which is mass-independent. These identical distributions, in return, produce the same distribution for the electronic subsystem. However, when nuclei express more "quantumness", especially moving towards the beginning of the periodic table and towards lower temperatures, this picture becomes less and less accurate. The measure for that is the ratio between the "classical" thermal energy $k_{\mathrm{B}}T$, which doesn't depend on mass, and the quantum zero point energy $\hbar\omega/2$, which is indeed mass-dependent *via* the frequency of vibration ω. In such cases, an isotopic change may lead to structural changes in the material and thus to a considerable change in the electronic structure. Such electron-phonon coupling effects can be captured to a great extent in the adiabatic limit [167].

One known case to exhibit such isotopic effects is cyclohexane (C_6H_{12}) adsorbed on platinum-group metal surfaces. In a series of papers by Koitaya, Yoshinobu and coworkers [8, 168], it was shown that C_6H_{12} and its fully deuterated counterpart C_6D_{12} impose different amounts of work function change when adsorbed on the Rh(111) surface. Based on work function measurements by the ultraviolet photoemission spectroscopy (UPS) and previous calculation of alkanes on metal surfaces [169], the authors suggested that deuterated molecules should lie farther away from the surface. Another affected property is the desorption energy: C_6H_{12} at lower coverages binds to Rh(111) surface 84 ± 23 meV stronger than C_6D_{12}, thus exhibiting an inverse kinetic isotope effect. The availability of experimental data and the importance of cyclohexane in a number of chemical processes, including reversible dehydrogenation to benzene with the release of hydrogen, make cyclohexane a suitable target to study the performance of different theoretical techniques in a realistically complex, but yet well-defined environment.

Theoretical investigation of the aforementioned isotope effects is rather challenging because one has to capture changes in the electronic structure of the high-dimensional system as well as the behavior of quantum nuclei. At least an approximate description of electron-phonon coupling is needed to relate nuclear fluctuations and electronic-structure variations. As researchers turn towards soft and hybrid electronic materials, where electron-phonon coupling tends to be more pronounced [13, 170], modelling of

these effects becomes more important. A common way to address such problems is to employ the harmonic approximation (HA) for the nuclear vibrations on first-principles potential energy surfaces [171]. However, weakly bonded interfaces are known to be anharmonic, for instance, molecules demonstrate mobility on a surface well beyond harmonic oscillations, which raises a question of applicability of the HA.

On the other hand, there is the *ab initio* path integral molecular dynamics (AI-PIMD) method capable of including nuclear quantum effects (NQE) fully anharmonically [72]. It is a truly powerful method, however, the high computational cost of AI-PIMD limits its applications severely. Therefore, in this work AI-PIMD simulations are performed making use of the SL-RPC technique which reduces the amount of ring-polymer "beads" required for simulations of weakly-bonded interfaces [143]. AI-PIMD results are compared to harmonic approximation for the adsorption energy and to the quasi-harmonic approximation, which we will explain below, for the structural properties and the work function change. With these simulations, we are able to explain the physical mechanism of the observed isotope effects on the cyclohexane/Rh(111) interface and assess when a quasi-harmonic analysis of these effects is valid. The AI-PIMD approach has been successfully applied previously to reveal the impact of nuclear quantum fluctuations on the electronic structure of diverse systems [172, 173, 174]. We follow this approach for cyclohexane/Rh(111) and discuss its capabilities and limitations.

It is known from the experiments that certain properties of the cyclohexane/Rh(111) interface depend on the coverage [8]. In particular, at coverage values below 0.5 desorption of cyclohexane competes with its dehydrogenation. To have access to coverage-dependent properties, we built a few systems with different adsorption patterns, taking hints from low energy electron diffraction (LEED) and scanning tunneling microscopy (STM) data. On a clean Rh(111) surface, experiment shows a high-order commensurate $(2\sqrt{79} \times 2\sqrt{79})R17.0^\circ$ pattern [30]. Such a large structure is way beyond the capabilities of *ab initio* calculations, given that at least a few atomic layers of metal are needed. A few smaller structures proposed by experimentalists and suitable for DFT simulations are $(\sqrt{7} \times \sqrt{7})R19.1^\circ$ with a single molecule in the unit cell, $(\sqrt{19} \times \sqrt{19})R23.4^\circ$ with 3 molecules, (5×5) cell with 4 molecules and the $(2\sqrt{3} \times 2\sqrt{3})R13.9^\circ$ pattern

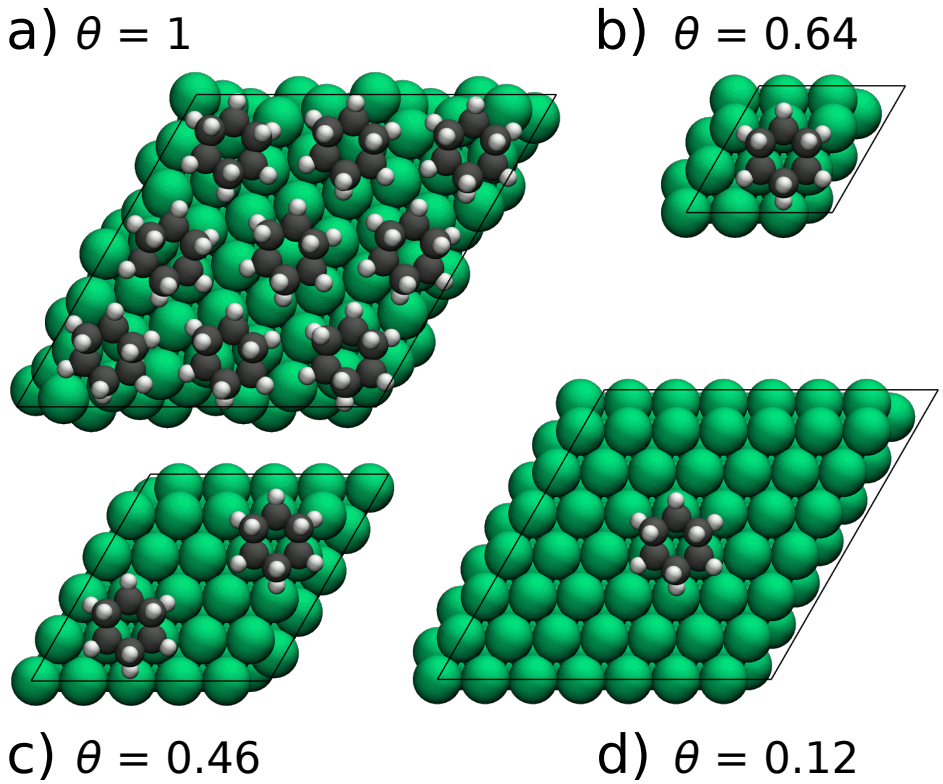

Figure 4.1: The cyclohexane adsorption patterns considered in this work for modelling different coverages θ. a) $\theta = 1$, $(2\sqrt{3} \times 2\sqrt{3})R13.9°$ unit cell (0.173 molecules per Rh atom). b) $\theta = 0.64$, (3×3) unit cell. c) $\theta = 0.46$, (5×5) unit cell. d) Coverage $\theta = 0.12$, (7×7) unit cell. The figure is reproduced from [7].

with 9 molecules in the unit cell [30, 175]. Although the $(\sqrt{7} \times \sqrt{7})R19.1°$ structure is the smallest one and the most convenient one from the perspective of a computational cost, we didn't want to restrict ourselves to the system with a single adsorbed molecule, because all the periodic images of that molecule would move in a coordinated fashion in a simulation, likely producing artifacts in spectra and in statistical distributions. The $(2\sqrt{3} \times 2\sqrt{3})R13.9°$ structure, which is shown in Figure 4.1a, has, in contrast, 9 molecules occupying different adsorption, and it is the reachest structure from the aforementioned ones to exhibit intermolecular interactions. We therefore took this structure as a reference for the full-coverage monolayer structure. The effective coverage values for other structures were derived from this one. Smaller unit cells which we used in this work are shown in figures 4.1b-d. In the following, we perform our calculations on the structure presented in figure 4.1c ($\theta = 0.46$) unless explicitly stated otherwise. This unit cell contains two cyclohexane molecules adsorbed on a Rh(111) (5×5) slab. It allows us to capture sufficiently the phonon band structure dispersion of the metal substrate in the real-space dynamics simulations, which is known to be modified by an adsorbate [176].

4.2 Details of simulations

Electronic structure calculations with FHI-aims

Energies and forces are calculated using density-functional theory DFT) with the PBE XC functional [86] and the range-separated hybrid HSE06 functional [31]. The calculations were done with the all-electron FHI-aims code, which uses numerical atom-centered orbitals [36] as basis sets. The FHI-aims package contains predetermined settings for numerical parameters and basis sets, which are aimed at different accuracy levels. *Light* settings were used for PIMD and phonon calculations, and *tight* settings were used for potential energy curves and electron density rearrangement. The parameters of Rh for the pairwise Tkatchenko-Scheffler van der Waals correction, modified in order to capture the collective response of a surface in the Lifshitz-Zaremba-Kohn form [10] (vdW^{surf}), were taken from Ref. [110]. The van der Waals interaction between Rh atoms was not included. Further, we used $\beta = 0.81$ for the non-local many-body

dispersion (nl-MBD) correction with the PBE functional and $\beta = 0.83$ for the same correction with the HSE06 functional.

We considered 4 Rh(111) layers in all FHI-aims calculations. The 2 bottom layers of the slab are fixed in the bulk geometry. The bulk geometry was calculated for the single-atom FCC unit cell using a 16x16x16 k-point grid. The k-point grid for the different surface unit cells was scaled accordingly. For the 5×5 Rh(111) surface unit cell, a $2 \times 2 \times 1$ k-point grid was employed. The resulting lattice constant of 3.83 Å is in good agreement with the experimental value of 3.80 Å [177]. The surface was aligned perpendicular to the z axis. In order to isolate the system from its periodic replicas in the z direction, a dipole correction [1] and a vacuum layer of 30 Å in both directions were applied.

Vibrational analysis was performed by a modified version of the Phonopy code coupled to FHI-aims [178, 179], which allowed to build the Hessian only for the molecular adsorbate and to account for a surface as a rigid environment. This approximation is well justified because the coupling between Rh atoms and the molecules is weak, and this weak coupling is concentrated in the low-frequency modes of the adsorbates, which behave very similarly for H- and D-cyclohexane and thus do not impact isotope effects. We set atomic displacements to 0.01 Å for finite difference calculations and considered geometries relaxed with a maximum force threshold of 0.001 eV/Å.

Adsorption energies and free energies

The adsorption energies per molecule were calculated with

$$E_{\mathrm{ads}}^{\mathrm{pot}} = (E_{\mathrm{s+m}}^{\mathrm{pot}} - E_{\mathrm{s}}^{\mathrm{pot}})/N_{\mathrm{mol}} - E_{\mathrm{m}}^{\mathrm{pot}}, \tag{4.1}$$

where $E_{\mathrm{s+m}}^{\mathrm{pot}}$ is the total energy at the potential energy surface of a slab with molecules adsorbed, $E_{\mathrm{s}}^{\mathrm{pot}}$ is the total energy of a clean surface relaxed with 2 bottom layers fixed in bulk position, $E_{\mathrm{m}}^{\mathrm{pot}}$ is the total energy of a molecule relaxed in vacuum, and N_{mol} is the number of molecules in a unit cell. A similar expression can be written for a free energy of adsorption $F_{\mathrm{ads}}^{\mathrm{harm}}$.

The harmonic vibrational free energy was calculated as

$$F^{\text{harm}} = \sum_{i=1}^{N_{\text{modes}}} \left[\frac{\hbar\omega_i}{2} + k_B T \ln\left(1 - \exp^{-\frac{\hbar\omega_i}{k_B T}}\right)\right] + \\ +_{\text{[if gas phase]}} \left(F^{\text{trans}} + F^{\text{rot}}\right), \tag{4.2}$$

where $N_{\text{modes}} = 3N - 3$ when the free energy of a clean surface is calculated (N is the number of atoms in a unit cell), $N_{\text{modes}} = 3N - 3N_{\text{s}}$ (N_s is the number of surface atoms in a unit cell) when the free energy of molecules adsorbed on surface is calculated, and $3N_m - 6$ (N_m is the number of atoms in a molecule) when the free energy of an isolated molecule is calculated. Rotational and translational contributions were added for the free molecule according to the rigid-body and ideal-gas textbook expressions [101]:

$$F^{\text{rot}} = -k_B T \left(3/2 \ln(T) + \ln\left[\frac{8\pi I_1 I_2 I_3}{\hbar^3}\right]\right) \tag{4.3}$$

$$F^{\text{trans}} = -k_B T \ln\left[\frac{e k_B T}{P}\left(\frac{mT}{2\pi\hbar}\right)^{3/2}\right] \tag{4.4}$$

Expression 4.2 only takes into account vibrations at the Γ point of the unit cell. Since we focus mostly on molecular vibrations, which show a very small phonon band dispersion, and employ large unit cells, this approximation does not introduce large errors in the calculated free energy differences. For the translational term, we took the pressure of 10^{-8} Pa, which is close to the reported experimental conditions [8].

The quasi-harmonic ZPE-corrected energy of adsorption E^*_{ads} was calculated as a difference between the energy at the equilibrium distance and at 10 Å away from the surface, which is considered to be far enough to remove all molecule-surface interaction,

$$E^*_{\text{ads}}(h_{\text{COM}}) = \left(E^{\text{pot}}_{\text{s+m}}(h_{\text{COM}}) + \sum_{i=1}^{3N_m-3} \frac{\hbar\omega_i}{2}(h_{\text{COM}})\right) - \\ - \left(E^{\text{pot}}_{\text{s+m}} + \sum_{i=1}^{3N_m-3} \frac{\hbar\omega_i}{2}\right)\Bigg|_{h_{\text{COM}}=10\text{Å}}, \tag{4.5}$$

where h_{COM} is the distance from the center of mass of the adsorbate to the Rh surface. Although E^*_{ads} is not the true adsorption energy, this procedure compensates for spurious interactions that might appear in a particular simulation cell. A numerical comparison of the energies calculated by the expressions 4.1 and 4.5 is given in the section B.2 of the Appendix. For the ZPE contribution, we include $(3N_m - 3)$ molecular vibrations.

Ab initio molecular dynamics

Ab initio molecular dynamics (AIMD) and AI-PIMD simulations were carried out by connecting FHI-aims to the i-PI code [76]. For classical-nuclei MD, a timestep of 1 fs was used. For PIMD simulations, a smaller timestep of 0.5 fs was employed.

In order to accelerate sampling in the NVT ensemble, we applied a colored-noise GLE thermostat [131, 132] to the classical-nuclei *ab initio* molecular dynamics (AIMD) simulations. For the AI-PIMD simulations, the PIGLET thermostat was used [140]. This approach preserves quantum distribution and gives a fast convergence of observables with respect to the number of replicas. The parameters for the thermostats are: 8 fictitious degrees of freedom s [132], and a frequency range of 0.32-3200 cm^{-1} for C_6H_{12} and 0.23-2300 cm^{-1} for C_6D_{12}. The **A** and **C** matrices (as defined in [132]) are parameterized for $\hbar\omega/k_BT = 50$ using the GLE4MD library [180]. We observed convergence with around 12 beads for the adsorbate atoms (H) at 150 K within this setup. After thermalization, we have calculated 7 independent trajectories of a total length of 32 ps for C_6H_{12}, 5 trajectories of a total length of 30 ps for C_6D_{12}, and 5 trajectories of a total length of 97 ps for classical-nuclei cyclohexane. Each force evaluation for the model $\theta = 0.46$ (FHI-aims program, *light* settings) amounts, on average, to 3.1 minutes when parallelized over 240 cores (Intel Xeon Gold 6148 Skylake processors, MPCDF COBRA supercomputer). This gives an idea of how expensive these simulations are even without considering nuclear quantum effects.

The effects of nuclear fluctuations on electronic observables (work function, electronic density of states, etc.) were calculated as the average of single-point calculations from AI-PIMD trajectories through the following general expression

$$\begin{aligned} \langle A \rangle =& \frac{1}{Z} \mathrm{Tr}\left[\hat{A} e^{\frac{-\hat{H}}{k_B T}}\right] \xrightarrow[\text{PIMD sampling}]{\text{ergodicity,}} \\ & \Rightarrow \frac{1}{P N_s} \sum_{i}^{N_t} \sum_{k}^{P} A\left(\boldsymbol{R}_{(k)}(t_i)\right), \end{aligned} \tag{4.6}$$

where $\hat{A}$ is a position-dependent observable, $\hat{H}$ is the Hamiltonian, Z is the partition function, P is the number of beads of a ring polymer, N_t is the number of snapshots considered from a PIMD trajectory, and $\boldsymbol{R}_{(k)}$ is a position vector for a bead k. The snapshots from the PIMD trajectory were picked so that they were statistically independent. The criterion for independence is an autocorrelation time of the property A.

In our PIMD calculations, the autocorrelation time is 30 fs for a velocity, 300 fs for a work function and 600 fs for the z-coordinate of the center of mass of a molecule. We also used these correlation times to calculate error bars. For classical nuclei simulations, the same expression was used with $P = 1$.

In order to reduce the cost of AI-PIMD simulations, we use the fact that the bonding between molecules and a surface is relatively weak in the case of cyclohexane and apply the SL-RPC [143], described in Section 3.1.2.

The error of the SL-RPC for a cyclohexane on Rh(111) with $P' = 1$ does not exceed **37** meV per molecule for the total potential energy and **79** meV/molecule for the total free energy. When comparing H- and D-cyclohexane, one can rely on error cancellation. Then, the error in potential energy *difference* is **19** meV/molecule, and in free energy difference about **36** meV/molecule. It is thus clear that although this approximation is very useful, if quantitative results for this particular system are desired, a contraction to the centroid ($P' = 1$) is not sufficient and we do not further pursue calculations of free energies at this level of approximation. It should, however, be sufficient to capture further important anharmonic effects if present.

4.3 Static results and the quasi-harmonic approximation

4.3.1 Adsorption energy

We calculated the adsorption energy $E_{\text{ads}}^{\text{pot}}$ per molecule for each structure shown in fig. 4.1 as explained in sec. 4.2. The results obtained with PBE+vdW$^{\text{surf}}$ [64, 10] functional are given in column 2 of table 4.1, and the comparison between *Light* and *Tight* computational settings is reported in table B.1 in the Appendix.

The harmonic free energy of adsorption at a temperature of 150 K was calculated by eq. 4.2 and analogously to eq. 4.1. The temperature of 150 K was chosen to satisfy several conditions. On one hand, it is desirable to avoid very low temperatures: they increase the number of ring-polymer beads needed to converge PIMD simulation considerably, and they would reduce the role of anharmonicity, which we aim to in-

Table 4.1: Adsorption energies and harmonic free energies for different coverage values, calculated with the PBE+vdW$^{\text{surf}}$ functional (*light* settings) according to eq. 4.1. The free energy is calculated for the temperature of 150 K and all energies are given in meV. Experimental data from temperature-programmed desorption (TPD) experiments from Ref. [8].

coverage θ	$E_{\text{ads}}^{\text{pot}}$	$E_{\text{ads}}^{\text{pot}}$+ZPE		Δ ZPE	$F_{\text{ads}}^{\text{harm}}$		ΔF
		H	D	H – D	H	D	H – D
0.12	945	1039	1004	35	742	705	37
0.46	953	1056	1022	34	786	750	36
0.64	946	1046	1013	33	780	745	35
1.0	1023	1066	1049	17	790	770	20
0.3 (TPD [8])		728 ± 12	644 ± 20	84 ± 23			

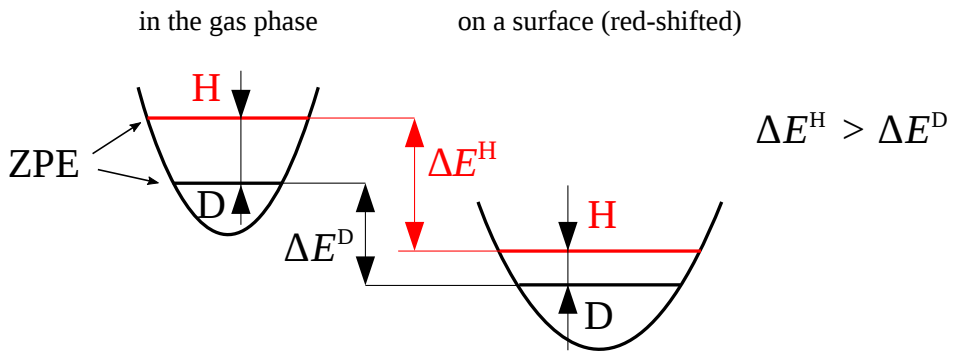

Figure 4.2: The effect of the red shift in the C-H stretching modes on the adsorption energy, shown schematically. The difference in ZPE is between H and D is higher in a vacuum than on the surface, due to the different masses and the red-shift of the corresponding stretching mode upon binding. The figure is reproduced from [7].

vestigate. On the other hand, the temperature should stay below the temperatures of desorption and dehydrogenation, which are both known to be around 200 K [8].

The results for each coverage are summarized in table 4.1, columns 3-8. We note that already in harmonic approximation, different values of ZPE lead to different adsorption energies for C_6H_{12} and C_6D_{12}. It is not an unexpected result. We show in figure 4.2 a pictorial explanation of the phenomenon: the vibrational modes associated with the C-H bonds of cyclohexane pointing towards the surface are red-shifted by up to 300 cm^{-1} in comparison to the gas phase, as shown in figure 4.3. Because of the difference in mass between H and D atoms, such a red shift has a stronger impact on the ZPE of a C-H vibration, compared to a C-D one. In both cases, the effect of ZPE increases the energy of adsorption (table 4.1, columns 3,4), and in the case of C_6H_{12} this effect is stronger. When the translational and rotational entropic contributions of the gas-phase molecules are added, resulting adsorption free energy decreases compared to ZPE-corrected $E_{\mathrm{ads}}^{\mathrm{pot}}$ (table 4.1, columns 6,7). However, these two terms do not give pronounced isotope effects, despite the fact that they are formally mass-dependent. The main reason is that for rigid-molecule motion mass or moment of inertia of the whole molecule is the decisive value, and 84 (C_6H_{12}) vs 96 (C_6D_{12}) a.m.u. is not a large difference. The calculated isotope effect is approximately twice weaker than the reported value obtained in the temperature-programmed desorption (TPD) experiment [8]. We also observe that the difference between H/D adsorption energies decreases at full coverage. It goes down from 37 meV for $\theta = 0.12$ to 20 meV for $\theta = 1$, while the values for coverage 0.12, 0.46 and 0.64 differ negligibly. We explain it by analyzing the vibrational spectra at different coverage. We show in figure 4.3 the harmonic vibrational density of states (vDOS) for the adsorption patterns considered in this work. The key feature is a red shift in the stretching vibrations of the CH groups pointing to the surface (denoted as (I) in figure 4.3b). This red shift slowly decreases with increasing coverage. It means that surface-molecule interaction becomes weaker and, consequently, the C-H bond strengthens. At the highest coverage ($\theta = 1$), the picture is qualitatively different: there are multiple splittings of CH stretching frequencies, because cyclohexane, when packed closely, occupies the adsorption sites which are nonequivalent, unlike more free patterns, which all follow the sketch 4.3a with 3 CH groups pinned to 3 adjacent Rh

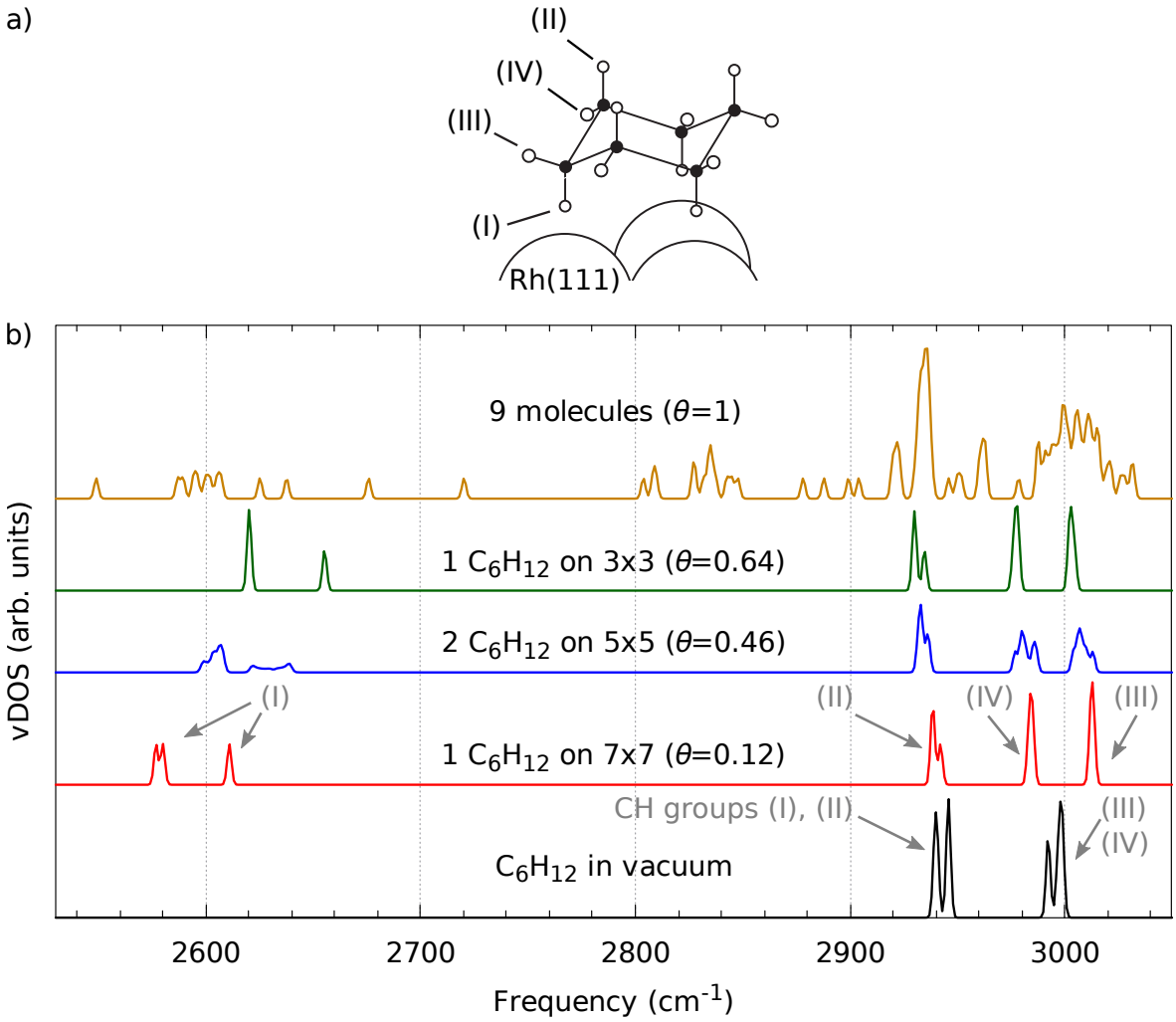

Figure 4.3: a) Different CH groups for a cyclohexane molecule adsorbed on a surface. b) The vibrational spectra of CH stretching modes of cyclohexane in vacuum (black) and on a Rh(111) surface with coverage $\theta = 0.12$ (red), $\theta = 0.46$ (blue), $\theta = 0.64$ (green) and $\theta = 1$ (ochre). The grey arrows assign peaks to the CH groups given in (b). As the red shift in CH stretching modes decreases, the H/D difference in the adsorption energy decreases also. At the full coverage ($\theta = 1$), the intermolecular interaction is so strong that single adsorption sites become highly non-equivalent, which is reflected in multiple peak splitting in the range between 2540 and 3040 cm^{-1}. The figure is reproduced from the SI of [7] with minor changes.

atoms. We also note a blue shift in stretching vibrations of CH groups of type (III) and a slight red shift in groups (II) and (IV).

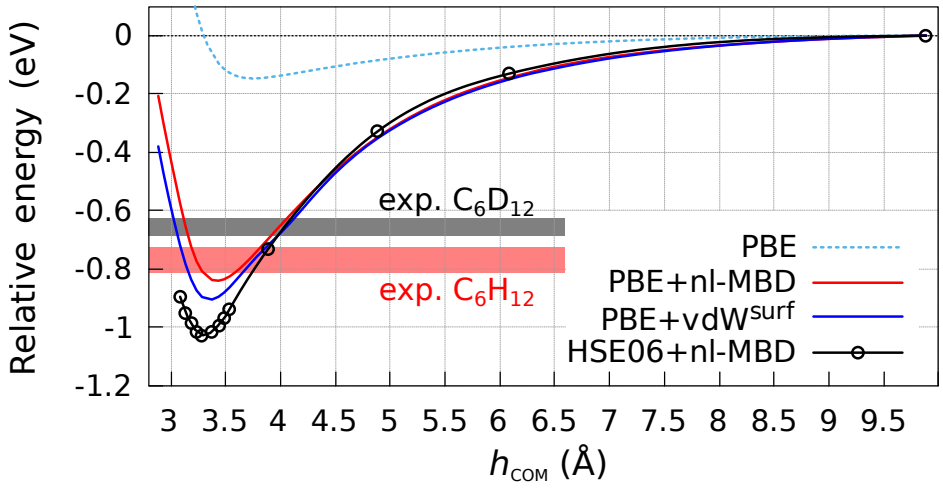

Figure 4.4: Adsorption curves calculated with different exchange-correlation functionals and vdW corrections: PBE (dotted blue line), PBE +vdW^{surf} (solid blue line), PBE+nl-MBD (solid red line), HSE06+nl-MBD (black points).Calculations were performed with the unit cell of $\theta = 0.46$. Shaded areas show the interval of reported experimental values of the adsorption energy of C_6H_{12} (red) and C_6D_{12} (grey) around the coverages we study [8]. The figure is reproduced from the publication [7] with changes.

4.3.2 The role of the exchange-correlation functional

One of the important questions is how the results depend on the choice of XC functional. To elucidate this, we have calculated the adsorption curves of cyclohexane with different functionals and vdW corrections. We took the simulation cell corresponding to $\theta = 0.46$ and moved one of the two cyclohexane molecules along the z direction. At each distance, geometry optimization was performed with the center of mass of the molecule being constrained, while the two topmost layers of the Rh surface and the other molecule were allowed to relax. Instead, we used the geometries optimized with the PBE+vdW^{surf} functional. In figure 4.4, we show the adsorption profile with the pure PBE functional, the PBE+vdW^{surf} functional, the PBE functional with the recently proposed many-body dispersion method nl-MBD [67] and the range-separated

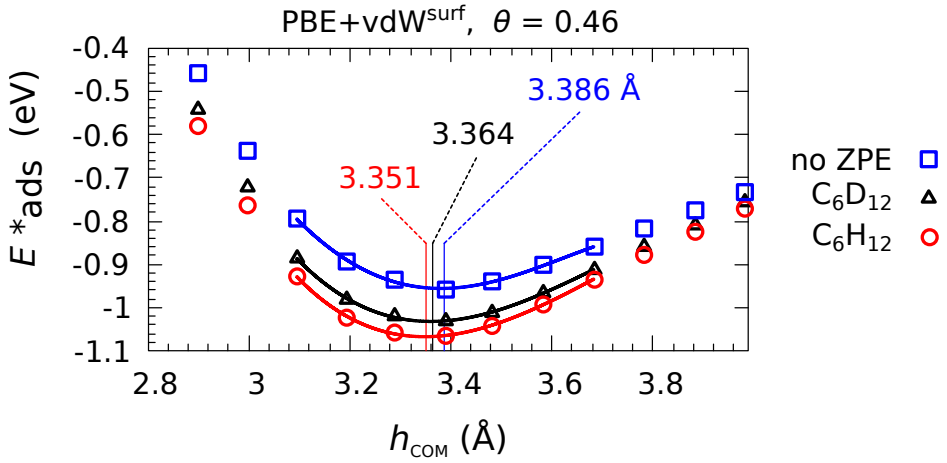

Figure 4.5: ZPE-corrected energy of adsorption for C_6H_{12} (red) and C_6D_{12} (black), calculated according to eq. 4.5 with PBE + vdW^{surf}. The blue line shows the adsorption energy values calculated without ZPE correction. The figure is reproduced from the publication [7].

hybrid functional HSE06 [31] combined with nl-MBD dispersion interactions. To the moment of conducting these calculations, the implementation of the nl-MBD model in FHI-aims did not include calculation of forces, therefore we didn't perform geometry optimization for the models with nl-MBD. The minima of these curves are tabulated in table B.2 in the Appendix.

We first analyze the dataset based on the PBE functional, which gives us information about the role of different models of dispersion interactions. Comparing the depth of the adsorption curve obtained with the bare PBE functional and the others, we conclude, as expected, that vdW interactions are the main component of the molecule-surface binding. Without a vdW correction, the adsorption energy is only 147 meV, which would mean desorption roughly at 30 K[2]. We proceed to compare the results obtained with PBE+vdW^{surf} with the results obtained with PBE+nl-MBD. Both of these vdW corrections do not enter the Kohn-Sham potential within the self-consistent procedure and therefore cannot change the electronic density. We observe that vdW^{surf} predicts a larger binding energy (0.90 eV) and an equilibrium distance closer to the surface (3.36 Å) than nl-MBD (0.84 eV and 3.45 Å, respectively). Considering that

[2]calculated for the UHV pressure of 10^{-8} Pa

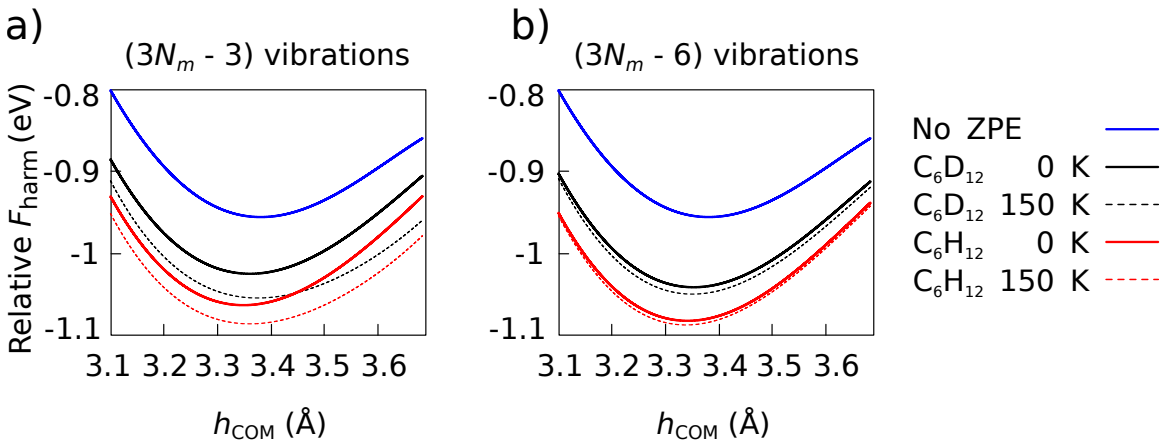

Figure 4.6: The effect of temperature on the harmonic free energy of cyclohexane (red) and D-cyclohexane (black) with and without the inclusion of hindered rigid rotation modes (a and b, respectively). Solid lines show ZPE-corrected potential energy, and dashed lines add finite temperature corrections at the temperature of 150 K. The curves are aligned to zero at the distance of 10 Å. Calculations are done with PBE + vdW^{surf} functional.

nl-MBD contains explicit many-body vdW effects and captures the electronic screening of these interactions better than vdW^{surf} [67], we can conclude that the observed differences are due to both of these effects. Then, we can compare the results obtained with the PBE+nl-MBD and the HSE06+nl-MBD functionals. In this case, the long-range vdW interactions are treated at the same level, but the short-range exchange term differs: HSE06 includes a fraction of exact exchange. HSE06 functional yields larger adsorption energy (1.03 eV), and the equilibrium distance to the surface becomes even smaller (3.30 Å). We can therefore assume that decreasing the self-interaction error strengthens the bonding of molecules to the surface. For further calculations, we use *light* settings of the FHI-aims code and PBE+vdW^{surf} functional. A comparison of the adsorption curve between *light* and *tight* settings is shown in figure B.1 in the Appendix. An increase of the basis set and density of real-space grids slightly decreases binding (by 58 meV), but we consider the effect small enough to proceed with lighter settings, because the computational overhead of *tight* settings is considerable. Looking at the adsorption curves, we note that the well is visibly asymmetric near its bottom, therefore inclusion of anharmonic effects will shift the mean distance to the surface

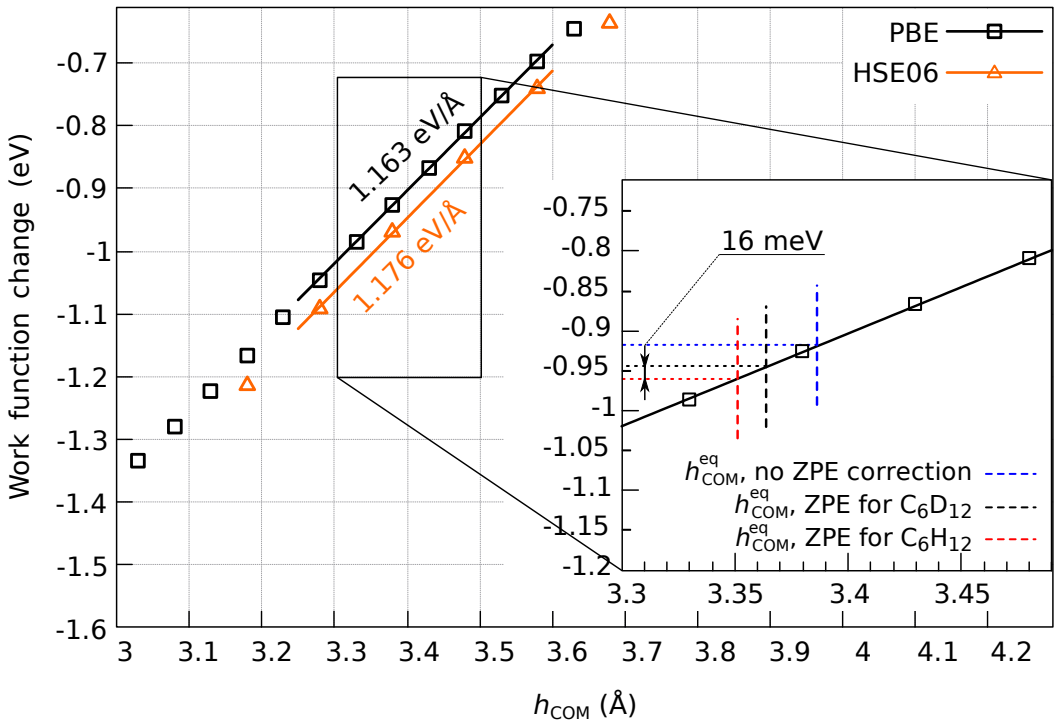

Figure 4.7: Work function change as a function of distance to surface, calculated with PBE (black squares) and HSE06 (orange triangles). Vertical dashed lines in the inset mark the equilibrium distances for classical nuclei (blue), C_6D_{12} (black) and C_6H_{12} (red). The figure is reproduced from the publication [7].

compared to the harmonic picture.

4.3.3 Quasi-harmonic approximation

Since the adsorption curve clearly exhibits anharmonicity near its minimum, we investigate the nuclear quantum effects with respect to the molecule-surface distance. We calculate harmonic phonons and the corresponding ZPE contribution to the adsorption energy for different molecule-surface distances, and do so for both isotopologues. Somewhat technical, but important question is how to treat rigid translations and rotations of the molecule, which are free at large distances to the surface, but become hindered when approaching the equilibrium distance. We included into the ZPE correction only $(3N_m - 3)$ molecular vibrations, where N_m is the number of atoms in a molecule, end explain the reason in a separate section 4.3.4.

The quasi-harmonic (QH) ZPE-corrected energy of adsorption E^*_{ads} was then calculated at each distance according to eq. 4.5. The results are presented in figure 4.5. The adsorption energies and distances obtained for C_6H_{12} and C_6D_{12} in this way are also summarized in table 4.2. With this procedure, a deformation of the binding energy curve that is different for C_6H_{12} and C_6D_{12} is predicted, such that C_6H_{12} has a larger binding energy and adsorbs closer to the surface than C_6D_{12}. The H-D adsorption energy difference is **37** meV, which is just slightly different from the value reported in table 4.1[3]. We have checked that adding finite temperature contributions in the HA to these values, up to 150 K, does not appreciably change this calculated isotope effect either (see figure 4.6).

Regarding the equilibrium distance of absorption, we observe an important effect. The adsorption distance of C_6H_{12} is **3.351** Å, and for C_6D_{12}, it is **3.364** Å. The H-D equilibrium distance *difference* $h^{\mathrm{D}}_{\mathrm{COM}} - h^{\mathrm{H}}_{\mathrm{COM}}$ is thus about **0.01** Å. It seems small, but this difference is enough to induce a noticeable effect on the work function change. The sensitivity of the work function change $\Delta\phi$ of the interface to the distance between the cyclohexane and the Rh surface is shown in figure 4.7. We calculated it by shifting an adsorbate rigidly closer to the slab and farther away from it. The work function depends linearly on the molecule-surface distance in the range around the equilibrium distance.

[3]The reason for the 1 meV discrepancy is the difference in definitions of E_{ads} and E^*_{ads}.

Table 4.2: Isotope effects on distance to surface and work function change, obtained by QH model and aiPIMD simulations with PBE + vdW$^{\text{surf}}$ functional for coverage $\theta = 0.46$.

	C_6H_{12}	C_6D_{12}	no ZPE
ZPE-corrected E^*_{ads} (meV)	1067	1030	956
QH h_{COM} (Å)	3.351	3.364	3.386
QH $\Delta\phi$ (meV)	-960	-945	-920
PIMD h_{COM} (Å)	3.41 ± 0.01	3.42 ± 0.01	3.416 ± 0.007
PIMD $\Delta\phi$ (meV)	-927 ± 9	-915 ± 9	-903 ± 5

The slope is **1.16** eV/Å with the PBE functional and **1.18** eV/Å with HSE06. The $\Delta\phi$ with HSE06 is about 0.06 eV larger than with the PBE functional. Regardless the XC functional, the H-D difference in $\Delta\phi$ which corresponds to the 0.01 Å difference in h_{COM} is **16-17** meV. This result qualitatively agrees with the experiment [8], although the experiment gives slightly larger value of ≈ 25 meV at $\theta = 0.46$. We obtained this value by a different fitting of the experimental data compared to what the authors did. We fitted a linear regression for the $\Delta\phi$ dependence on coverage reported in Ref. [8], in the interval $0.1 < \theta < 0.65$, and aligned the fits for C_6H_{12} and C_6D_{12} so that they coincide at $\theta = 0$. The reason to change the fitting procedure is that the reported data has only one point at zero coverage, which makes it unclear whether the θ=0 reference was different for C_6H_{12} and C_6D_{12} measurements or not. In the figure 4.8, we show the comparison of work function dependences on distance for two adsorption patterns with different coverage. Larger coverage considerably increases the value of $\Delta\phi$ and the slope $d\Delta\phi/dh_{\text{COM}}$ We show in the same plot the calculations performed with and without including the van der Waals energy into the energy functional in SCF cycle. Inclusion of self-consistent vdW interactions does not change appreciably the values or the slopes of $\Delta\phi$.

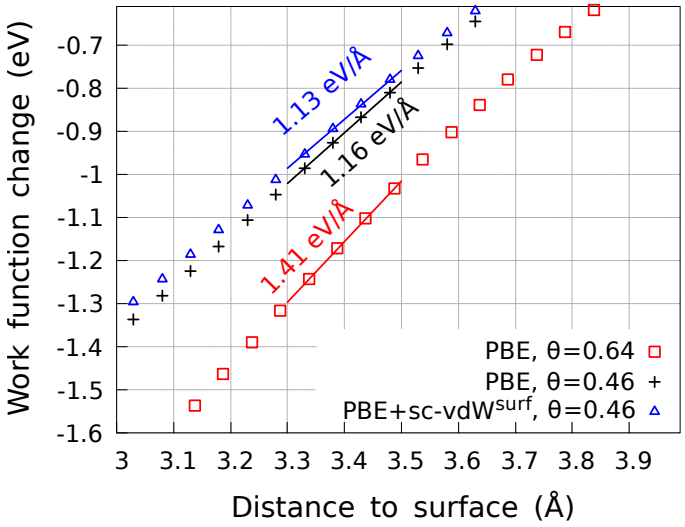

Figure 4.8: The work function change as a function of distance to the surface. Calculated by PBE for coverage 0.64 (red squares) and 0.46 (black crosses) and PBE + self-consistent vdW$^{\text{surf}}$ for coverage 0.46 (blue triangles).

4.3.4 QH model at finite temperatures: rigid translations and rotations

As mentioned above, we included into the ZPE correction for E^*_{ads} only $(3N_m - 3)$ molecular vibrations. The remaining 3 lowest-frequency modes (0 to 55 cm^{-1} depending on the distance to the surface) correspond to the hindered translations of a rigid molecule. They have completely classical behavior and high entropy, and they are populated at very low temperatures. Including them into the QH model is technically difficult because a) one of them is aligned with the parameter of the model (the distance to the surface) and is ill-defined except the equilibrium point; and b) the frequencies of the rest two translations, when calculated by finite differences, are very sensitive to noise in forces. The impact of this noise on ZPE correction is negligible, but it becomes divergent if one naively attempts to calculate vibrational entropy for these modes. Therefore we decided to exclude them from consideration, admitting that it decreases the applicability of the QH model at finite temperatures. Nevertheless, we give a rough estimate of finite-temperature effects by looking at remaining rigid rotations. In figure 4.6, we show harmonic free energy corrections at 150 K including $(3N_m - 3)$ modes, i.e. intramolecular vibrations and hindered rigid rotations, and only

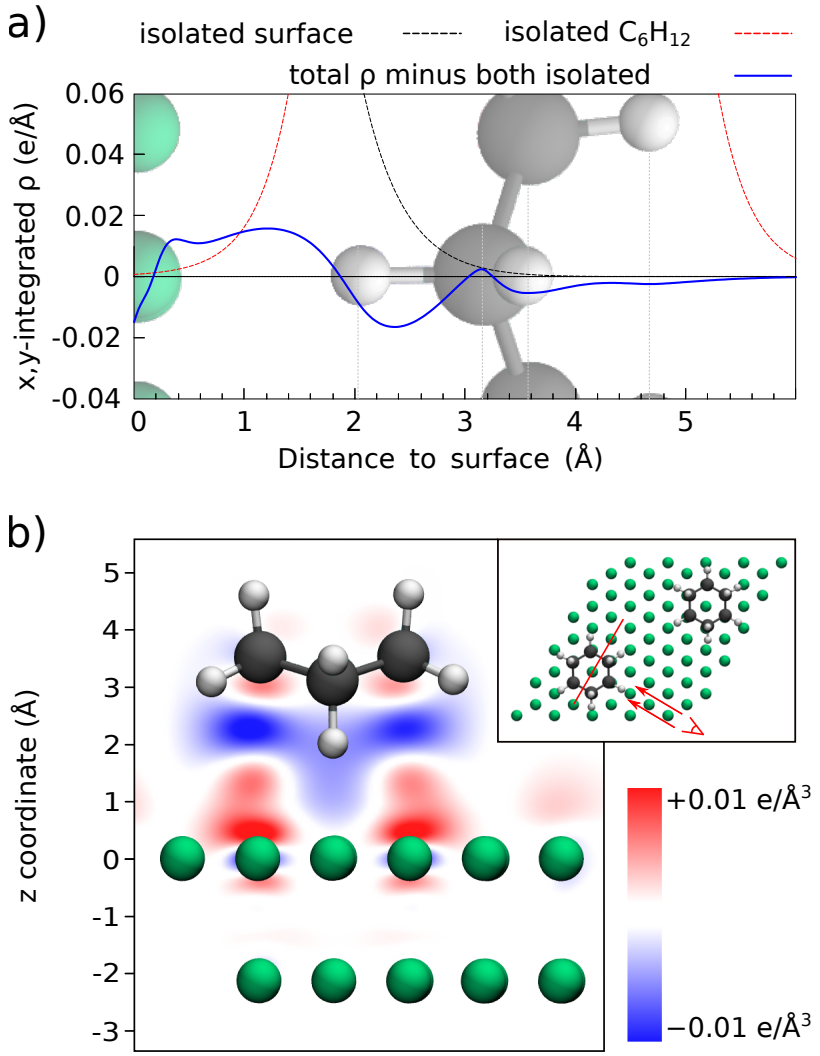

Figure 4.9: a) The electron density ρ of the interface integrated over the x and y dimensions and projected on the z axis. The dashed lines represent the electron densities of the clean surface and the adsorbate monolayer, calculated separately. The blue line shows the difference between the total density and the superposition of isolated parts. It shows the density accumulation between Rh and H atoms and the depletion in the C-H bond. b) The difference between the total electron density of the interface and the sum of the densities of the clean surface and the isolated adsorbate. Blue shows electron depletion, and red shows accumulation. The inset shows the unit cell and the slicing plane (the dashed red line). The position of the plane is chosen as shown in the inset. The figure is reproduced from the publication [7] with minor changes.

the $(3N_m - 6)$ intramolecular vibrations. Clearly, temperature effects are concentrated in the hindered rotations, and these effects are negligibly small in the higher frequency intramolecular vibrations. h_{COM} when including $(3N_m - 3)$ modes is **3.351 (3.365)** Å for H and **3.364 (3.384)** Å for D at the temperature of 0 (150) K.

4.3.5 The nature of the work function change

The work function change upon the adsorption of neutral and non-polar molecules like cyclohexane is typically attributed to two effects: (i) polarization of the molecule induced by the mirror charge that forms in metal [181] and (ii) a "push" of the electron density tail of the metal surface back towards the surface by the molecule due to the Pauli exclusion, often referred as a "pushback effect" [14, 182]. To get an insight into these effects, we calculate the electron density rearrangement upon adsorption. We do it by calculating first the full interface system, and then the clean Rh(111) surface and the cyclohexane molecule separately, using the same coordinates which they have in the full system. We calculate the difference between the full system and its "reactants" $\Delta\rho$ and plot it in two different ways: in figure 4.9a we plot $\Delta\rho$ integrated over the lateral dimensions of the interface, and in 4.9b we plot the cut through the molecule to see the spatial arrangement of $\Delta\rho$. There is an electron depletion in the C-H bonds and accumulation in the H$\cdots$Rh region, which is associated with H-Rh bond formation. Similarly to what was reported by Bagus *et al.* for cyclohexane on a Cu(111) cluster [182], we see the pushback effect: the tail of the electron density is shrunk under the molecule. In figure 4.9b, the redistribution of the electron density on a plane perpendicular to the surface, that crosses only carbon-carbon bonds, is shown. In this plane, the contribution of H-metal bonds is small, therefore the electron depletion which is present under the molecule can be mainly attributed to a pushback effect. It is difficult to separate the role of H-metal bond formation and the pushback effect clearly. By investigating the spatial arrangement of the electronic density changes, we conclude that the contributions of these two effects are of comparable magnitudes (see Appendix B, figures B.2 and B.3). Together, H-metal bonds and a pushback effect cause a **2.13** Debye per molecule decrease in the dipole moment of the interface.

4.4 Validity of the quasi-harmonic analysis

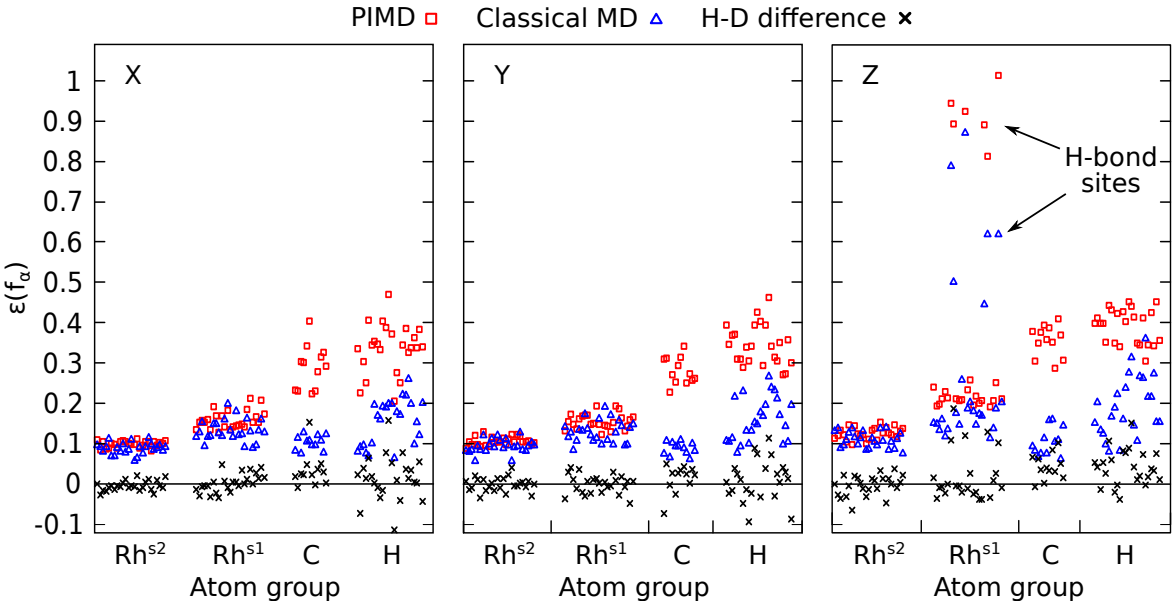

Figure 4.10: Anharmonicity measure ϵ (see eq. 4.7) for individual Cartesian components of atomic forces from the PIMD simulation of C_6H_{12} (red squares) compared to classical-nuclei MD (blue triangles), and difference in ϵ between PIMD simulations of C_6H_{12} and C_6D_{12} (black crosses). All values calculated for $\theta = 0.46$ (two cyclohexane molecules in the unit cell) and at $T = 150$ K. Rh^{s1} and Rh^{s2} denote the 1st and the 2nd layers of the surface atoms. The distinct group of Rh atoms with highly anharmonic z components consists of atoms connected to cyclohexane via hydrogen-metal bonds. The figure is reproduced from the publication [7] with minor changes.

The QH model gives a sufficient explanation of the isotope effects on geometry and work function change. It gives qualitative and, under certain assumptions, quantitative approximation of these effects. However, these assumptions are obvious weak points of the approximation – particularly, the assumption that all the vibrational modes of the adsorbate, except one, are either harmonic or not coupled to the isotope effects (the hindered rotations). Therefore it is important to estimate the quality of the QH model for such kind of molecular systems.

PIMD method described in section 3.1.2 can be employed in this context, in order to calculate static thermodynamic averages with full accounting for anharmonicity of

the PES. However, given the need for an *ab initio* PES and quite large size of the studied system, AI-PIMD simulations of this sort are computationally expensive since converging statistical averages requires long MD trajectories.

Therefore, we make a simpler test of the anharmonicity of the system before turning to PIMD. We study the anharmonic contributions to the forces in this system and separate nuclear quantum effects from classical finite-temperature effects. For this purpose, we use the method described in Ref. [183] and calculate an anharmonicity measure ϵ for different degrees of freedom. Since it is interesting to compare the difference between quantum and classical anharmonic contributions to different coordinates in the system, we calculate

$$\epsilon(T)^{\mathrm{CL/QM}} = \sqrt{\frac{\langle (F_{\mathrm{DFT}}^{\mathrm{CL/QM}} - F_{\mathrm{h}}^{\mathrm{CL/QM}})^2 \rangle_T}{\sigma^2_{F_{\mathrm{DFT}}^{\mathrm{QM}}}(T)}}, \tag{4.7}$$

where F_{DFT} are the full forces calculated by DFT, F_{h} are the harmonic forces calculated for the same geometry and with the Hessian matrix obtained for the full system, σ^2 is the variance, and $\langle \dots \rangle_T$ is the ensemble average at the temperature T. The superscripts CL and QM denote a classical-nuclei (AIMD) and a quantum-nuclei (AI-PIMD) simulations, respectively. In the latter case, it is important to take the forces on the actual bead positions, not on the centroid position. We normalize both classical and quantum quantities by the respective PIMD variance of that quantity so that the difference $\epsilon(T)^{\mathrm{QM}} - \epsilon(T)^{\mathrm{CL}}$ serves as a measure of "quantum anharmonicity": the part of the anharmonic contribution that is not included in a classical-nuclei estimation.

We calculate $\epsilon(T)$ and resolve it into Cartesian components of force on individual atoms and plot it in figure 4.10 for C_6H_{12} along with the H-D difference (all calculations with PBE+vdW$^{\mathrm{surf}}$). Such an analysis shows, as one could expect for a weakly bonded interface, that the forces acting on the adsorbate atoms exhibit the most pronounced anharmonicity. The rhodium surface is largely harmonic, with exception of those atoms which bond to the hydrogen atoms of cyclohexane, pointing towards the surface: those Rh atoms have a substantially anharmonic z-component of the force. We see also that classical and "quantum anharmonicity" are nearly the same at the surface, except at the aforementioned bonding sites, while at the adsorbate "quantum anharmonicity" exceeds the classical one considerably in all 3 dimensions. At the same time, the H-D

difference is very small in all considered atoms. We can draw three conclusions from this analysis: (i) the quasi-harmonic model with the molecule-surface distance as a parameter is likely to capture the effects of H$\cdots$Rh bonds, because they are concentrated in the z direction; (ii) there is a pronounced anharmonicity in the cyclohexane/Rh(111) interface, and quantum anharmonicity is higher than the classical one, therefore PIMD simulation is likely to improve the prediction of statistical observables; (iii) however, the contribution of quantum anharmonicity on C_6H_{12} and C_6D_{12} is similar, suggesting that they could largely cancel out in the evaluation of isotope effects.

4.5 Fully anharmonic model: path integral molecular dynamics

We estimated structural properties of the classical and quantum C_6H_{12} and C_6D_{12} on Rh(111) at 150 K directly from the AIMD and AI-PIMD simulations ($\theta = 0.46$, PBE+vdW$^{\text{surf}}$). In addition, we managed to capture changes in the electronic structure including full electron-phonon coupling at the adiabatic limit, by averaging the desired electronic quantities of interest over the trajectories. The only drawback, as we will see below, is that even with the SL-RPC technique, statistically converging the small energy differences and structural changes observed upon deuteration is a very challenging task. We ensured at least 30 ps of trajectories for each of the systems that we consider (see sec. 4.2).

The results are summarized in figure 4.11. In panel a, we show the distribution of the distance from the adsorbate atoms to the top layer of the Rh(111) surface. As expected, a more localized position distribution is observed for C_6D_{12} than for C_6H_{12}, and it is even more localized for classical-nuclei cyclohexane. The inset in panel a shows that C_6H_{12} can reach closer to the surface than C_6D_{12} and classical-nuclei cyclohexane, but it was not possible to resolve differences in the average position h_{COM} to an accuracy of 0.01 Å.

In figure 4.11b, the distribution of work function values at 150 K is shown. Again, C_6H_{12} presents a broader distribution than C_6D_{12} and classical-nuclei MD. The distributions are shifted with respect to each other, and their mean values $\langle\Delta\phi\rangle$ are ordered

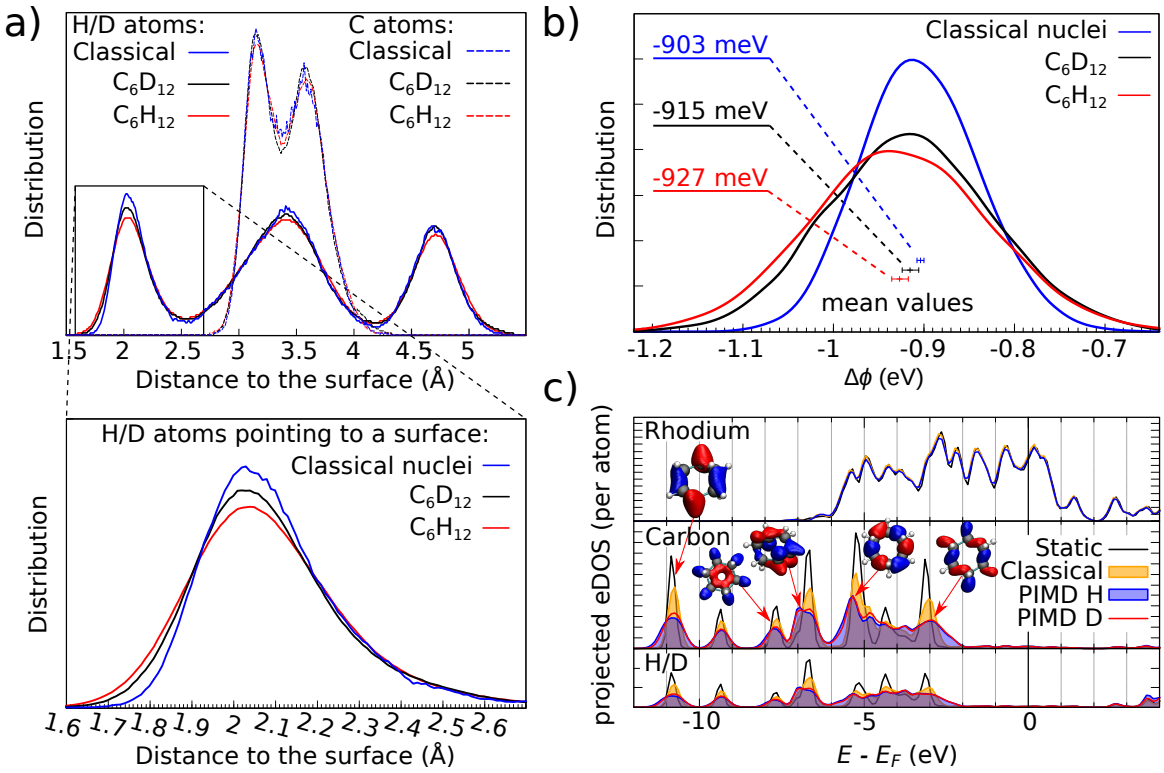

Figure 4.11: a) The distribution of distances from the Rh(111) surface to H/D atoms (solid lines) and C atoms (dashed lines). The red (black) lines show PIMD simulations of C_6H_{12} (C_6D_{12}), and the blue lines represent MD simulations with classical nuclei. b) The distribution of $\Delta\phi$ values for PIMD simulations of C_6H_{12} (red), C_6D_{12} (black) and classical MD simulation (blue). c) The species-projected electronic density of states in a single-point calculation (black), a classical-nuclei MD simulation (yellow), PIMD simulations for C_6H_{12} (blue) and C_6D_{12} (red). Peaks are broadened and shifted due to coupling with nuclear vibrations. Typical Kohn-Sham eigenstates are shown near the corresponding peaks. In all panels, $T = 150$ K. The figure is reproduced from the publication [7].

so that $\langle\Delta\phi\rangle_{\mathrm{H}} < \langle\Delta\phi\rangle_{\mathrm{D}} < \langle\Delta\phi\rangle_{\mathrm{Classical}}$. The resulting values for $\langle\Delta\phi\rangle$ are **−927 ± 9** meV for C_6H_{12}, **−915 ± 9** meV for C_6D_{12}, and **−903 ± 5** meV for classical-nuclei cyclohexane. We were careful in evaluating these uncertainties, by analyzing the autocorrelation behavior of this quantity during the simulation. The H/Classical difference is **24 ± 10** meV and we expect the H/D difference to be between zero and this value. In fact, we compute the H/D difference to be **12 ± 13** meV, which, despite the large uncertainty, shows the expected trend. Compared to the quasi-harmonic approximation (QHA), the AIMD and AI-PIMD simulations predict the molecules (with either classical or quantum nuclei) to lie farther away from the surface ($h_{\mathrm{COM}} = \mathbf{3.42 \pm 0.01}$ Å) by around **0.06 ± 0.01** Å (see estimation of h_{COM} within the QHA including temperature effects in the section 4.3.4). Accordingly, the AI-PIMD simulations predict a considerably smaller overall work function change. This is a consequence of taking into account anharmonic contributions at a temperature of 150 K (we note that the rigid "out of plane" vibrations of the adsorbates lie around 80-130 cm^{-1}, thus having components that are thermally activated at 150 K). This is also consistent with the high anharmonic score of the forces in the z direction, especially at H-bonded sites. Statistically converging the differences between C_6H_{12} and C_6D_{12} would require a considerable computational effort. However, with the current uncertainty intervals, it is possible to conclude that the isotope effects from the PIMD simulations cannot differ largely from the QH results, confirming that anharmonic contributions play a minor role in the geometric isotope effects in this potential energy surface. We were not able to calculate the isotope effect on the binding energies because, as mentioned previously, the SL-RPC approximation would have to include (many) more replicas of the system for an accurate assessment, which would make the calculations prohibitive.

Resolution of electron-phonon coupling

The AI-PIMD simulations give access to the changes induced on the electron density of states by the quantum fluctuations of the molecules. The nature of AI-PIMD restricts electron-phonon coupling to the adiabatic limit, neglecting electronic friction and other phenomena dependent on nuclear momenta. Nevertheless, it shows important changes, as discussed below. We project the total electronic density of states on

the atomic species using the Mulliken projection and average it over multiple snapshots of the simulations. The results are compared with the static density of states in figure 4.11c. There is a pronounced broadening of the peaks only on the adsorbate (for both quantum and classical nuclei), and this broadening is much more pronounced when considering quantum nuclei. We note that it is not clear if one can assign any physical interpretation to such broadening of Kohn-Sham single-particle orbitals. Nevertheless, this effect is caused by the dependence of these ground-state orbital energies on nuclear configurations and the interplay of this dependence with the distribution of nuclear configurations. In addition, there are considerable energy shifts due to this electron-phonon interaction in levels associated with sp^3 orbitals. Since sp^3 orbitals are responsible for C-H bonding, we tentatively correlate these shifts with the anharmonic effects in ZPE, which effectively change the length of the bonds and therefore the electronic structure as well. The semilocal/nonlocal functionals we employ are not able to provide a quantitative level alignment of this interface, even if they can predict the HOMO level reasonably well because of the cancellation of the self-interaction error and the missing image-potential effect [184, 185]. Even though a much higher level of theory, e.g. many-body perturbation theory, would be desirable for a quantitative comparison with UPS experiments conducted at this interface [175], the magnitude of changes that we observe in the Kohn-Sham electronic density of states highlights the importance of taking nuclear fluctuations into account when analyzing the electronic spectra of such interfaces.

4.6 Conclusions

We have studied isotope and anharmonic effects on the cyclohexane/Rh(111) interface by means of DFT calculations coupled to harmonic lattice dynamics, AIMD, and AI-PIMD.

Employing a QHA, in which the harmonic ZPE contributions were calculated with the molecule fixed at different distances from the surface, it could be shown that the binding energy of C_6D_{12} is smaller than C_6H_{12} and that C_6D_{12} lies 0.01 Å farther from the surface than C_6H_{12}, in qualitative agreement with the isotope effects previ-

ously observed experimentally [8] at the same interface. By showing that the work function change of the interface is very sensitive to the distance between the molecule and the surface, this geometrical isotope effect could be correlated with the isotope-induced change in the work function, thus confirming the hypothesis that Koitaya, Yoshinobu and coworkers proposed [168], based on experimental observations. Finally, these simulations also showed that the electronic-density rearrangement at the interface is impacted by both bond formation and the pushback effect and that the inclusion of van der Waals contributions improves the energetics and adsorption distances.

The reliability of the QHA was assessed by estimating the degree of anharmonicity of the nuclear motions at a temperature of 150 K. Anharmonic contributions to the forces are particularly pronounced at the surface sites which bond to hydrogens and on the degrees of freedom describing the adsorbates. In these cases, in particular, the difference between classical and quantum anharmonic contributions is also large, meaning that techniques like PIMD are necessary to describe structural aspects and related electron-phonon interactions in these systems. However, the *quantum* part of the anharmonic contributions to C_6H_{12} and C_6D_{12} are very similar in magnitude and character for coordinates parallel to the surface, and thus play a minor role when addressing isotope effects. This explains why the QHA fares well for these quantities in this case.

Indeed, in the AIMD and AI-PIMD simulations, the pronounced anharmonic character of certain degrees of freedom in the out-of-plane direction cause the equilibrium distance of the adsorbates to be around 0.06 Å farther from the surface than a static evaluation or the QHA would predict. This effect stems mostly from anharmonic terms that are already captured with classical nuclei. This is accompanied by considerably smaller work function changes. However, as expected due to the small contribution of quantum anharmonic effects beyond the QHA and within the statistical error bars, the observed isotope effects on this system (distance to surface and work function change) do not differ significantly from the QH case. Finally, the effect of electron-phonon coupling on the electronic density of states in the adiabatic limit causes a pronounced shift (and broadening) of Kohn-Sham levels related to the CH bonds.

Although we obtain excellent qualitative agreement with the experiment and are

able to provide an atomistic view of the origins of the isotope effects measured in this interface, there are still remaining differences in the magnitude of the isotope effect, in particular on the adsorption energy. We are left with the conclusion that this disagreement is likely coming from slightly different conditions in the experiment e.g., clustering of molecules at lower coverages, or the remaining approximations that were employed in this work. The most prominent approximations are the DFT functional and the SL-RPC approximation. We also cannot rule out that very slow degrees of freedom are not sufficiently sampled within the dynamical simulations. Nevertheless, we suggest that the exchange-correlation functional would be the largest source of remaining errors, given the known drawbacks that functionals based on generalized gradient approximations present for adsorbates on metallic surfaces [186], and the scatter of binding energies and distances we observed for different functionals and vdW corrections. Moreover, the functionals that yield good binding energies in comparison to the experiment, seem to predict a work-function variation with the distance to the surface that is too small. All of these observations motivate the training of fitted or machine-learned potentials that include long-range electrostatic interactions [187] and are based on more accurate potential energy surfaces [188, 189]. Such potentials would both decrease the cost related to statistical sampling and increase the (quantitative) predictive power of these simulations.

Chapter 5

Water electrolysis on a catalytic surface: Pd(111)

Reactions of water with surfaces occur in many situations. Sometimes it is a desired process, for instance, the production of hydrogen in an electrolytic cell, sometimes it is harmful corrosion. Many electrochemical reactions are conducted in an aqueous solution – the simplest well-known example would be a lead-acid battery where H_2SO_4 diluted by water serves as an electrolyte. Therefore the research of heterogeneous reactions involving water is a vast field existing for more than a century. The arrangement of atoms in the interface layer remains a topic of both experimental and theoretical research. Experimentalists use X-ray scattering and surface-enhanced IR spectroscopy to access such structural information and report that potential bias changes the orientation of molecules near the surface, affecting the chemical properties of the interface [190, 191].

From a theoretical standpoint, a correct description of water requires a quite high level of theory: it has many phases, and its liquid phase has an anomalous thermal expansion coefficient which changes its sign at 277 K. The network of hydrogen bonds and shared protons are decisive for water properties [192, 27]. These phenomena are dynamical in nature and have substantial contributions of nuclear quantum effects [193], therefore AIMD and even AI-PIMD methods are necessary to simulate water. The first attempt to approach water on AIMD level was done at the very dawn of the AIMD field by Parrinello, Car and coauthors [194], and to the end of 90s it was possible to

simulate bulk water on AI-PIMD level [195, 196, 197]. AIMD simulations to reveal the structure of the interface layer were for the first time performed by Izvekov *et al.* [198] in 2001, and then were significantly expanded by many researchers, as summarized in the recent review of Groß and Sakong [199].

Regarding the surface-mediated dissociation of water, there are still many open questions. Several groups reported studies of the splitting of a single water molecule on various transition metals, but without voltage applied and without accounting for long-range dispersion interactions [200, 201, 202, 203]. When a potential bias is applied to a water-metal interface, the issues discussed in section 2.6 come into play. Sugino *et al.* performed MD simulations for liquid water near the biased surface using a charged cell with effective screening medium (ESM) [204, 205] and Hagiwara *et al.* later further improved the setup using grand-canonical SCF technique, and calculated energy barriers of lateral diffusion of water molecule [5]. Hamada, Otani and their colleagues studied water dissociation under potential bias by means of AIMD [206, 207]. They ran relatively short MD trajectories (of a few picoseconds each) of a metal-liquid interface in the NVT ensemble. Although it may be enough to grasp some qualitative differences, a quantitative analysis would require much longer MD simulations and, probably, some acceleration technique to sample rare events properly – with the barrier of roughly 0.9 eV, spontaneous dissociation of water on Pd(111) is truly a rare event. Therefore, to the best of my knowledge, the behavior of the water dissociation barrier under potential bias remains largely unknown.

In this Chapter, I present our simulations of water dissociation on a Pd(111) surface under an electric field in a periodic slab model. First, I discuss the reactivity of the Pd(111) surface in an electric field and extend some of the results of Carrasco *et al.* [9] in section 5.2. Then, we reproduce the aforementioned NEB calculation of the dissociation barrier for a single water molecule at a zero-field Pd(111) surface and extend it to the case of a positive and negative electric field. I show the changes arising from the electric field and the influence of nuclear quantum effects on the barrier in section 5.3.

5.1 Details of simulations

We simulated a Pd(111) surface by a slab of 7 atomic layers in the periodic cell with a large vacuum layer of 64 Å. A dipole correction [1] was applied to compensate for spurious interactions between periodic images. The FHI-aims code with PBE XC functional was used. Dispersion interactions were included by the screened vdW$^{\text{surf}}$ model [10] with the coefficients for palladium taken from [110]. Lateral dimensions of the slab were chosen as 4×4 in order to reduce finite-size effects such as the interaction between periodic images of water as much as possible, while keeping the system reasonably small. The finite-size effect on the adsorption energy is shown in fig. 5.1, and the self-interaction of a water molecule in a periodic cell (spurious "cohesion energy") is shown for comparison. Both E_{ads} and this spurious interaction are saturated sufficiently at 4×4 unit cell. 3×3 k-points were used, which is consistent with the single-atom bulk

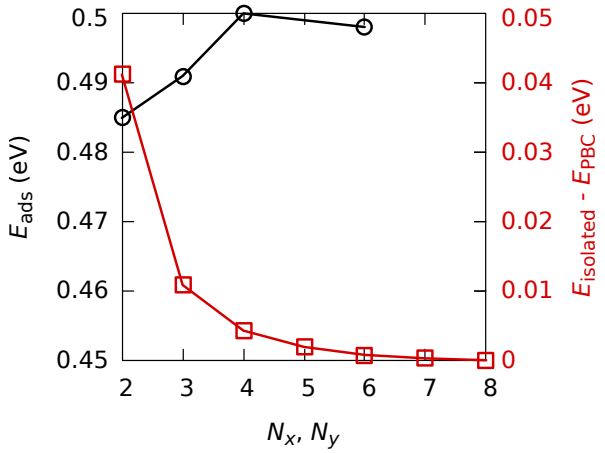

Figure 5.1: Adsorption energy of a single water molecule on a 6-layer Pd(111) slab as a function of the x, y dimensions of the slab (black) $N_{x,y} \times N_{\text{kpt}\,x,y} = 12$ for all points; the energy of a water molecule in the gas phase of the periodic cell of the same dimensions, compared to the non-periodic simulation (red). The values are calculated with PBE + vdW$^{\text{surf}}$.

Pd simulation with 12 k-points in each direction, which exhibits the cohesive energy converged below 10 meV and a converged FCC lattice constant of **3.95** Å.

We mimic potential bias by an electric field, as described in section 2.6.2. Two surfaces of the slab effectively become capacitor plates with opposite charges, and

the slab is thick enough to screen the surfaces from the electric field of each other, although they remain coupled by the charge conservation constraint. Dufils *et al.* showed recently on a model system that such a system exhibits very similar properties to a 2D-periodic setup with two metallic electrodes which are independently set to different potentials [2]. We see a linear dependence of the surface charge on the applied electric field in a range from –10 to +10 V/Å. An increase of the field by 1 V/Å induces a surface charge of **0.0364** electron per Pd atom, which is equivalent to **8.734** C/cm^2. The surface without an electric field is slightly negatively charged, which offsets the linear dependence by –0.012 e per atom. For shortness, I will refer to a field as "negative" or "positive" according to the charge that it induces to the surface of interest.

For the phonon calculations, a modified version [179] of the Phonopy package [178] was used, and only the water molecule and the first layer of the surface were included to build the Hessian. The deeper layers of the surface are included as a rigid environment By doing so, we lose the coupling Hessian elements between the atoms of the molecule and the surface beyond the first layer, which affects low-frequency molecule-surface phonons. Since the molecule is small and light, we assume that long-wave collective vibrations of a surface do not play a significant role in water reactions, because the water molecule will simply move together with the slowly "breathing" surface, while the chemically relevant frequencies of the H-O-H bending and O-H stretching are separated from low-frequency modes by two orders of the time scale.

5.2 Reactivity of Pd(111) surface under an electric field

Before approaching a surface-mediated reaction mechanism, it is important to study the adsorption of the reactant at the surface. Wilke *et al.* suggested a simple and easily calculatable measure for the activity of different adsorption sites of a surface, based on how easily the local electron density can be changed [208, 9].

$$W(\boldsymbol{r}) = \frac{\rho(\boldsymbol{r}, T_{\mathrm{el},2}) - \rho(\boldsymbol{r}, T_{\mathrm{el},1})}{k_{\mathrm{B}}^2 T_{\mathrm{el},2}(T_{\mathrm{el},2} - T_{\mathrm{el},1})} \tag{5.1}$$

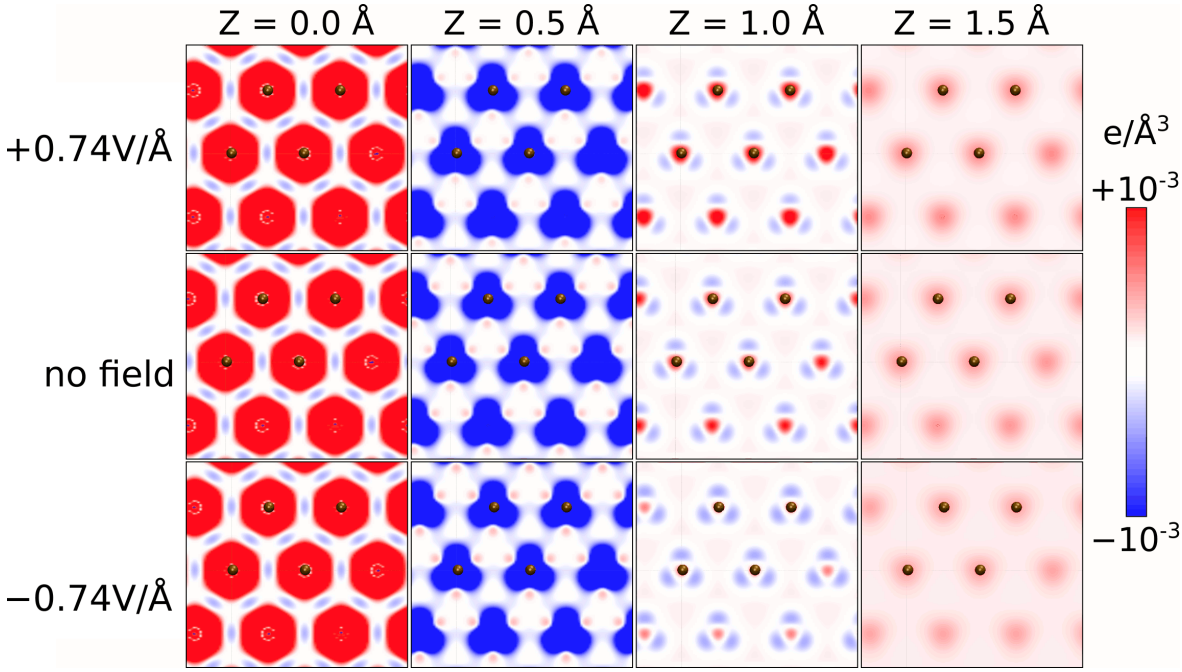

Figure 5.2: Parallel to surface plane slices of the electron density difference between the calculations with $T_{\mathrm{el},1} = 1.4$ meV and $T_{\mathrm{el},2} = 123.8$ meV. Four brown spheres show the atoms of Pd(111) surface lying inside the 2×2 unit cell. The difference to the results in [9] is probably related to the use of pseudopotentials in that work, while we used an all-electron code.

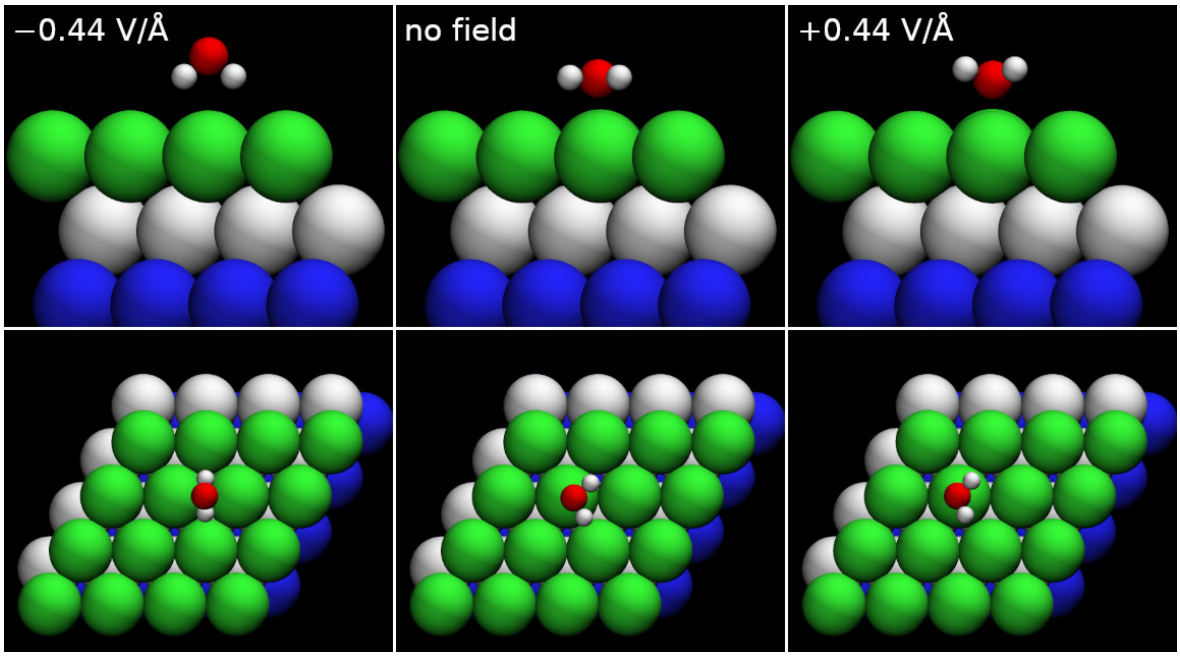

Figure 5.3: Adsorption geometries of a single water molecule on Pd(111) surface under –0.44 V/Å (left), no field (center) and +0.44 V/Å (right). Large green, white and blue spheres denote the 1st, 2nd and 3rd layers of the Pd(111) surface, respectively.

The electron density difference between the calculations with electronic temperatures 1.4 meV and 123.8 meV is shown in fig. 5.2. I plot the electron density difference instead of $W(\boldsymbol{r})$, because a normalization factor ($2.04 \times 10^6 \mathrm{J}^2$ for the chosen $T_{\mathrm{el},1}, T_{\mathrm{el},2}$) is only important to compare different materials. Surprisingly, $W(\boldsymbol{r})$ shows almost no dependence on the electric field applied to the slab and therefore cannot be an indicator of the changes induced by the field. In the range of electric fields from –0.74 V/Å to +0.74 V/Å, the atop site is the most electronically "soft". Following the discussion in paper [9], we would assume that a water molecule, which is also considered electronically "soft", reacts with the atop site in the whole range of electric fields. As we will see below, it is true for the neutral and positively charged surfaces, but not for the negatively charged surface, where electrostatic effects apparently dominate over the "hard and soft acid and base principle" of Pearson [209].

The adsorption geometries of a single water molecule at the electric field of –0.44 V/Å, 0 and +0.44 V/Å are shown in fig. 5.3. We found that the water molecule prefers a flat orientation if no field is applied, which agrees with previous works [200,

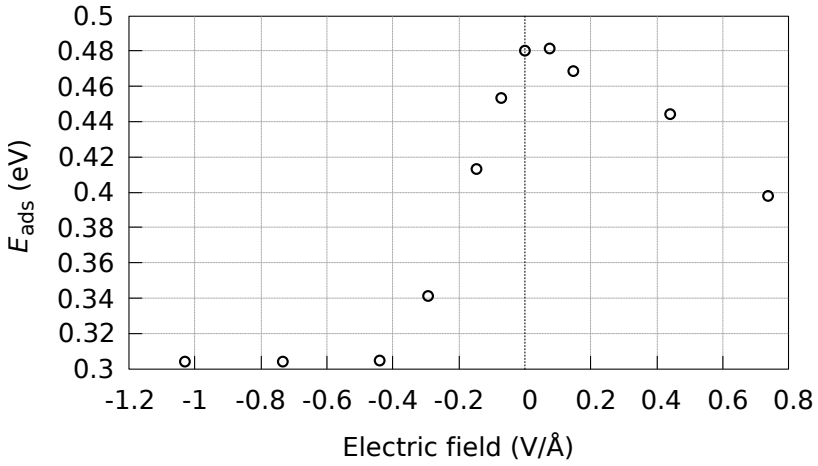

Figure 5.4: Adsorption energy of a single water molecule on the Pd(111) surface as a function of the applied electric field. The values are calculated with PBE + vdW$^{\text{surf}}$.

201, 202]. In a negative electric field, the flat orientation remains up to –0.37 V/Å, after which the molecule "stands up" pointing both hydrogen atoms towards the surface. In a positive field, the molecule deviates gradually from the flat geometry, and hydrogen atoms turn more and more towards the vacuum. We did not observe any abrupt changes in the range between –0.29 and +1 V/Å.

We calculated the adsorption energy of water in presence of an electric field, taking an isolated molecule relaxed in the same field as a reference – in order to have consistent contributions from the electrostatic potential. The adsorption energies E_{ads} are summarized in figure 5.4 and table 5.1. The highest adsorption energy is observed when no electric field or a slight positive field of 0.07 V/Å is applied. The value that we get without an electric field is 0.48 eV, which is expectedly higher than the values of 0.22-0.31 eV obtained in previous studies of water dissociation on Pd(111) [201, 202, 203], which we will use for comparison below. The reason is that no vdW interaction was included in those simulations. As we will see below, it is not very important for the dissociation barrier. When increasing the field towards positive values, E_{ads} gradually decreases. When a negative field is applied, E_{ads} gradually decreases up to a field of –0.44 V/Å, after which it remains the same. This change of the trend corresponds to the flip of the preferred adsorption orientation discussed above.

One important question is how the molecular energy levels align with the surface levels. We investigated it by projecting the total electronic density of states (DOS)

Table 5.1: Adsorption energy E_{ads} of a water monomer on a Pd(111) surface, depending on the applied electric field. The electric field of 1 V/Å corresponds to the surface charge of 0.0364 electron per Pd atom (8.734 C/cm^2). The values are calculated with PBE + vdW$^{\text{surf}}$, unless specified otherwise.

Electric field (V/Å)	E_{ads} (eV)	Note
+0.74	0.40	
+0.44	0.44	
+0.15	0.47	
+0.07	0.48	
no field	0.48	this work
	0.31	this work, PBE, no vdW
	0.33	[210] PW91, no vdW
	0.22	[201] PW91, no vdW
	0.30	[202] PW91, no vdW
	0.31	[203] PW91, no vdW
–0.07	0.45	
–0.15	0.41	
–0.29	0.34	
–0.44	0.31	
–0.74	0.30	
–1.00	0.30	

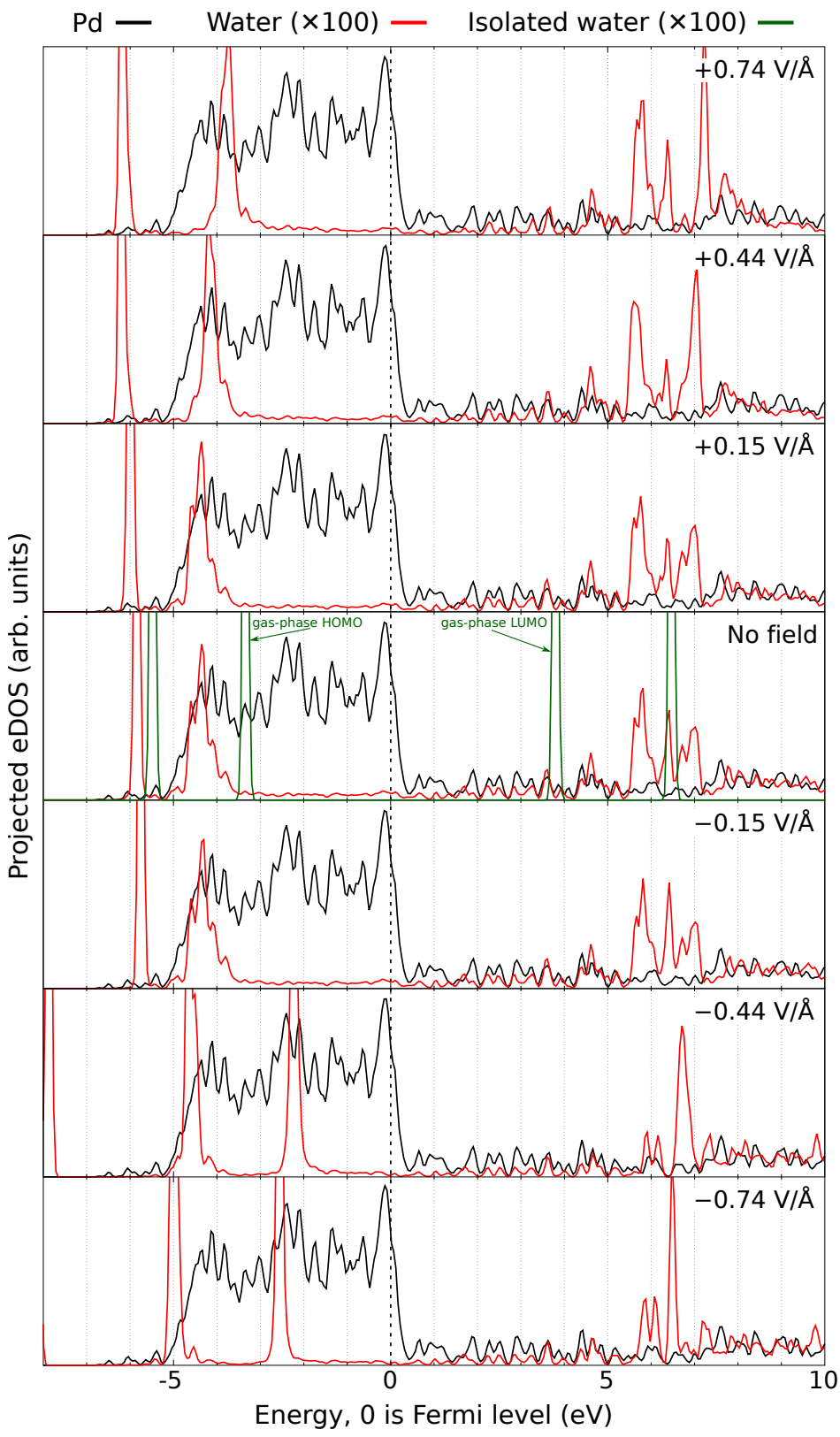

Figure 5.5: Electronic density of states projected on the atomic species at different values of an external electric field. The red lines denote Pd, the black lines – the sum of O and H contributions. Green line on the zero-field plot shows the DOS of an isolated water molecule, aligned so that its 1s orbital of oxygen matches that of the full system.

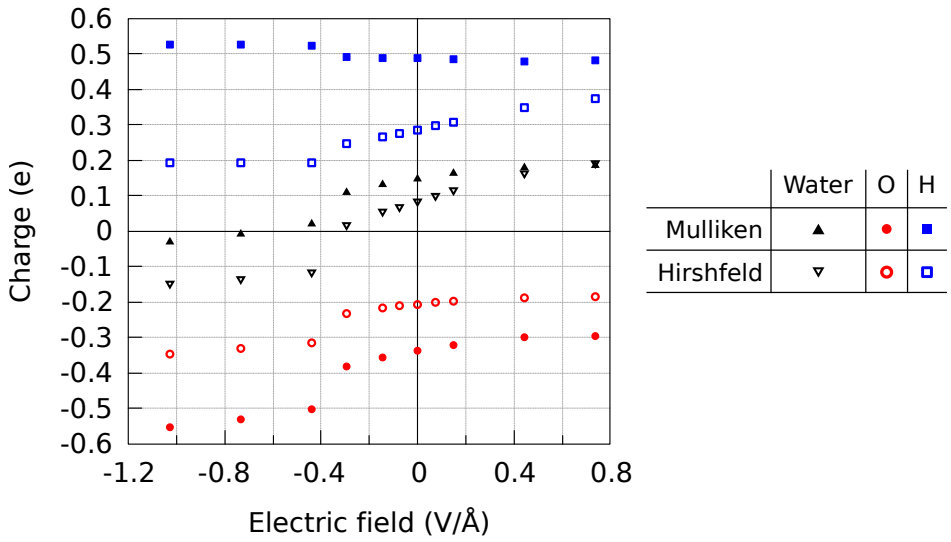

Figure 5.6: Charge induced on water molecule on Pd(111) surface depending on the applied electric field, measured by the Mulliken (filled points) and Hirshfeld (empty points) analysis. The black triangles show the total charge on the molecule, and the blue squares (red circles) show H (O) contributions to it.

on the atoms, employing a Mulliken analysis [211] on the numerical atomic orbitals of FHI-aims. We show such projected density of states (DOS) in fig. 5.5 and the charge induced on the water molecule, calculated by the Hirshfeld and the Mulliken analysis, in fig. 5.6. On a positively charged surface, Hirshfeld and Mulliken analysis agree. The molecule donates roughly 0.2 e to the surface, indicating orbital hybridization and electron transfer from the molecule to the surface. At an electric field below –0.44 V/Å, when the molecule "stands", the Mulliken analysis shows, in contrast, a negligibly small charge, while the Hirshfeld method shows again about 0.15 e. In addition, below –0.44 V/Å the hybridization of the highest occupied molecular orbital (HOMO) of the water molecule with the surface is reduced (see the peak at –2.5 eV in fig. 5.5). We can interpret the discrepancy between the Hirshfeld and Mulliken charges as a specific feature of the Hirshfeld definition of charge, which assigns local changes of the electron density to atoms proportionally to their free-atom electron density at the considered point. Therefore, a change of the "tail" of surface density can be assigned to the molecule even if there is no hybridization of the orbitals of the surface and the molecule.

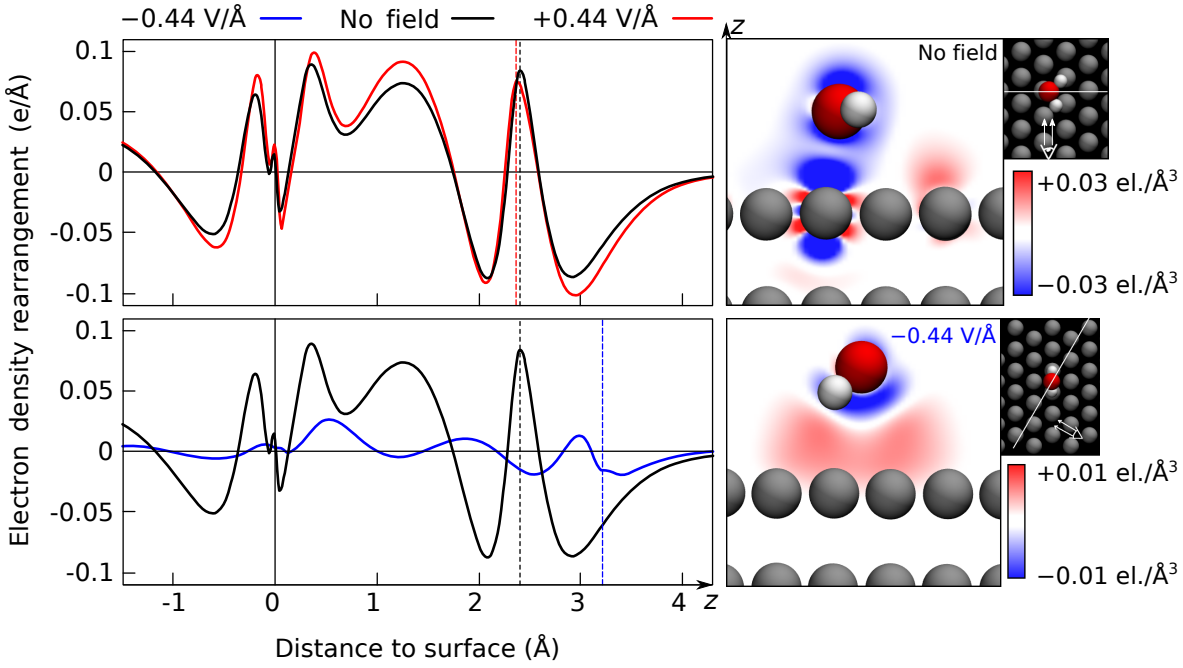

Figure 5.7: The difference between the electron density of the interface and its isolated subcomponents. Left: $\Delta\rho(z)$. Dashed lines show the positions of the oxygen atom: the blue line for the system at an electric field of –0.44 V/Å, the red line for +0.44 V/Å, and the black line for the system without an electric field. Right: the slices of the spatial distribution of the electron density difference. Blue color means electron depletion, red color means accumulation. The position of the slicing planes is marked by the white lines in the insets.

Similarly to what was done in Chapter 4, we can assess the influence of the electric field on the molecule-surface bond by examining how the electron density rearranges near the surface in the presence of the molecule. We subtract the electron densities of the clean surface and of the isolated molecule from the total density of the interface and integrate the difference over the directions parallel to the surface (x, y).

$$\Delta\rho(z) = \int dxdy \left[\rho_{\text{full}}(\boldsymbol{r}) - \rho_{\text{isolated water}}(\boldsymbol{r}) - \rho_{\text{clean Pd}}(\boldsymbol{r})\right]. \tag{5.2}$$

The results are shown in figure 5.7. Comparing zero-bias and +0.44 V/Å calculations, which have very similar adsorbed geometries, we can conclude that the electric field itself does not induce a large difference in electron density rearrangement – the difference comes mostly from structural changes.

5.3 Reaction paths in an electric field

We have calculated the reaction path of dissociation of a single water molecule on a Pd(111) surface using the climbing-image nudged elastic band method (CI-NEB). The resulting NEB path and corresponding energies of the nodes for the zero-field case are shown in figure 5.8, and representative paths for positive and negative electric fields are given in figure C.1 in Appendix C. We verified the transition states by the normal mode analysis. In all cases, the transition state has exactly one imaginary-frequency mode, which corresponds to a direction of barrier crossing. The geometry of the transition state has little dependence on the surface charge, compared to the reactant state. The activation energy for each bias is summarized in fig. 5.9 and in table 5.2.

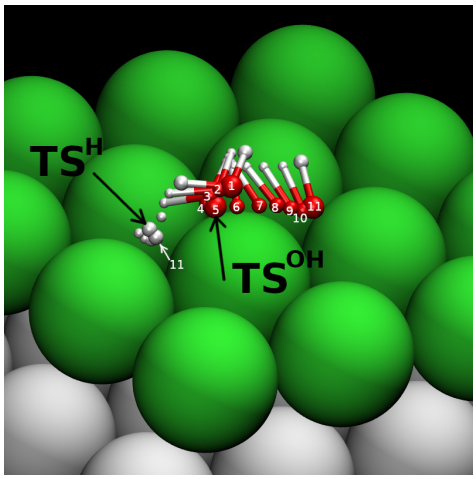

(a)

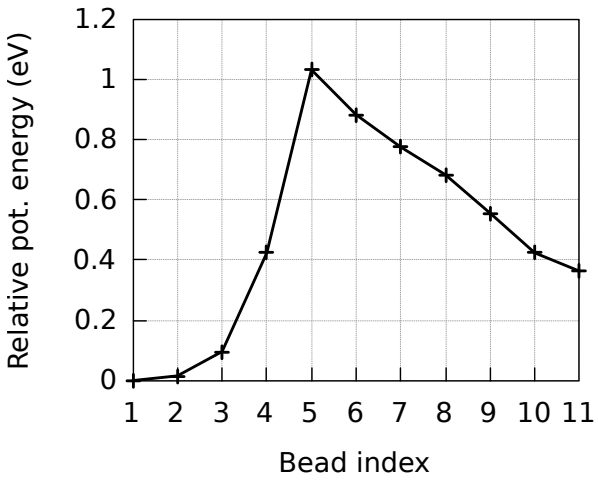

(b)

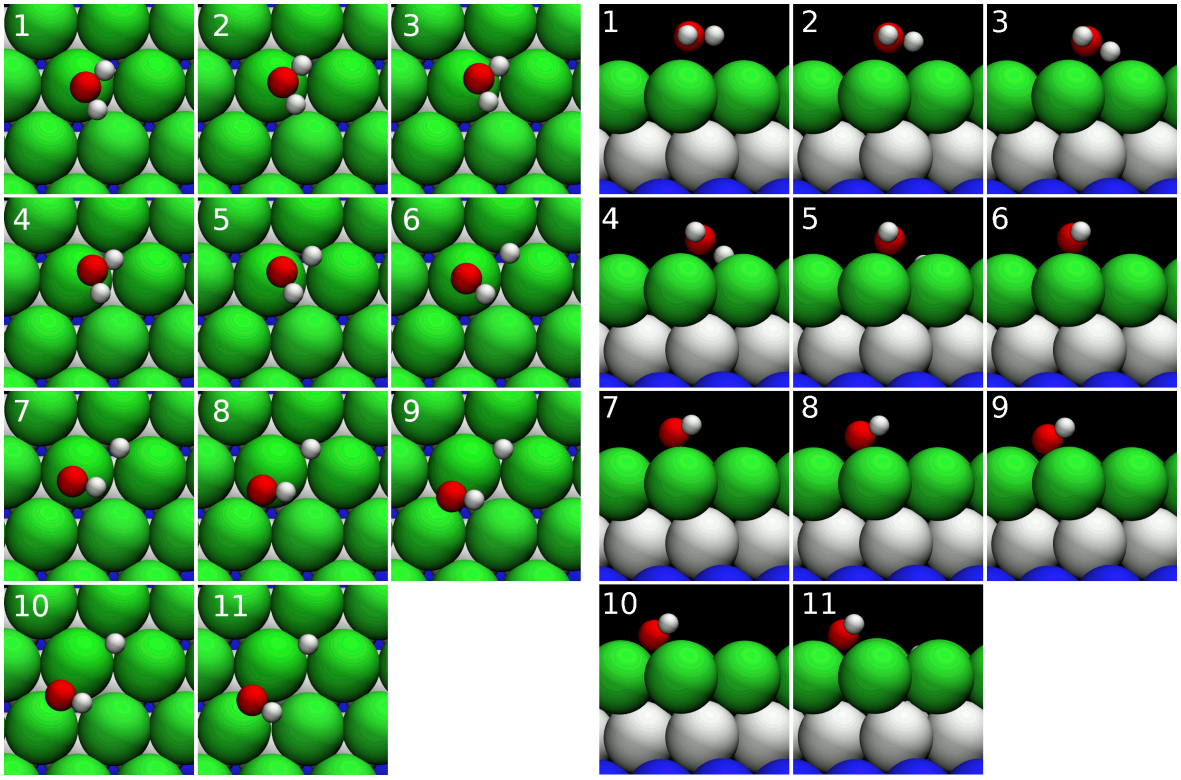

(c)

Figure 5.8: a) The reaction path of a water molecule splitting on a Pd(111) surface without an electric field applied, found by CI-NEB algorithm, a combined view of all NEB beads. The white numbers show the indices of NEB nodes, node 5 is the transition state; b) Corresponding potential energies relative to the reactant state. c)Individual NEB beads of the reaction path. Large green, white and blue spheres denote the 1st, 2nd and 3rd layers of the Pd(111) surface, respectively.

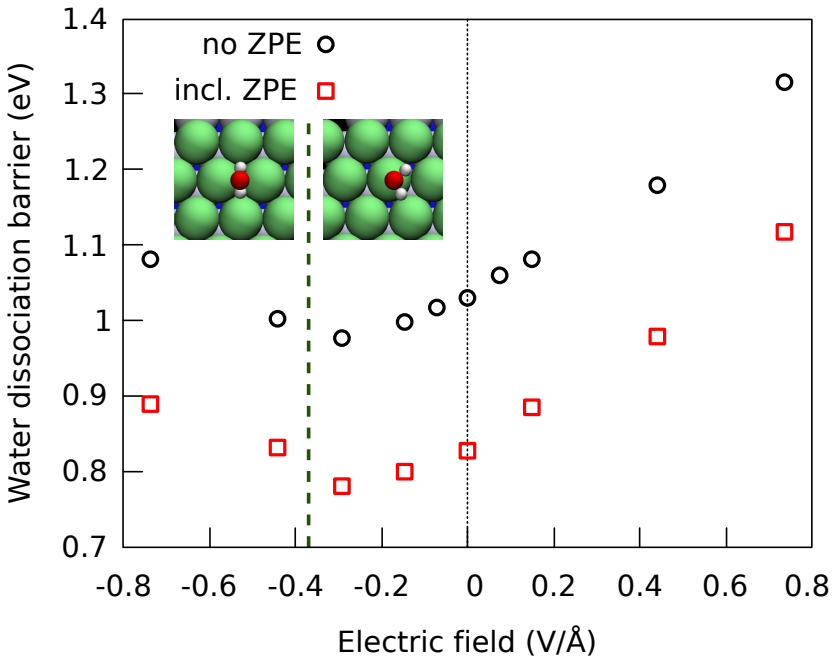

Figure 5.9: The energy barrier of water splitting calculated by CI-NEB algorithm. Black circles show the potential energy barrier, and red squares show the vibrational free energy barrier calculated in the harmonic approximation. The dashed green line marks the border between two orientations of the reactant state.

For zero bias, our value lies slightly (by 20-120 meV) below previously reported calculations [200, 201, 202, 203], which did not include dispersion interactions. Most of those authors used PW91 XC potential, but it was shown on various metals that the water dissociation barrier calculated by PW91 and PBE are almost identical, e.g. see the SI of [203]. Thus, the discrepancy with literature is consistent with the observation of Litman *et al.* that inclusion of vdW interactions decreases the barrier of dissociation of water on metals [143]. The lowest barrier is observed at –0.29 V/Å, directly before the water molecule changes its adsorption orientation. We calculated harmonic vibrational normal modes to evaluate the ZPE, and summarize the changes of the dissociation barrier in figure 5.9 and in table 5.2. The ZPE contribution decreases the barrier by roughly 0.19-0.20 eV at all points except –0.44 V/Å, where the decrease is 0.17 eV. Such a constant effect is somewhat surprising, given that the geometry of the reactant state changes considerably.

Table 5.2: Potential energy barrier E_a and ZPE-corrected barrier for the dissociation of a water monomer on a Pd(111) surface, depending on the applied electric field. The values are calculated with PBE + vdW$^{\text{surf}}$, unless specified otherwise.

Electric field (V/Å)	E_a (eV)	ZPE-corrected E_a (eV)	Note
+0.74	1.32	1.12	
+0.44	1.18	0.98	
+0.15	1.08	0.86	
+0.07	1.06	—	
no field	1.03	0.83	this work
	1.12	—	[200] PBE, no vdW
	1.09	0.87	[201] PW91, no vdW
	1.05	—	[202] PW91, no vdW
	1.15	0.96	[203] PW91, no vdW
–0.07	1.02	—	
–0.15	1.0	0.80	
–0.29	0.98	0.78	
–0.44	1.02	0.85	
–0.74	1.01	0.90	

In order to resolve the effects of ZPE, we look at the vibrational density of states (vDOS) spectra of the reactant and transition states, which are shown in figure 5.10, top and bottom, respectively. The most pronounced difference appears in the two hindered rotation modes of the reactant, which shift sharply from the range of 400-500 cm^{-1} down to 200-320 cm^{-1} when the field goes below –0.29 V/Å. These modes are shown in fig. 5.11. These modes are particularly softened at –0.44 V/Å, which indicates that the above-mentioned geometry flipping point is very close to –0.44 V/Å. In order to see more clearly how the shifts of the vibrational modes contribute to the total ZPE effect on the reaction barrier, we calculate a cumulative ZPE difference between the reactant and the transition state as follows:

$$\Delta^{\text{ZPE}}_{\text{cumul}}(\omega) = \sum_{\omega_i \leq \omega} \frac{\hbar\omega_i^{\text{TS}}}{2} - \sum_{\omega_i \leq \omega} \frac{\hbar\omega_i^{\text{ini}}}{2}, \tag{5.3}$$

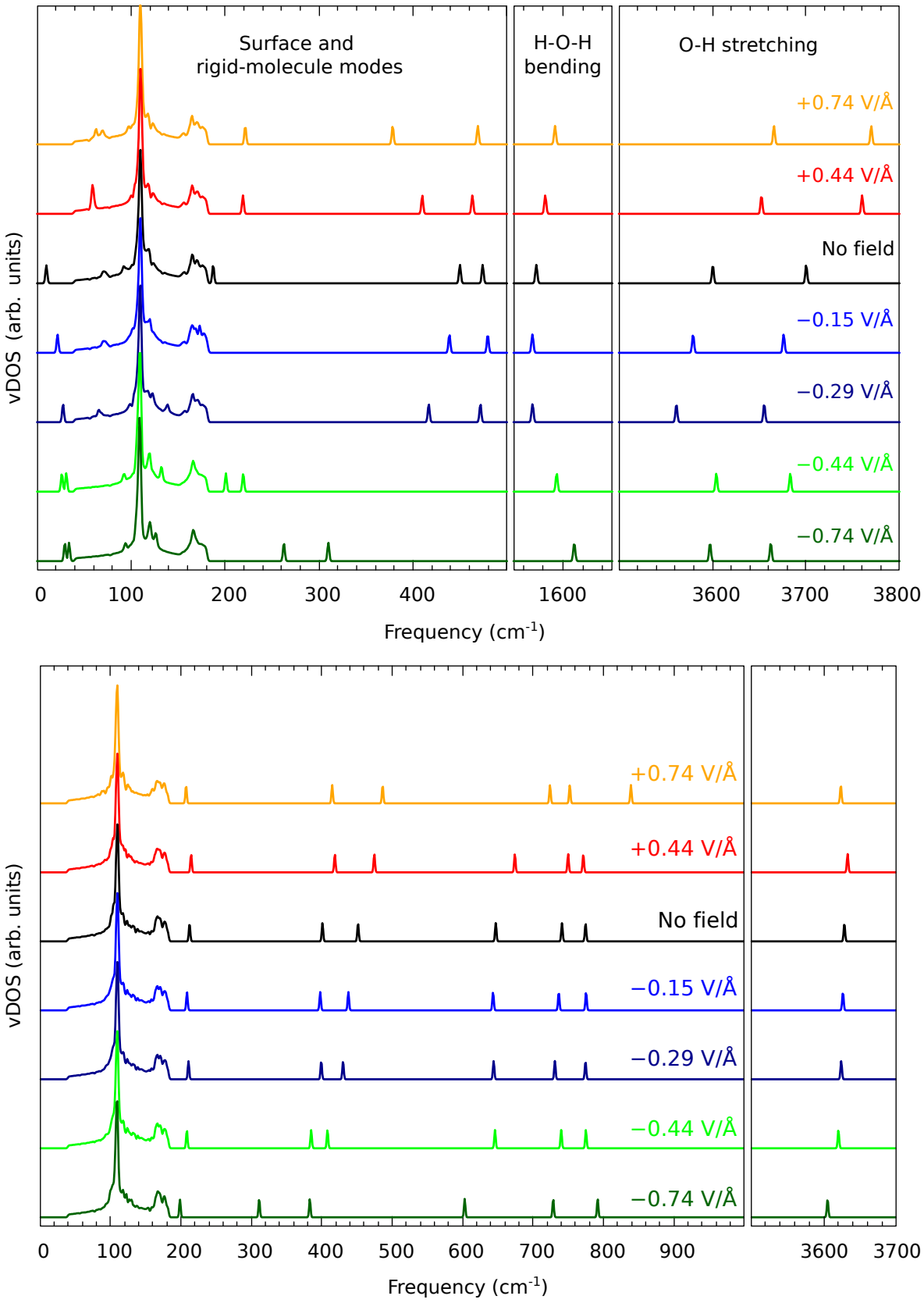

Figure 5.10: Vibrational density of states of the initial state (top) and the transition state (bottom) of water splitting reaction on a Pd(111) surface at different electric field values.

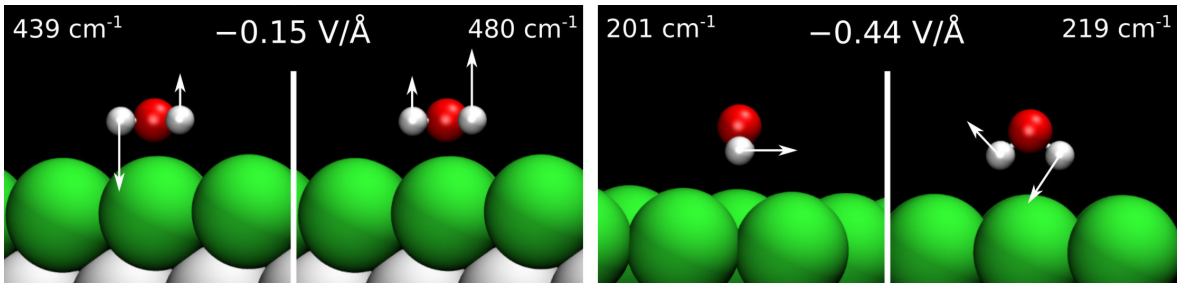

Figure 5.11: Hindered rotation modes of a water molecule on a Pd(111) surface at –0.15 V/Å (left) and –0.44 V/Å (right).

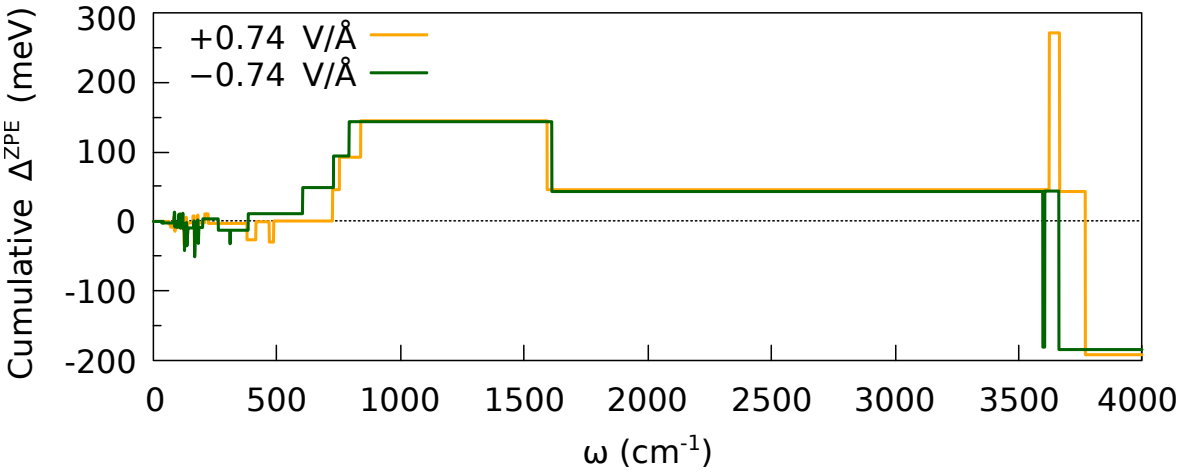

Figure 5.12: Cumulative contribution of the vibrational modes to the total ZPE effect on the barrier of water dissociation, calculated by formula 5.3.

where ω_i^{TS} and ω_i^{ini} are the normal modes of the transition state and the reactant, respectively. We show $\Delta^{\mathrm{ZPE}}_{\mathrm{cumul}}(\omega)$ in figure 5.12. One can see that despite multiple shifts of the individual modes, all the ZPE differences between the most distant electric field values of + and –0.74 V/Å below 1000 cm^{-1} cancel out, ending up with almost equal ZPE contribution to the barrier. The total ZPE effect comes almost entirely from the high-frequency modes, namely the H-O-H bending mode and one of the two O-H stretching modes, which exist in the reactant state and disappear at the transition state. It is important to note that hindered rotation modes are expected to be strongly anharmonic and thermally populated, therefore the harmonic analysis presented here gives only an estimate of the effect.

5.4 Conclusions and outlook

In this Chapter, we presented an *ab initio* study of water dissociation on Pd(111) surface subjected to an external electric field, using a periodic slab model. We showed that the previously suggested indicator of electronic "softness" of Wilke *et al.* [208] for the surface reactivity is not sensitive to an external electric field.

We showed *ab initio* calculations of the reaction path of water monomer dissociation on a Pd(111) surface under an electric field – a study that was not found in previous literature. We conclude that the main feature that affects the reaction barrier is the geometry of the reactant state, which is strongly influenced by the applied field. We demonstrated that the lowest dissociation barrier for the monomer lies at the electric field strength at which the molecule has two adsorption geometries equally preferred. We evaluated NQE limited to ZPE in the harmonic approximation and demonstrated that it reduces the barrier by roughly 0.2 eV, and this effect weakly depends on an applied electric field. The reason for such a weak dependence is the mutual cancellation of contributions of different vibrational modes. Harmonic approximation is an important simplification of the model, since the important contributions to the ZPE come from hindered rotations, which are expected to be anharmonic. The outlook that we have in mind to clarify this question is the use of MD-based methods such as umbrella sampling to calculate an anharmonic free energy profile along the reaction path.

Another simplification that we made is taking a single water molecule as an adsorbate. Clearly, a monomer does not give a realistic approximation of a structured water layer near the electrode, which is governed by the intermolecular interactions [192, 27]. We started to increment in this direction by modeling a dimer and faced unexpected difficulties. I summarize the results for the dimer in Appendix C.3. I expect this direction to be fruitful, therefore this work should be continued.

Finally, we simplified the model of the surface by constraining the total charge of the simulation cell to be zero, while a real electrode would allow charge fluctuations on a larger scale and, possibly, with a lower energy penalty. We investigated the existing openly available software to perform grand-canonical GF calculations, I summarize our efforts in Appendix C.4. Although we didn't achieve practical results so far, I think that simulation of the grand-canonical ensemble of electrons is the right direction to

increase accuracy, since it was demonstrated recently that the inclusion of surface charge fluctuations affects the reaction barrier of the lateral diffusion of water on a surface [5].

Chapter 6

Conclusions

"... and she threw in two mites,
which make a farthing."

Mark 12:42

In this thesis, I have summarized our theoretical studies of nuclear quantum effects on two systems containing molecules physisorbed on platinum-group metallic surfaces. These systems are relevant for hydrogen energy research and serve as model systems for hydrogen production and storage.

In Chapter 4, we have presented the simulations of cyclohexane adsorbed on the Rh(111) surface. We have shown, on one hand, that even in a weakly bound and fairly anharmonic system, such as the cyclohexane-rhodium interface, reasonably accurate results for the nuclear quantum effects in the electronic structure can be achieved by means of the quasi-harmonic approximation (QHA). Moreover, the quality of such predictions can be evaluated by the relatively simple estimator of anharmonicity of atomic forces, thus allowing a researcher to decide whether there is a need for more accurate methods such as AI-PIMD, or not, basing the decision on inexpensive calculations solely. On the other hand, we have shown that using higher-level AI-PIMD simulations we get access to properties beyond the reach of QHA, such as temperature-dependent renormalization of the electronic density of states, which stems from the coupling between thermally activated low-frequency vibrations, quantum fluctuations in high-frequency modes and the electronic orbitals. Therefore, a researcher can rationally choose a minimal necessary level of description to calculate a particular property.

Our failure to reproduce experimental results on the isotope effect in the adsorption energy of cyclohexane underline the need for such decision-making: if a property of interest (adsorption energy in this case) poses a demand for a higher level of electronic structure theory, while not exhibiting pronounced anharmonic effects, it makes sense to employ a simpler quasi-harmonic model and invest the computational resources to perform calculations with a more accurate XC functional.

A concern that we did not directly address in this study is the error that we introduced by applying the spatially localized ring polymer contraction (SL-RPC), in which we kept only the centroid mode to describe the molecule-surface interactions. Although we understood this could be an issue from the beginning, this choice was dictated by necessity, because increasing the computational cost of AI-PIMD simulations would have made them unreasonably expensive. This fact points to a problem that is known in the community: the increasing complexity of methods to treat nuclei creates a need for cheaper methods to treat the electronic structure, or at least to calculate potential energy surfaces. The dawn of machine learning methods in this field gives us hope to make PIMD simulations routinely available in the future, even though there are many challenges to overcome when using ML potentials for interfaces.

In the second study, summarized in Chapter 5, we have employed a simple model to simulate water splitting on an electrode surface: We used a periodic slab embedded in an external electric field. Using this model, we have obtained valuable results for the barriers of water splitting reaction in electric fields of various strengths. We have demonstrated that the ZPE contribution is nearly constant across a wide range of electric fields applied to the system due to the mutual compensation of red and blue shifts of individual vibrational modes between reactant and transition states. We do not consider such a weak dependence of ZPE on the field to be general, given that the geometry and the vibrational frequencies of the reactant change noticeably. Therefore, this phenomenon should be treated carefully in future work on similar systems.

We have demonstrated that the lowest barrier of water dissociation corresponds to a frustrated geometry of the reactant. Although the flip of the adsorption orientation of a water molecule is a feature of a single adsorbed molecule, which disappears with the increase of lateral interactions when multiple molecules are involved, it is reasonable

to assume that similar points of geometrical frustration exist in more complex adsorbate systems and to target them using an electric field (potential bias) as a control parameter.

Our setup allows local charge fluctuations near the adsorbate, effectively using the opposite side of the slab as a charge reservoir. However, the capacity of this reservoir is limited and cannot accommodate a substantial change in the charge state of an adsorbate. A real electrode allows charge fluctuations on a larger scale, therefore the next step in the modeling of an electrode would be to lift the constraint of zero total charge that we imposed on a simulation cell, and to move from the canonical to the grand-canonical ensemble of electrons. We investigated the state of the art in grand-canonical surface Green's function methods. Our tests of the existing openly available software for GF calculations led us to the conclusion that the numerical stability of those implementations does not allow for routine calculations of arbitrary materials at the moment. However, one can expect that the situation will improve in the near future.

Although we had to restrict our work to a small system with a single water molecule, the efficiency and scalability of the method make us sure that it is applicable on a larger scale. We put in place the necessary infrastructure for such calculations. On the electronic structure side, we have tested and streamlined the relatively new functionality for embedding a periodic system into an external electric field in the FHI-aims code, thus making sure that future researchers with less access to the source code can rely on this functionality. On the nuclear motion side, we have provided the community with the infrastructure for NEB calculations in the i-PI code, which may be used with many electronic-structure codes, providing a unified framework suitable for comparing and benchmarking the results across a broad community. Although our NEB implementation works well in many cases, it sometimes requires performing small optimization steps to achieve convergence, increasing the toll of force calculations. A promising way to improve the performance, while keeping the commonly accepted formalism of the original method, would be to employ a surrogate machine-learned potential as an intermediate PES [164]. ■

Appendix A

Estimate of the error of SL-RPC

A.1 The error in potential energy

The expression 3.19 can be rewritten as

$$\frac{k_B T}{2} \sum_i \sum_k \left[\frac{\omega_{\text{mol}}^2}{\omega_{(k)}^2 + \omega_{i,\text{full}}^2 + \Delta} - \frac{\omega_{\text{full}}^2}{\omega_{(k)}^2 + \omega_{i,\text{full}}^2} \right], \tag{A.1}$$

where $\Delta = \omega_{i,\text{mol}}^2 - \omega_{i,\text{full}}^2$. Since Δ is much smaller than $\omega_{(k)}^2 + \omega_{i,\text{full}}^2$, it can be omitted, and we immediately get eq. 9 from the Ref. [143]. It is a reasonable approximation of one fraction, which gives an error of not more than 10% in practical cases. However, these two fractions have quite close values, therefore the *difference* between them can be even smaller than the error introduced by omitting the Δ. This fact can lead to a significant overestimation of the error, if eq. 9 from [143] is used.

A.2 The error in free energy

Assuming a system to be harmonic, the Hamiltonian of a ring polymer with P beads in "physical" normal modes can be written as

$$H = K + \sum_{i=1}^{3N} \sum_{k=1}^{P} \left[\frac{m_i \omega_P^2}{2} \left(q_{i,(k)} - q_{i,(k+1)} \right)^2 + \frac{m_i \omega_i^2}{2} q_{i,(k)}^2 \right]. \tag{A.2}$$

Here K is a kinetic energy, i denotes normal modes (NMs) of a physical system, m_i is an effective mass associated with the normal mode i. Note that here, k stands for a

bead index – in contrast to the equations coming after the transformation (A.7), where it will enumerate normal modes of a free ring polymer.

Expanding the spring-terms and rearranging the summation over k (also making use of periodicity of a ring polymer $q^{(P+1)} = q^{(1)}$), one can rewrite a Hamiltonian as following:

$$H = K + \sum_{i=1}^{3N} \sum_{k=1}^{P} \left[\frac{m_i \omega_P^2}{2} \left(2q_{i,(k)}^2 - q_{i,(k)} q_{i,(k+1)} - q_{i,(k)} q_{i,(k-1)} \right) + \frac{m_i \omega_i^2}{2} q_{i,(k)}^2 \right]. \quad \text{(A.3)}$$

Then, the spring terms can be written in a matrix form (bold below means P-dimensional vectors $\{q^{(j)}\}, j \in [1, ..., P]$ and corresponding square matrices)

$$V^{spring} = \sum_{i=1}^{3N} \frac{m_i \omega_P^2}{2} \boldsymbol{q_i}^\top \boldsymbol{A} \boldsymbol{q_i}, \quad \text{(A.4)}$$

$$\boldsymbol{A} = \begin{bmatrix} 2 & -1 & 0 & ... & & -1 \\ -1 & 2 & -1 & 0 & & \\ 0 & -1 & 2 & ... & & \\ ... & 0 & ... & & & \\ & & & & & -1 \\ -1 & & & & -1 & 2 \end{bmatrix} \quad \text{(A.5)}$$

We diagonalize the $\boldsymbol{A}$ matrix by performing a normal mode transformation $\boldsymbol{C}$:

$$\boldsymbol{A} = \boldsymbol{C} \tilde{\boldsymbol{A}} \boldsymbol{C}^\top. \quad \text{(A.6)}$$

$$\tilde{\boldsymbol{q}}_i = \boldsymbol{C} \boldsymbol{q}_i \quad \text{(A.7)}$$

The matrix $\boldsymbol{C}$ is unitary, therefore the transformation to the normal modes of a free ring polymer doesn't change the physical potential term

$$\frac{m_i \omega_i^2}{2} \boldsymbol{q}_i^2 = \frac{m_i \omega_i^2}{2} \tilde{\boldsymbol{q}}_i^\top C^{-1\top} C^{-1} \tilde{\boldsymbol{q}}_i = \frac{m_i \omega_i^2}{2} \tilde{\boldsymbol{q}}_i^2. \quad \text{(A.8)}$$

The Hamiltonian in the "double normal-mode" representation (i.e. the normal modes of a physical system and the normal modes of a free ring polymer) reads as

$$H = K + \sum_{i=1}^{3N} \sum_{k=0}^{P-1} \frac{m_i (\omega_{(k)}^2 + \omega_{i,\text{full}}^2)}{2} \tilde{q}_{i,(k)}^2, \quad \text{(A.9)}$$

$$\tilde{q}_{i,(k)} = \sum_{j=1}^{P} C_{jk}^P q_{i,(j)} \quad \text{(A.10)}$$

where k denotes NMs of a free ring polymer. Here and below, "full" index stands for the "expensive" potential energy surface which describes all interactions in a system, while "mol" stands for the "cheap" one. In case of spatially-localized contraction, a "cheap" potential describes only interactions within an adsorbate.

Contraction procedure. Given a ring polymer of P beads, one can contract it to a lower dimensionality. Many useful expressions can be found in [141]. Equations 21-22 from [141], rewritten in our notation:

$$q_{i,(j')} = \sum_{j=1}^{P'} (T_P^{P'})_{j'j} q_{i,(j)}, \tag{A.11}$$

where

$$(T_P^{P'})_{j'j} = \frac{1}{P} \sum_{k=-P'/2}^{P'/2} C_{j'k}^{P'} C_{jk}^{P} \tag{A.12}$$

is a contraction matrix from $(P \times 3N)$ to $(P' \times 3N)$-dimensional space. It performs transformation C^P to a Fourier space, there it truncates the high-order coefficients and transforms back to a lower-dimensional real space by $C^{P'}$. Similarly, we define an expansion matrix $T_{P'}^{P}$ from $(P' \times 3N)$ to $(P \times 3N)$-dimensional space. The expansion procedure is a reverse of a contraction with only difference: instead of truncating Fourier series, we have to expand it from P' to P terms. Since we do not have these coefficients, we set them to be zero. It can be shown that the potential energies of the P- and P'-ring polymers are related as

$$\sum_{k=1}^{P} V(q_{1,(k)}, ..., q_{3N,(k)}) \approx \frac{P}{P'} \sum_{j=1}^{P'} V(q'_{1,(j)}, ..., q'_{3N,(j)}), \tag{A.13}$$

with respect to the accuracy of contraction.

The Hamiltonian after the SL-RPC is applied:

$$H = K + \sum_{i=1}^{3N} \left[\sum_{k=0}^{P'-1} \frac{m_i(\omega_{(k)}^2 + \omega_{i,\text{full}}^2)}{2} \tilde{q}_{i,(k)}^2 + \sum_{k=P'}^{P-1} \frac{m_i(\omega_{(k)}^2 + \omega_{i,\text{mol}}^2)}{2} \tilde{q}_{i,(k)}^2 \right]. \tag{A.14}$$

Then, the partition function of this system is

$$Q = \prod_{i=1}^{3N} \left[\prod_{k=0}^{P'-1} \frac{1}{\beta_P \hbar \sqrt{\omega_{(k)}^2 + \omega_{i,\text{full}}^2}} \prod_{k=P'}^{P-1} \frac{1}{\beta_P \hbar \sqrt{\omega_{(k)}^2 + \omega_{i,\text{mol}}^2}} \right] \tag{A.15}$$

The free energy of a (single) physical system:

$$
\begin{aligned}
F &= -\frac{1}{\beta}\ln(Q) = \\
&= -\frac{1}{\beta}\sum_{i=1}^{3N}\left[-\sum_{k=0}^{P'-1}\ln(\beta_P\hbar\sqrt{\omega_{(k)}^2+\omega_{i,\mathrm{full}}^2}) - \sum_{k=P'}^{P-1}\ln(\beta_P\hbar\sqrt{\omega_{(k)}^2+\omega_{i,\mathrm{mol}}^2})\right] = \\
&= \frac{3NP\ln(\beta_P\hbar)}{\beta} + \frac{1}{2\beta}\sum_{i=1}^{3N}\left[\sum_{k=0}^{P'-1}\ln(\omega_{(k)}^2+\omega_{i,\mathrm{full}}^2) + \sum_{k=P'}^{P-1}\ln(\omega_{(k)}^2+\omega_{i,\mathrm{mol}}^2)\right].
\end{aligned}
\tag{A.16}
$$

The free energy difference between SL-RPC and P beads calculated with full potential:

$$
\begin{aligned}
\delta F = (F^{RPC} - F^{P\ beads}) &= \frac{1}{2\beta}\sum_{i=1}^{3N}\sum_{k=P'}^{P-1}\ln\left(\frac{\omega_{(k)}^2+\omega_{i,\mathrm{mol}}^2}{\omega_{(k)}^2+\omega_{i,\mathrm{full}}^2}\right) = \\
&= \frac{1}{2\beta}\sum_{i=1}^{3N}\sum_{k=P'}^{P-1}\ln\left(1+\frac{\omega_{i,\mathrm{mol}}^2-\omega_{i,\mathrm{full}}^2}{\omega_{(k)}^2+\omega_{i,\mathrm{full}}^2}\right).
\end{aligned}
\tag{A.17}
$$

Appendix B

Supplementing details for Chapter 4

B.1 Availability of data

The outputs of static DFT calculations, such as phonon calculations and adsorption curves, are uploaded to the NOMAD repository `https://nomad-lab.eu`, the dataset DOI is 10.17172/NOMAD/2020.12.22-1.

B.2 Adsorption properties

Adsorption energies $E_{\text{ads}}^{\text{pot}}$ for the systems discussed in Chapter 4 are provided in table B.1.

A comparison of the adsorption energy curve between *Light* and *Tight* settings is provided in figure B.1 for $\theta = 0.46$. The difference in binding energy is 58 meV.

As mentioned in the main text, we use E_{ads} calculated by the eq. 4.1 and E_{ads}^{*} calculated by the eq. 4.5. Only E_{ads} rigorously satisfies the definition of an adsorption energy. Comparing the numbers for coverage 0.46 and PBE + vdW^{surf} in tables B.1 and B.2, one can compare the values obtained with these two definitions. The differences are very small (less than 10 meV).

Table B.1: Adsorption energy for different adsorption patterns, calculated with PBE+vdW$^{\text{surf}}$ by FHI-aims code with *Light* and *Tight* settings.

	$\boldsymbol{E_{\text{ads}}}$ $\left(\frac{\textbf{eV}}{\textbf{molecule}}\right)$
$\boldsymbol{\theta = 1, \left(2\sqrt{3} \times 2\sqrt{3}\right) R13.9°}$**, 9 molecules, 4 Rh layers**	
Light, 2×2×1 k-points	1.023
$\boldsymbol{\theta = 0.64}$**, 3×3 slab with 1 molecule**	
Light, 4×4×1 k-points	0.946
$\boldsymbol{\theta = 0.46}$**, 5×5 slab with 2 molecules**	
Light, 2×2×1 k-points	0.953
Tight, 2×2×1 k-points	0.912
$\boldsymbol{\theta = 0.12}$**, 7×7 slab with 1 molecule**	
Light, 2×2×1 k-points	0.945

B.3 Electron density rearrangement

Multiple slices of the electron density difference between the full system (surface+molecules) and the superposition of an isolated adsorbate and a clean surface are presented (figures B.2, B.3). In these pictures, shades of blue mean electron depletion upon adsorption, and shades of red mean electron accumulation.

Table B.2: Adsorption distance h_{COM} between the center of mass of a molecule and a surface, and energy E^{*}_{ads}, calculated as the energy difference between the minimal point of the adsorption curve and the point at 10 Å distance from the surface.

Calculation setup	h_{COM} (Å)	E^{*}_{ads} (meV)
$\theta = 0.46$, *Tight* settings		
PBE	3.71	147
PBE+nl-MBD	3.45	843
PBE + vdW$^{\mathrm{surf}}$	3.36	905
HSE06+nl-MBD	3.30	1026
$\theta = 0.46$, *Light* settings		
PBE + vdW$^{\mathrm{surf}}$	3.37	963

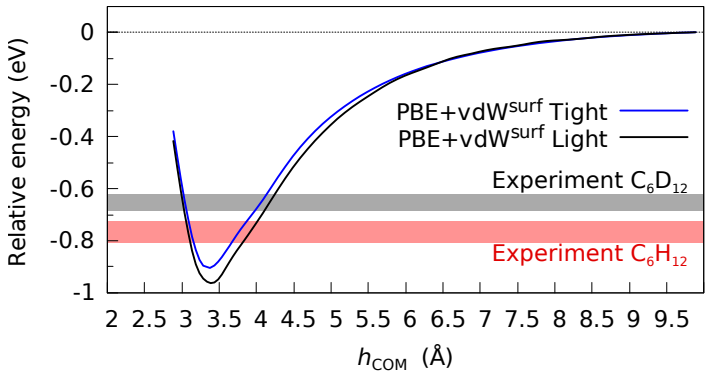

Figure B.1: Adsorption curves calculated with PBE +vdW$^{\mathrm{surf}}$ [10] functional with *Tight* (solid blue line) and *Light* (dashed black line) settings of FHI-aims. Calculations were performed with the unit cell of $\theta = 0.46$. Shaded areas show the experimental values of the adsorption energy of C_6H_{12} (red) and C_6D_{12} (grey), obtained by temperature programmed desorption [8].

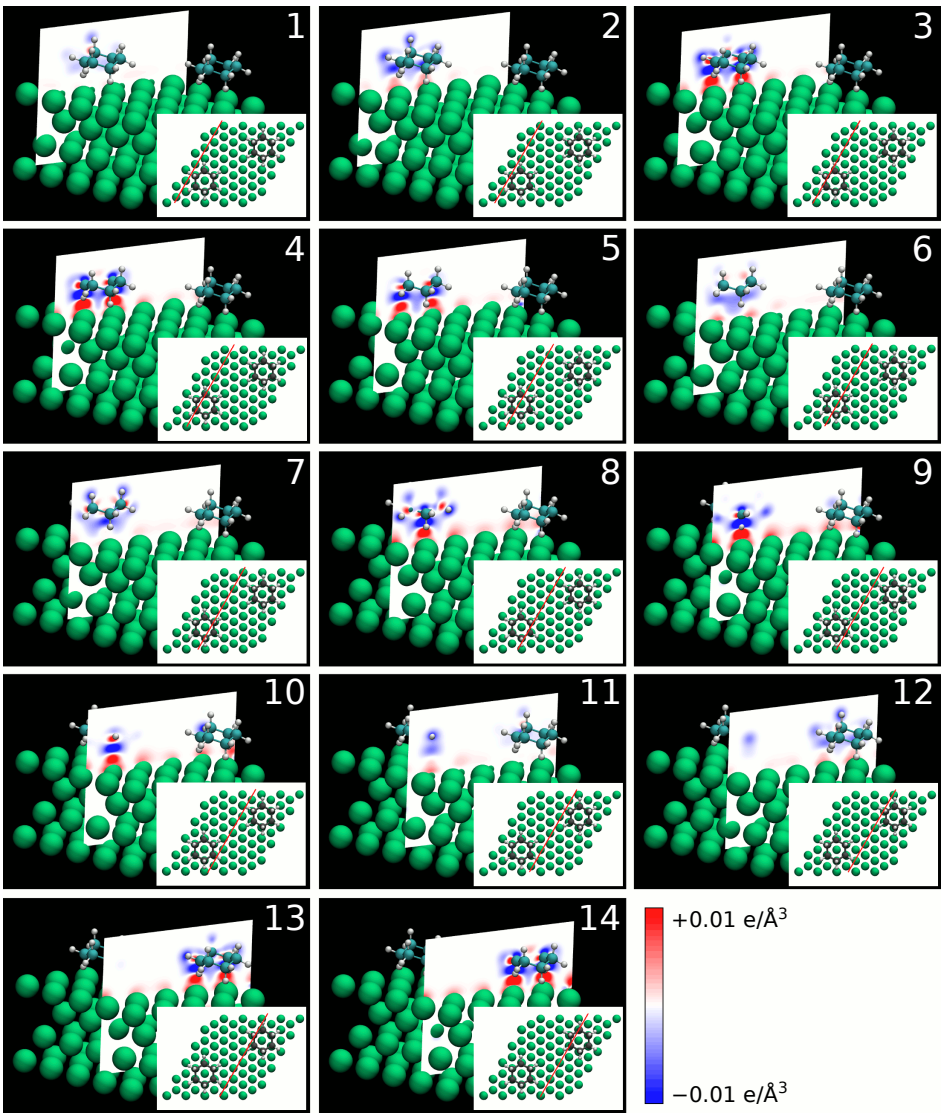

Figure B.2: Difference between the electron density of a surface with molecules adsorbed and the sum of isolated surface and isolated molecules, shown at different $y-z$ slices along x coordinate. Red color denotes electron density accumulation, and blue denotes depletion.

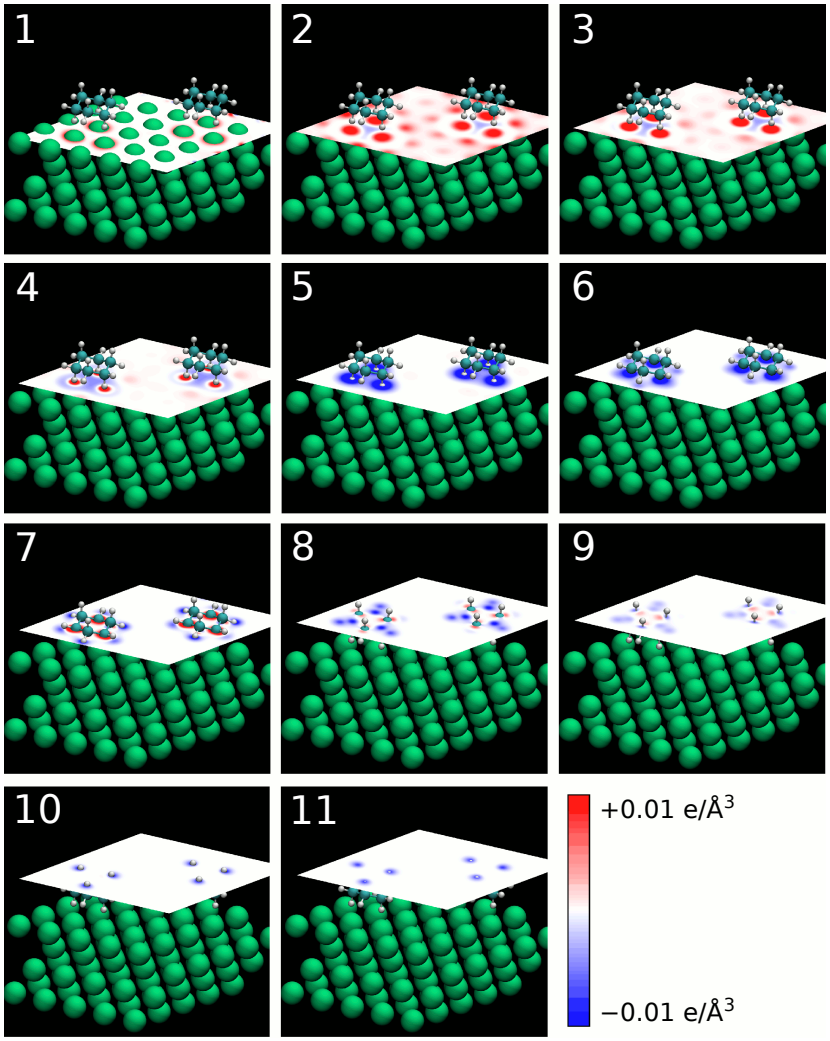

Figure B.3: Difference between the electron density of a surface with molecules adsorbed and the sum of isolated surface and isolated molecules, shown at different $x-y$ slices along z coordinate. Red color denotes electron density accumulation, and blue denotes depletion.

Appendix C

Supplementing details for Chapter 5

C.1 Availability of data

Phonon calculations for the initial and transition states of water splitting reaction, and the geometry relaxations of the adsorbed reactants and products for different values of an electric field are uploaded to the NOMAD repository, the dataset DOI is 10.17172/NOMAD/2022.09.15-1.

C.2 Water dissociation paths with non-zero electric fields

Dissociation paths for –0.74 and +0.74 V/Å are shown in figures C.1 (a) and (b), respectively. Despite different reactant geometries, the transition states of the reaction are quite similar.

C.3 Including lateral interaction: a water dimer

We simulated a water dimer to include water-water interactions, which are known to have decisive impact on the structure of the interface layer of water [192, 27]. We found that even one neighboring molecule is enough to prevent the flip of adsorbed

a)

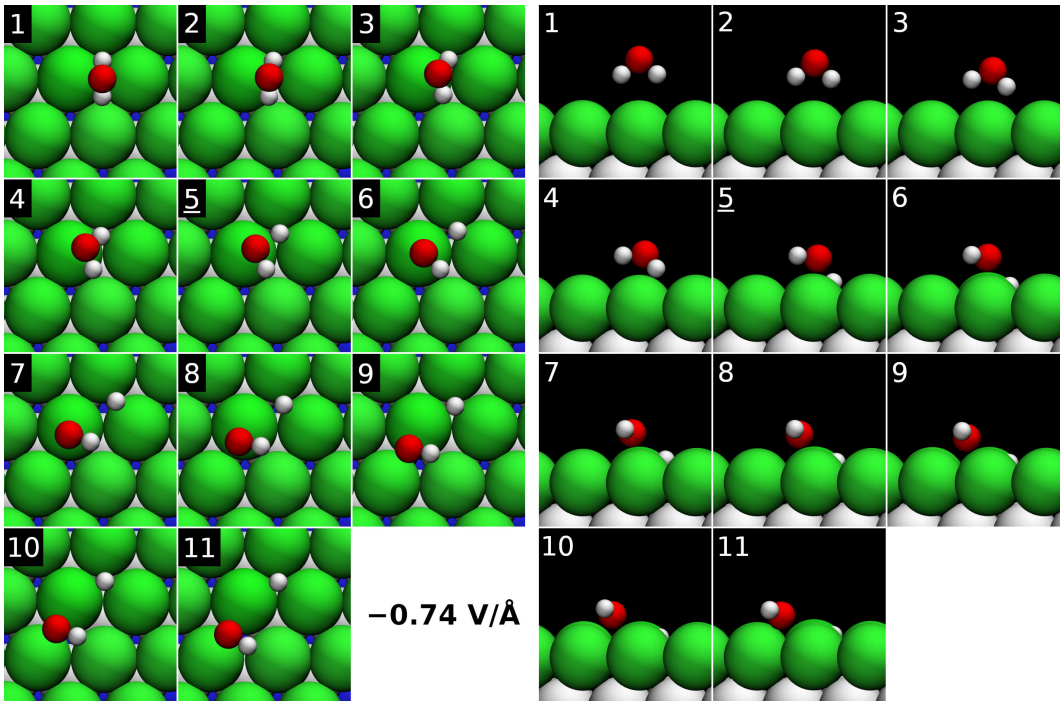

b)

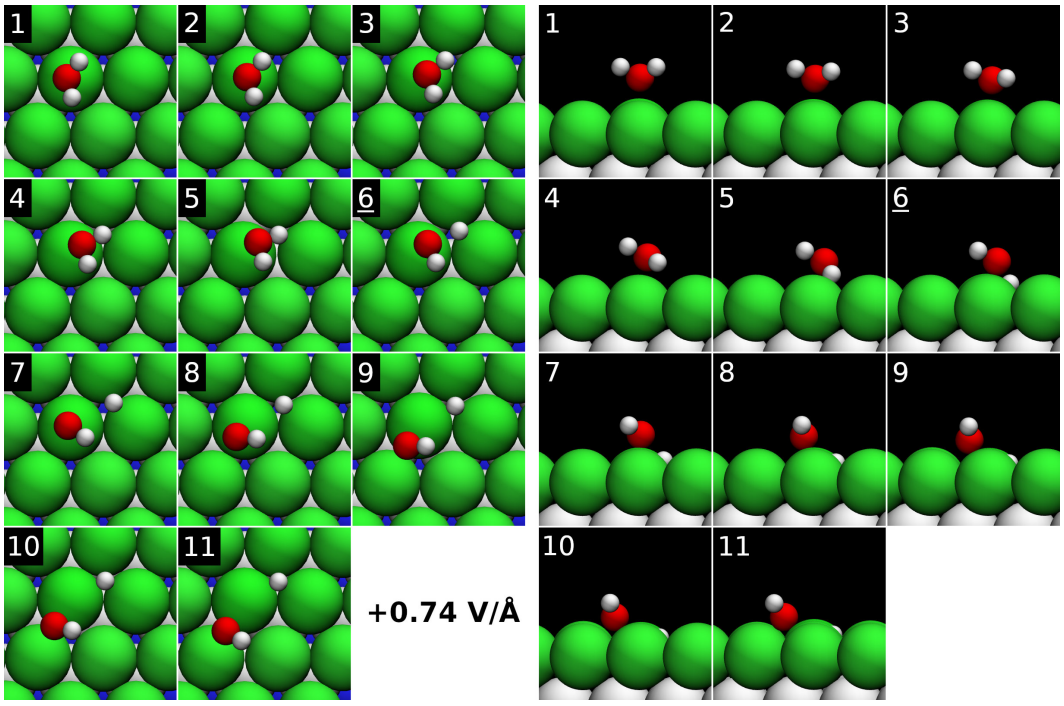

Figure C.1: Reaction path of water molecule splitting on the Pd(111) surface at –0.74 V/Å (a) and +0.74 V/Å (b), individual NEB beads. Large green, and white spheres denote the 1st and the 2nd layers of the Pd(111) surface, respectively. The underlined frame index denotes the transition state.

configuration which happened for the monomer below –0.3 V/Å. In a dimer, the water molecules form a hydrogen bond strong enough to prevent sharp changes in the range of –0.74..+0.74 V/Å (see fig. C.2). At the same time, two competing adsorbed structures were found for zero electric field. We tried to simulate the reaction

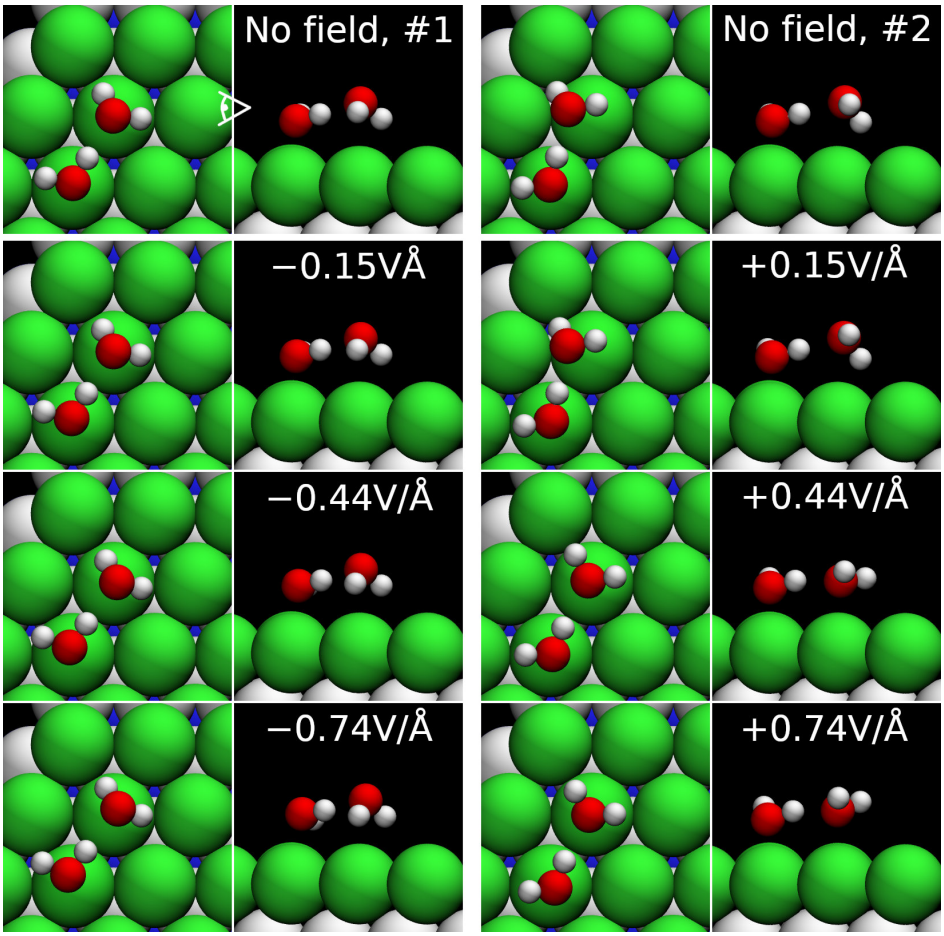

Figure C.2: Water dimer adsorbed on a Pd(111) surface under different electric field values. Large green, white and blue spheres denote the 1st, 2nd and 3rd layers of the Pd(111) surface, respectively. Structure #1 is 7 meV more preferable than #2.

$$2H_2O \rightarrow H_2O + OH + H. \tag{C.1}$$

We tried to perform NEB optimization for this reaction following the same CI-NEB protocol as for the monomer. For all bias values we managed to converge the NEB path down to the force residue of 0.05 eV/Å. The path without an electric field is shown in figure C.3). However, we were unable neither to converge it further, nor to perform

climbing-image optimization from these reasonably-well converged geometries because our NEB implementation started to diverge, and climbing algorithm also fails to refine the position of the saddle point and drifts away from the path.

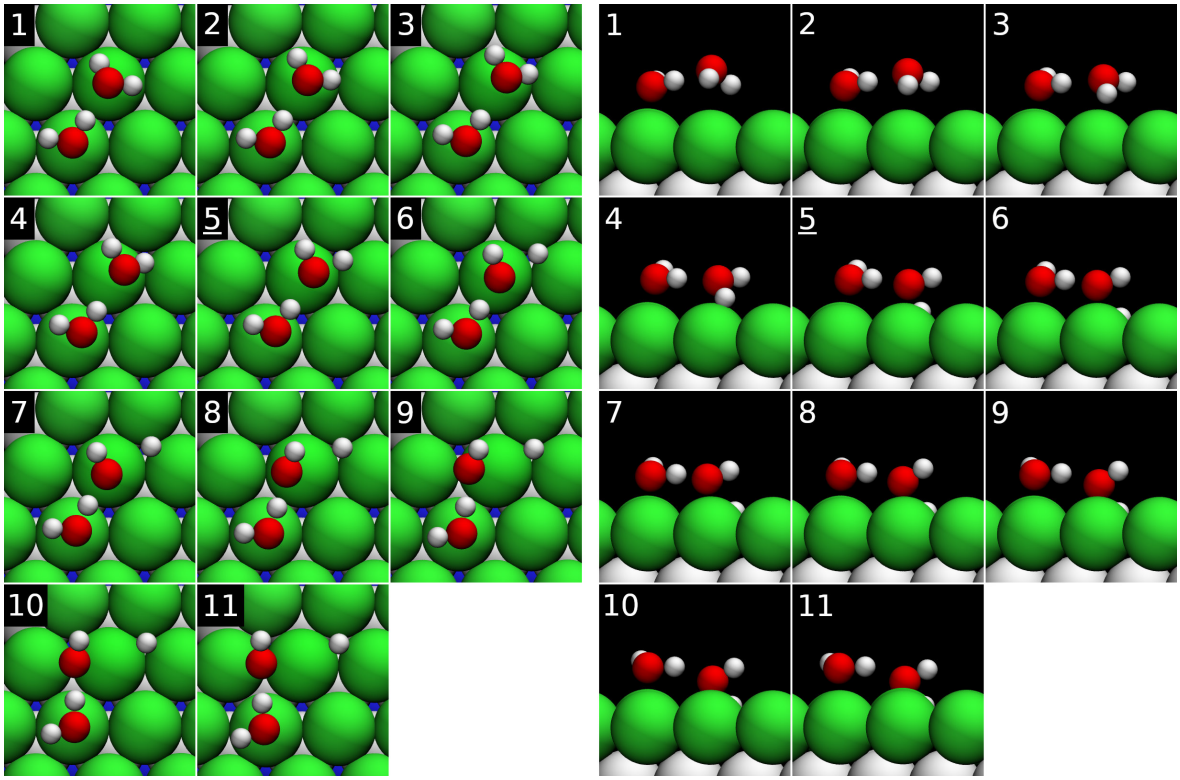

Figure C.3: The best reaction path that we achieved by the NEB algorithm for the dissociation of a water dimer on the Pd(111) surface without electric field applied. Individual NEB beads are shown. Bead 5 is the closest to the transition state. Large green, white and blue spheres denote the 1st, 2nd and 3rd layers of the Pd(111) surface, respectively.

C.4 Calculations of electronic Green's functions

Attempting to go beyond the slab model, we tested two implementations of electronic Green's functions: SMEAGOL and TranSIESTA, both based on the SIESTA DFT code. SMEAGOL currently supports the 2-electrode setup shown in fig. 2.5, and TranSIESTA suppors both 1 and 2-electrode setups. As described in section 2.6.3, sub-surface bulk metal is modelled as infinite repetitions of a principal layer (PL),

which is thick enough to screen the interactions to the second-nearest neighboring layer completely.

In 2-electrode setup, additional periodicity requirement takes place, because Poisson solver and energy functional in SMEAGOL are taken from SIESTA with minor modifications only. An FCC(111) slab is 3-periodic (ABC layers), therefore a PL should have 3 or 6 atomic layers. The cell contains a PL on each side, plus a number of surface layers sufficient to screen the PLs from vacuum. In the published work of our colleagues, gold surface was simulated. For gold, an ABC layer has length of 7.704 Å, and double-zeta basis set that was employed has a cut-off at 3.385 Å, which means that the electronic densities of the second-nearest neighbors do not overlap. This rather coincidental fact allows using a single ABC layer as a PL. For palladium, the lattice vector is smaller and an ABC layer spans over 6.797 Å only. At the same time, the necessary basis set is more extended than that of gold: we worked with two slightly different DZP basis sets with the cut-off distances of 4.454 and 4.170 Å. It means that the densities of the second-nearest neighbors will interact if the 3-layer is used as a PL, therefore a 6-layer is needed. This fact increases a system size considerably: considering that at least 4×4 lateral dimensions are necessary to damp water self interaction across x, y boundaries and 3-4 layers in z direction are needed to screen the PLs, the total number of atoms in such a setup is close to 300 (see fig. C.4. Converging the SCF cycle for a thick metal

Figure C.4: Typical dimensions of a 2-electrode setup in SMEAGOL or TranSIESTA with 6 atomic layers in a principal layer.

slab is difficult even in canonical KS-DFT [212], and fluctuating number of electrons makes this task even harder [4]. To date, SMEAGOL does not offer mixing procedures tailored for grand-canonical calculations, and we didn't manage to converge any GF calculation.

We then tried both 1 and 2-electrode setups available in TranSIESTA, and managed

to converge a single point for zero bias, starting from the density converged by KS-DFT in SIESTA. The reason for success is that converged KS-DFT is a very good initial guess, since the ground state density does not depend on the method which is used to calculate it. However, the density update algorithm appeared to be very unstable and diverged after either the atoms were displaced or a potential bias was required.

Bibliography

[1] Jörg Neugebauer and Matthias Scheffler, *Adsorbate-substrate and adsorbate-adsorbate interactions of Na and K adlayers on Al(111)*, Phys. Rev. B **46** (1992), 16067–16080.

[2] Thomas Dufils, Guillaume Jeanmairet, Benjamin Rotenberg, Michiel Sprik, and Mathieu Salanne, *Simulating electrochemical systems by combining the finite field method with a constant potential electrode*, Phys. Rev. Lett. **123** (2019), 195501.

[3] Nicéphore Bonnet, Tetsuya Morishita, Osamu Sugino, and Minoru Otani, *First-principles molecular dynamics at a constant electrode potential*, Phys. Rev. Lett. **109** (2012), 266101.

[4] Ravishankar Sundararaman, William A. Goddard, and Tomas A. Arias, *Grand canonical electronic density-functional theory: Algorithms and applications to electrochemistry*, The Journal of Chemical Physics **146** (2017), no. 11, 114104.

[5] Satoshi Hagiwara, Chunping Hu, Satomichi Nishihara, and Minoru Otani, *Bias-dependent diffusion of a H_2O molecule on metal surfaces by the first-principles method under the grand-canonical ensemble*, Phys. Rev. Materials **5** (2021), 065001.

[6] Klaus Müller and Leo D. Brown, *Location of saddle points and minimum energy paths by a constrained simplex optimization procedure*, Theoretica chimica acta **53** (1979), no. 1, 75–93.

[7] Karen Fidanyan, Ikutaro Hamada, and Mariana Rossi, *Quantum nuclei at weakly bonded interfaces: The case of cyclohexane on Rh(111)*, Advanced Theory and Simulations **4** (2021), no. 4, 2000241.

[8] Takanori Koitaya, Sumera Shimizu, Kozo Mukai, Shinya Yoshimoto, and Jun Yoshinobu, *Kinetic and geometric isotope effects originating from different adsorption potential energy surfaces: Cyclohexane on Rh(111)*, The Journal of Chemical Physics **136** (2012), no. 21, 214705.

[9] Javier Carrasco, Angelos Michaelides, and Matthias Scheffler, *Insight from first principles into the nature of the bonding between water molecules and 4d metal surfaces*, The Journal of Chemical Physics **130** (2009), no. 18, 184707.

[10] Victor G. Ruiz, Wei Liu, Egbert Zojer, Matthias Scheffler, and Alexandre Tkatchenko, *Density-functional theory with screened van der Waals interactions for the modeling of hybrid inorganic-organic systems*, Phys. Rev. Lett. **108** (2012), 146103.

[11] Dang Sheng Su, Jian Zhang, Benjamin Frank, Arne Thomas, Xinchen Wang, Jens Paraknowitsch, and Robert Schlögl, *Metal-free heterogeneous catalysis for sustainable chemistry*, ChemSusChem: Chemistry & Sustainability Energy & Materials **3** (2010), no. 2, 169–180.

[12] Robert Schlögl, *Heterogeneous catalysis*, Angewandte Chemie International Edition **54** (2015), no. 11, 3465–3520.

[13] Norbert Koch, *Organic electronic devices and their functional interfaces*, ChemPhysChem **8** (2007), no. 10, 1438–1455.

[14] Hisao Ishii, Kiyoshi Sugiyama, Eisuke Ito, and Kazuhiko Seki, *Energy level alignment and interfacial electronic structures at organic/metal and organic/organic interfaces*, Advanced Materials **11** (1999), no. 8, 605–625.

[15] Gregor Witte, Simon Lukas, Paul S Bagus, and Christof Wöll, *Vacuum level alignment at organic/metal junctions:"Cushion" effect and the interface dipole*, Applied Physics Letters **87** (2005), no. 26, 263502.

[16] R. Burch, P. K. Loader, and F. J. Urbano, *Some aspects of hydrocarbon activation on platinum group metal combustion catalysts*, Catalysis Today **27** (1996), no. 1,

243–248, 1st World Conference Environmental Catalysis For a Better World and Life.

[17] Junbo Hou, Min Yang, Changchun Ke, Guanghua Wei, Cameron Priest, Zhi Qiao, Gang Wu, and Junliang Zhang, *Platinum-group-metal catalysts for proton exchange membrane fuel cells: From catalyst design to electrode structure optimization*, EnergyChem **2** (2020), no. 1, 100023.

[18] Anthony E. Hughes, Nawshad Haque, Stephen A. Northey, and Sarbjit Giddey, *Platinum group metals: A review of resources, production and usage with a focus on catalysts*, Resources **10** (2021), no. 9.

[19] Q. Du, R. Superfine, E. Freysz, and Y. R. Shen, *Vibrational spectroscopy of water at the vapor/water interface*, Phys. Rev. Lett. **70** (1993), 2313–2316.

[20] N. Bloembergen, *Surface nonlinear optics: a historical overview*, Applied Physics B **68** (1999), no. 3, 289–293.

[21] Akihiro Morita, *Theory of sum frequency generation spectroscopy*, vol. 97, Springer, 2018.

[22] Gerhard Ertl and Jürgen Küppers, *Low energy electrons and surface chemistry*, vol. 87, Vch Weinheim, 1985.

[23] P. Stoltze and J. K. Nørskov, *Bridging the "pressure gap" between ultrahigh-vacuum surface physics and high-pressure catalysis*, Phys. Rev. Lett. **55** (1985), 2502–2505.

[24] D. C. Koningsberger and R. Prins, *X-ray absorption: principles, applications, techniques of EXAFS, SEXAFS and XANES*, Chemical analysis **92** (1988).

[25] G. Lüpke, *Characterization of semiconductor interfaces by second-harmonic generation*, Surface Science Reports **35** (1999), no. 3, 75–161.

[26] Yuanyuan Zhou, Matthias Scheffler, and Luca M. Ghiringhelli, *Determining surface phase diagrams including anharmonic effects*, Phys. Rev. B **100** (2019), 174106.

[27] Luana S. Pedroza, Adrien Poissier, and M.-V. Fernández-Serra, *Local order of liquid water at metallic electrode surfaces*, The Journal of Chemical Physics **142** (2015), no. 3, 034706.

[28] Jinggang Lan, Vladimir V. Rybkin, and Marcella Iannuzzi, *Ionization of water as an effect of quantum delocalization at aqueous electrode interfaces*, The Journal of Physical Chemistry Letters **11** (2020), no. 9, 3724–3730, PMID: 32315196.

[29] Zdenek Futera and Niall J. English, *Water breakup at Fe2O3–hematite/water interfaces: Influence of external electric fields from nonequilibrium ab initio molecular dynamics*, The Journal of Physical Chemistry Letters **12** (2021), no. 29, 6818–6826, PMID: 34270253.

[30] Takanori Koitaya, Kozo Mukai, Shinya Yoshimoto, and Jun Yoshinobu, *Two-dimensional superstructures and softened C–H stretching vibrations of cyclohexane on Rh(111): Effects of preadsorbed hydrogen*, The Journal of Chemical Physics **135** (2011), no. 23, 234704.

[31] Aliaksandr V. Krukau, Oleg A. Vydrov, Artur F. Izmaylov, and Gustavo E. Scuseria, *Influence of the exchange screening parameter on the performance of screened hybrid functionals*, The Journal of Chemical Physics **125** (2006), no. 22, 224106.

[32] Soohyung Park, Haiyuan Wang, Thorsten Schultz, Dongguen Shin, Ruslan Ovsyannikov, Marios Zacharias, Dmitrii Maksimov, Matthias Meissner, Yuri Hasegawa, Takuma Yamaguchi, et al., *Temperature-dependent electronic ground-state charge transfer in van der Waals heterostructures*, Advanced Materials **33** (2021), no. 29, 2008677.

[33] M. Otani and O. Sugino, *First-principles calculations of charged surfaces and interfaces: A plane-wave nonrepeated slab approach*, Phys. Rev. B **73** (2006), 115407.

[34] Sudarsan Surendralal, Mira Todorova, Michael W. Finnis, and Jörg Neugebauer, *First-principles approach to model electrochemical reactions: Understanding the*

fundamental mechanisms behind Mg corrosion, Phys. Rev. Lett. **120** (2018), 246801.

[35] F. Deißenbeck, C. Freysoldt, M. Todorova, J. Neugebauer, and S. Wippermann, *Dielectric properties of nanoconfined water: A canonical thermopotentiostat approach*, Phys. Rev. Lett. **126** (2021), 136803.

[36] Volker Blum, Ralf Gehrke, Felix Hanke, Paula Havu, Ville Havu, Xinguo Ren, Karsten Reuter, and Matthias Scheffler, *Ab initio molecular simulations with numeric atom-centered orbitals*, Computer Physics Communications **180** (2009), no. 11, 2175 – 2196.

[37] José M. Soler, Emilio Artacho, Julian D. Gale, Alberto García, Javier Junquera, Pablo Ordejón, and Daniel Sánchez-Portal, *The SIESTA method for ab initio order-N materials simulation*, Journal of Physics: Condensed Matter **14** (2002), no. 11, 2745–2779.

[38] Alberto García, Nick Papior, Arsalan Akhtar, Emilio Artacho, Volker Blum, Emanuele Bosoni, Pedro Brandimarte, Mads Brandbyge, J. I. Cerdá, Fabiano Corsetti, Ramón Cuadrado, Vladimir Dikan, Jaime Ferrer, Julian Gale, Pablo García-Fernández, V. M. García-Suárez, Sandra García, Georg Huhs, Sergio Illera, Richard Korytár, Peter Koval, Irina Lebedeva, Lin Lin, Pablo López-Tarifa, Sara G. Mayo, Stephan Mohr, Pablo Ordejón, Andrei Postnikov, Yann Pouillon, Miguel Pruneda, Roberto Robles, Daniel Sánchez-Portal, Jose M. Soler, Rafi Ullah, Victor Wen-zhe Yu, and Javier Junquera, *Siesta: Recent developments and applications*, The Journal of Chemical Physics **152** (2020), no. 20, 204108.

[39] S. Sanvito, C. J. Lambert, J. H. Jefferson, and A. M. Bratkovsky, *General Green's-function formalism for transport calculations with* spd *hamiltonians and giant magnetoresistance in co- and ni-based magnetic multilayers*, Phys. Rev. B **59** (1999), 11936–11948.

[40] J. E. Inglesfield, *From slabs to surfaces – calculating the electronic structure of a semi-infinite solid*, Progress in surface science **25** (1987), no. 1-4, 57–82.

[41] J. E. Inglesfield, *The screening of an electric field at an Al(001) surface*, Surface Science **188** (1987), no. 3, L701–L707.

[42] G. C. Aers and J. E. Inglesfield, *Electric field and Ag(001) surface electronic structure*, Surface Science **217** (1989), no. 1, 367–383.

[43] Matthias Scheffler, Ch. Droste, Andrzej Fleszar, F. Maca, G. Wachutka, and G. Barzel, *A self-consistent surface-Green-function (SSGF) method*, Physica B: Condensed Matter **172** (1991), no. 1-2, 143–153.

[44] Nick Papior, Nicolás Lorente, Thomas Frederiksen, Alberto García, and Mads Brandbyge, *Improvements on non-equilibrium and transport Green function techniques: The next-generation transiesta*, Computer Physics Communications **212** (2017), 8–24.

[45] Søren Smidstrup, Troels Markussen, Pieter Vancraeyveld, Jess Wellendorff, Julian Schneider, Tue Gunst, Brecht Verstichel, Daniele Stradi, Petr A. Khomyakov, Ulrik G. Vej-Hansen, Maeng-Eun Lee, Samuel T. Chill, Filip Rasmussen, Gabriele Penazzi, Fabiano Corsetti, Ari Ojanperä, Kristian Jensen, Mattias L. N. Palsgaard, Umberto Martinez, Anders Blom, Mads Brandbyge, and Kurt Stokbro, *QuantumATK: an integrated platform of electronic and atomic-scale modelling tools*, Journal of Physics: Condensed Matter **32** (2019), no. 1, 015901.

[46] D. Wortmann, H. Ishida, and S. Blügel, *Ab initio Green-function formulation of the transfer matrix: Application to complex band structures*, Phys. Rev. B **65** (2002), 165103.

[47] Kurt Stokbro, Jeremy Taylor, Mads Brandbyge, and Pablo Ordejón, *TranSIESTA: A spice for molecular electronics*, Annals of the New York Academy of Sciences **1006** (2003), no. 1, 212–226.

[48] A. R. Rocha and S. Sanvito, *Asymmetric $i-v$ characteristics and magnetoresistance in magnetic point contacts*, Phys. Rev. B **70** (2004), 094406.

[49] Henry Eyring, *The activated complex in chemical reactions*, The Journal of Chemical Physics **3** (1935), no. 2, 107–115.

[50] Henry Eyring, *The theory of absolute reaction rates*, Trans. Faraday Soc. **34** (1938), 41–48.

[51] George H. Vineyard, *Frequency factors and isotope effects in solid state rate processes*, Journal of Physics and Chemistry of Solids **3** (1957), no. 1-2, 121–127.

[52] Atsushi Togo, Laurent Chaput, and Isao Tanaka, *Distributions of phonon lifetimes in brillouin zones*, Phys. Rev. B **91** (2015), 094306.

[53] Olle Hellman, Peter Steneteg, I. A. Abrikosov, and S. I. Simak, *Temperature dependent effective potential method for accurate free energy calculations of solids*, Phys. Rev. B **87** (2013), 104111.

[54] Olle Hellman and Igor A. Abrikosov, *Temperature-dependent effective third-order interatomic force constants from first principles*, Physical Review B **88** (2013), no. 14, 144301.

[55] H. Okamoto, *The Ru-Zr system (ruthenium-zirconium)*, Journal of phase equilibria **14** (1993), no. 2, 225–227.

[56] Choong-Shik Yoo, Hyunchae Cynn, and Per Söderlind, *Phase diagram of uranium at high pressures and temperatures*, Physical Review B **57** (1998), no. 17, 10359.

[57] Mariana Rossi, Piero Gasparotto, and Michele Ceriotti, *Anharmonic and quantum fluctuations in molecular crystals: A first-principles study of the stability of paracetamol*, Phys. Rev. Lett. **117** (2016), 115702.

[58] Shuyi Liu, D. Baugh, Kenta Motobayashi, Xunhua Zhao, Sergey V. Levchenko, Sylwester Gawinkowski, Jacek Waluk, Leonhard Grill, Mats Persson, and Takashi Kumagai, *Anharmonicity in a double hydrogen transfer reaction studied in a single porphycene molecule on a Cu (110) surface*, Physical Chemistry Chemical Physics **20** (2018), no. 17, 12112–12119.

[59] Matheus Jacobs, Jannis Krumland, Ana M. Valencia, Haiyuan Wang, Mariana Rossi, and Caterina Cocchi, *Ultrafast charge transfer and vibronic coupling in a laser-excited hybrid inorganic/organic interface*, Advances in Physics: X **5** (2020), no. 1, 1749883.

[60] Honghui Shang and Haidi Wang, *Anharmonic Raman spectra simulation of crystals from deep neural networks*, AIP Advances **11** (2021), no. 3, 035105.

[61] Tushar Debnath, Debalaya Sarker, He Huang, Zhong-Kang Han, Amrita Dey, Lakshminarayana Polavarapu, Sergey V. Levchenko, and Jochen Feldmann, *Coherent vibrational dynamics reveals lattice anharmonicity in organic–inorganic halide perovskite nanocrystals*, Nature communications **12** (2021), no. 1, 1–9.

[62] Leeor Kronik and Alexandre Tkatchenko, *Understanding molecular crystals with dispersion-inclusive density functional theory: Pairwise corrections and beyond*, Accounts of Chemical Research **47** (2014), no. 11, 3208–3216.

[63] Fritz London, *The general theory of molecular forces*, Trans. Faraday Soc. **33** (1937), 8b–26.

[64] Alexandre Tkatchenko and Matthias Scheffler, *Accurate molecular van der Waals interactions from ground-state electron density and free-atom reference data*, Phys. Rev. Lett. **102** (2009), 073005.

[65] M. Dion, H. Rydberg, E. Schröder, D. C. Langreth, and B. I. Lundqvist, *Van der Waals density functional for general geometries*, Phys. Rev. Lett. **92** (2004), 246401.

[66] Kyuho Lee, Éamonn D. Murray, Lingzhu Kong, Bengt I. Lundqvist, and David C. Langreth, *Higher-accuracy van der Waals density functional*, Phys. Rev. B **82** (2010), 081101.

[67] Jan Hermann and Alexandre Tkatchenko, *Density functional model for van der Waals interactions: Unifying many-body atomic approaches with nonlocal functionals*, Phys. Rev. Lett. **124** (2020), 146401.

[68] Alessandro Laio and Michele Parrinello, *Escaping free-energy minima*, Proceedings of the National Academy of Sciences **99** (2002), no. 20, 12562–12566.

[69] Robert H. Swendsen and Jian-Sheng Wang, *Replica Monte Carlo simulation of spin-glasses*, Physical review letters **57** (1986), no. 21, 2607.

[70] Cameron Abrams and Giovanni Bussi, *Enhanced sampling in molecular dynamics using metadynamics, replica-exchange, and temperature-acceleration*, Entropy **16** (2014), no. 1, 163–199.

[71] Yi Isaac Yang, Qiang Shao, Jun Zhang, Lijiang Yang, and Yi Qin Gao, *Enhanced sampling in molecular dynamics*, The Journal of chemical physics **151** (2019), no. 7, 070902.

[72] Michele Parrinello and Aneesur Rahman, *Study of an F center in molten KCl*, The Journal of Chemical Physics **80** (1984), no. 2, 860–867.

[73] Dominik Marx and Michele Parrinello, *Ab initio path integral molecular dynamics: Basic ideas*, The Journal of chemical physics **104** (1996), no. 11, 4077–4082.

[74] Motoyuki Shiga, Masanori Tachikawa, and Shinichi Miura, *Ab initio molecular orbital calculation considering the quantum mechanical effect of nuclei by path integral molecular dynamics*, Chemical Physics Letters **332** (2000), no. 3-4, 396–402.

[75] Michele Ceriotti, Joshua More, and David E. Manolopoulos, *i-PI: A Python interface for ab initio path integral molecular dynamics simulations*, Computer Physics Communications **185** (2014), no. 3, 1019–1026.

[76] Venkat Kapil, Mariana Rossi, Ondrej Marsalek, Riccardo Petraglia, Yair Litman, Thomas Spura, Bingqing Cheng, Alice Cuzzocrea, Robert H. Meißner, David M. Wilkins, Benjamin A. Helfrecht, Przemysław Juda, Sébastien P. Bienvenue, Wei Fang, Jan Kessler, Igor Poltavsky, Steven Vandenbrande, Jelle Wieme, Clemence Corminboeuf, Thomas D. Kühne, David E. Manolopoulos, Thomas E. Markland, Jeremy O. Richardson, Alexandre Tkatchenko, Gareth A. Tribello, Veronique Van Speybroeck, and Michele Ceriotti, *i-PI 2.0: A universal force engine for advanced molecular simulations*, Computer Physics Communications **236** (2019), 214 – 223.

[77] John P. Perdew and Karla Schmidt, *Jacob's ladder of density functional approximations for the exchange-correlation energy*, AIP Conference Proceedings **577** (2001), no. 1, 1–20.

[78] Jay A. Labinger and John E. Bercaw, *Understanding and exploiting C–H bond activation*, Nature **417** (2002), no. 6888, 507–514.

[79] Gang Chen, Lev N. Zakharov, Mark E. Bowden, Abhijeet J. Karkamkar, Sean M. Whittemore, Edward B. Garner, Tanya C. Mikulas, David A. Dixon, Tom Autrey, and Shih-Yuan Liu, *Bis-BN cyclohexane: A remarkably kinetically stable chemical hydrogen storage material*, Journal of the American Chemical Society **137** (2015), no. 1, 134–137.

[80] Lu Li, Xiaoyue Mu, Wenbo Liu, Zetian Mi, and Chao-Jun Li, *Simple and efficient system for combined solar energy harvesting and reversible hydrogen storage*, Journal of the American Chemical Society **137** (2015), no. 24, 7576–7579.

[81] M. Born and R. Oppenheimer, *Zur Quantentheorie der Molekeln*, Annalen der Physik **389** (1927), no. 20, 457–484.

[82] Jerzy Leszczynski, *Handbook of computational chemistry*, Springer Science & Business Media, 2012.

[83] P. Hohenberg and W. Kohn, *Inhomogeneous electron gas*, Phys. Rev. **136** (1964), B864–B871.

[84] Walter Kohn and Lu Jeu Sham, *Self-consistent equations including exchange and correlation effects*, Physical review **140** (1965), no. 4A, A1133.

[85] Robert G. Parr and Yang Weitao, *Density-Functional Theory of Atoms and Molecules*, Oxford University Press, 01 1995.

[86] John P. Perdew, Kieron Burke, and Matthias Ernzerhof, *Generalized gradient approximation made simple*, Phys. Rev. Lett. **77** (1996), 3865–3868.

[87] Mel Levy, *Asymptotic coordinate scaling bound for exchange-correlation energy in density-functional theory*, International Journal of Quantum Chemistry **36** (1989), no. S23, 617–619.

[88] Yingkai Zhang and Weitao Yang, *A challenge for density functionals: Self-interaction error increases for systems with a noninteger number of electrons*, The Journal of chemical physics **109** (1998), no. 7, 2604–2608.

[89] Paula Mori-Sánchez, Aron J. Cohen, and Weitao Yang, *Many-electron self-interaction error in approximate density functionals*, The Journal of chemical physics **125** (2006), no. 20, 201102.

[90] John P. Perdew, Matthias Ernzerhof, and Kieron Burke, *Rationale for mixing exact exchange with density functional approximations*, The Journal of Chemical Physics **105** (1996), no. 22, 9982–9985.

[91] Carlo Adamo and Vincenzo Barone, *Toward reliable density functional methods without adjustable parameters: The PBE0 model*, The Journal of Chemical Physics **110** (1999), no. 13, 6158–6170.

[92] Matthias Ernzerhof and Gustavo E. Scuseria, *Assessment of the Perdew–Burke–Ernzerhof exchange-correlation functional*, The Journal of chemical physics **110** (1999), no. 11, 5029–5036.

[93] Carlo Adamo and Vincenzo Barone, *Physically motivated density functionals with improved performances: The modified Perdew–Burke–Ernzerhof model*, The Journal of Chemical Physics **116** (2002), no. 14, 5933–5940.

[94] Philipp Haas, Fabien Tran, and Peter Blaha, *Calculation of the lattice constant of solids with semilocal functionals*, Phys. Rev. B **79** (2009), 085104.

[95] Guo-Xu Zhang, Anthony M. Reilly, Alexandre Tkatchenko, and Matthias Scheffler, *Performance of various density-functional approximations for cohesive properties of 64 bulk solids*, New Journal of Physics **20** (2018), no. 6, 063020.

[96] Michael J. Gillan, Dario Alfè, and Angelos Michaelides, *Perspective: How good is DFT for water?*, The Journal of Chemical Physics **144** (2016), no. 13, 130901.

[97] J. D. Van der Waals, *On the continuity of the gaseous and liquid states*, Doctoral Dissertation, Leiben (1873).

[98] John E. Lennard-Jones, *Cohesion*, Proceedings of the Physical Society (1926-1948) **43** (1931), no. 5, 461.

[99] John Edward Jones, *On the determination of molecular fields. I. From the variation of the viscosity of a gas with temperature*, Proceedings of the Royal Society of London. Series A, Containing Papers of a Mathematical and Physical Character **106** (1924), no. 738, 441–462.

[100] Hendrik B. G. Casimir and Dirk Polder, *The influence of retardation on the London-van der Waals forces*, Physical Review **73** (1948), no. 4, 360.

[101] Lev D. Landau and Evgeny M. Lifshitz, *Statistical Physics, Part 1 (Third Edition)*, 3 ed., vol. 5, Butterworth-Heinemann, 1980.

[102] Evgeny M. Lifshitz, *The theory of molecular attractive forces between solids*, Soviet Phys. JETP **2** (1956), no. 1.

[103] Eugene Zaremba and Walter Kohn, *Van der Waals interaction between an atom and a solid surface*, Physical Review B **13** (1976), no. 6, 2270.

[104] Albrecht Unsöld, *Quantentheorie des Wasserstoffmolekülions und der Born-Landéschen Abstoßungskräfte*, Zeitschrift für Physik **43** (1927), no. 8, 563–574.

[105] K. T. Tang and M. Karplus, *Padé-approximant calculation of the nonretarded van der waals coefficients for two and three helium atoms*, Physical Review **171** (1968), no. 1, 70.

[106] Fred L. Hirshfeld, *Bonded-atom fragments for describing molecular charge densities*, Theoretica chimica acta **44** (1977), no. 2, 129–138.

[107] Tore Brinck, Jane S. Murray, and Peter Politzer, *Polarizability and volume*, The Journal of chemical physics **98** (1993), no. 5, 4305–4306.

[108] Juan J. Perez and Hugo O. Villar, *Computation of the polarizability of anthracene*, Chemical Physics Letters **188** (1992), no. 5, 604–608.

[109] G. Mercurio, E. R. McNellis, I. Martin, S. Hagen, F. Leyssner, S. Soubatch, J. Meyer, M. Wolf, P. Tegeder, F. S. Tautz, and K. Reuter, *Structure and energetics of azobenzene on Ag(111): Benchmarking semiempirical dispersion correction approaches*, Phys. Rev. Lett. **104** (2010), 036102.

[110] Victor G. Ruiz, Wei Liu, and Alexandre Tkatchenko, *Density-functional theory with screened van der Waals interactions applied to atomic and molecular adsorbates on close-packed and non-close-packed surfaces*, Phys. Rev. B **93** (2016), 035118.

[111] Alexandre Tkatchenko, Robert A. DiStasio, Roberto Car, and Matthias Scheffler, *Accurate and efficient method for many-body van der Waals interactions*, Phys. Rev. Lett. **108** (2012), 236402.

[112] A. Mayer, *Formulation in terms of normalized propagators of a charge-dipole model enabling the calculation of the polarization properties of fullerenes and carbon nanotubes*, Phys. Rev. B **75** (2007), 045407.

[113] A. Mayer and P.-O. Åstrand, *A charge–dipole model for the static polarizability of nanostructures including aliphatic, olephinic, and aromatic systems*, The Journal of Physical Chemistry A **112** (2008), no. 6, 1277–1285, PMID: 18198848.

[114] Alberto Ambrosetti, Anthony M. Reilly, Robert A. DiStasio, and Alexandre Tkatchenko, *Long-range correlation energy calculated from coupled atomic response functions*, The Journal of Chemical Physics **140** (2014), no. 18, 18A508.

[115] Tomáš Bučko, Sébastien Lebègue, Tim Gould, and János G. Ángyán, *Many-body dispersion corrections for periodic systems: an efficient reciprocal space implementation*, Journal of Physics: Condensed Matter **28** (2016), no. 4, 045201.

[116] Oleg A. Vydrov and Troy Van Voorhis, *Dispersion interactions from a local polarizability model*, Phys. Rev. A **81** (2010), 062708.

[117] Tim Gould, Sébastien Lebègue, János G. Ángyán, and Tomáš Bučko, *A fractionally ionic approach to polarizability and van der Waals many-body dispersion calculations*, Journal of Chemical Theory and Computation **12** (2016), no. 12, 5920–5930, PMID: 27951673.

[118] Oliver T. Hofmann, Egbert Zojer, Lukas Hörmann, Andreas Jeindl, and Reinhard J. Maurer, *First-principles calculations of hybrid inorganic–organic inter-*

faces: from state-of-the-art to best practice, Physical Chemistry Chemical Physics **23** (2021), no. 14, 8132–8180.

[119] Ikutaro Hamada, Minoru Otani, Osamu Sugino, and Yoshitada Morikawa, *Green's function method for elimination of the spurious multipole interaction in the surface/interface slab model*, Phys. Rev. B **80** (2009), 165411.

[120] Ikutaro Hamada, Osamu Sugino, Nicéphore Bonnet, and Minoru Otani, *Improved modeling of electrified interfaces using the effective screening medium method*, Phys. Rev. B **88** (2013), 155427.

[121] Leonid V. Keldysh, *Diagram technique for nonequilibrium processes*, Sov. Phys. JETP **20** (1965), no. 4, 1018–1026.

[122] Pablo Ordejón, Emilio Artacho, and José M. Soler, *Self-consistent order-n density-functional calculations for very large systems*, Phys. Rev. B **53** (1996), R10441–R10444.

[123] Richard T. Hall and Jerome M. Dowling, *Pure rotational spectrum of water vapor*, The Journal of Chemical Physics **47** (1967), no. 7, 2454–2461.

[124] Thomas Kreibich, Robert van Leeuwen, and E. K. U. Gross, *Multicomponent density-functional theory for electrons and nuclei*, Phys. Rev. A **78** (2008), 022501.

[125] Kurt R. Brorsen, Patrick E. Schneider, and Sharon Hammes-Schiffer, *Alternative forms and transferability of electron-proton correlation functionals in nuclear-electronic orbital density functional theory*, The Journal of Chemical Physics **149** (2018), no. 4, 044110.

[126] Hale F. Trotter, *On the product of semi-groups of operators*, Proceedings of the American Mathematical Society **10** (1959), no. 4, 545–551.

[127] Mark Tuckerman, *Statistical mechanics: theory and molecular simulation*, Oxford university press, 2010.

[128] David Chandler and Peter G. Wolynes, *Exploiting the isomorphism between quantum theory and classical statistical mechanics of polyatomic fluids*, The Journal of Chemical Physics **74** (1981), no. 7, 4078–4095.

[129] R. P. Feynman and A. R. Hibbs, *Path integrals and quantum mechanics*, McGraw, New York (1965).

[130] Nicholas Metropolis, Arianna W. Rosenbluth, Marshall N. Rosenbluth, Augusta H. Teller, and Edward Teller, *Equation of state calculations by fast computing machines*, The journal of chemical physics **21** (1953), no. 6, 1087–1092.

[131] Michele Ceriotti, Giovanni Bussi, and Michele Parrinello, *Langevin equation with colored noise for constant-temperature molecular dynamics simulations*, Phys. Rev. Lett. **102** (2009), 020601.

[132] Michele Ceriotti, Giovanni Bussi, and Michele Parrinello, *Colored-noise thermostats a la carte*, Journal of Chemical Theory and Computation **6** (2010), no. 4, 1170–1180.

[133] Don S. Lemons and Anthony Gythiel, *Paul Langevin's 1908 paper "On the Theory of Brownian Motion" ["Sur la théorie du mouvement brownien," C. R. Acad. Sci. (Paris) 146, 530–533 (1908)]*, American Journal of Physics **65** (1997), no. 11, 1079–1081.

[134] T. Schneider and E. Stoll, *Molecular-dynamics study of a three-dimensional one-component model for distortive phase transitions*, Physical Review B **17** (1978), no. 3, 1302.

[135] Michele Ceriotti, Giovanni Bussi, and Michele Parrinello, *Nuclear quantum effects in solids using a colored-noise thermostat*, Phys. Rev. Lett. **103** (2009), 030603.

[136] Michele Ceriotti, Michele Parrinello, Thomas E. Markland, and David E. Manolopoulos, *Efficient stochastic thermostatting of path integral molecular dynamics*, The Journal of Chemical Physics **133** (2010), no. 12, 124104.

[137] Michele Ceriotti, David E. Manolopoulos, and Michele Parrinello, *Accelerating the convergence of path integral dynamics with a generalized langevin equation*, The Journal of Chemical Physics **134** (2011), no. 8, 084104.

[138] M. F. Herman, E. J. Bruskin, and B. J. Berne, *On path integral Monte Carlo simulations*, The Journal of Chemical Physics **76** (1982), no. 10, 5150–5155.

[139] D. M. Ceperley, *Path integrals in the theory of condensed helium*, Rev. Mod. Phys. **67** (1995), 279–355.

[140] Michele Ceriotti and David E. Manolopoulos, *Efficient first-principles calculation of the quantum kinetic energy and momentum distribution of nuclei*, Phys. Rev. Lett. **109** (2012), 100604.

[141] Thomas E. Markland and David E. Manolopoulos, *An efficient ring polymer contraction scheme for imaginary time path integral simulations*, The Journal of Chemical Physics **129** (2008), no. 2, 024105.

[142] Thomas E. Markland and David E. Manolopoulos, *A refined ring polymer contraction scheme for systems with electrostatic interactions*, Chemical Physics Letters **464** (2008), no. 4-6, 256–261.

[143] Yair Litman, Davide Donadio, Michele Ceriotti, and Mariana Rossi, *Decisive role of nuclear quantum effects on surface mediated water dissociation at finite temperature*, The Journal of Chemical Physics **148** (2018), no. 10, 102320.

[144] W. B. Streett, D. J. Tildesley, and G. Saville, *Multiple time-step methods in molecular dynamics*, Molecular Physics **35** (1978), no. 3, 639–648.

[145] Mark Tuckerman, Bruce J. Berne, and Glenn J. Martyna, *Reversible multiple time scale molecular dynamics*, The Journal of chemical physics **97** (1992), no. 3, 1990–2001.

[146] Pierre Simon Laplace, *Memoir on the probability of the causes of events (translation from French)*, Statistical science **1** (1986), no. 3, 364–378.

[147] Jacobus Henricus Van 't Hoff, *Etudes de dynamique chimique*, vol. 1, Frederik Muller & Co., 1884.

[148] Svante Arrhenius, *Über die dissociationswärme und den einfluss der temperatur auf den dissociationsgrad der elektrolyte*, Zeitschrift für physikalische Chemie **4** (1889), no. 1, 96–116.

[149] J. Pancíř, *Calculation of the least energy path on the energy hypersurface*, Collection of Czechoslovak Chemical Communications **40** (1975), no. 4, 1112–1118.

[150] Charles J. Cerjan and William H. Miller, *On finding transition states*, The Journal of Chemical Physics **75** (1981), no. 6, 2800–2806.

[151] Graeme Henkelman and Hannes Jónsson, *A dimer method for finding saddle points on high dimensional potential surfaces using only first derivatives*, The Journal of Chemical Physics **111** (1999), no. 15, 7010–7022.

[152] Hannes Jónsson, Greg Mills, and Karsten W. Jacobsen, *Nudged elastic band method for finding minimum energy paths of transitions*, (1998).

[153] Graeme Henkelman, Blas P. Uberuaga, and Hannes Jónsson, *A climbing image nudged elastic band method for finding saddle points and minimum energy paths*, The Journal of chemical physics **113** (2000), no. 22, 9901–9904.

[154] Graeme Henkelman and Hannes Jónsson, *Improved tangent estimate in the nudged elastic band method for finding minimum energy paths and saddle points*, The Journal of chemical physics **113** (2000), no. 22, 9978–9985.

[155] Jhih-Wei Chu, Bernhardt L. Trout, and Bernard R. Brooks, *A super-linear minimization scheme for the nudged elastic band method*, The Journal of chemical physics **119** (2003), no. 24, 12708–12717.

[156] P. Maragakis, Stefan A. Andreev, Yisroel Brumer, David R. Reichman, and Efthimios Kaxiras, *Adaptive nudged elastic band approach for transition state calculation*, The Journal of Chemical Physics **117** (2002), no. 10, 4651–4658.

[157] Esben L. Kolsbjerg, Michael N. Groves, and Bjørk Hammer, *An automated nudged elastic band method*, The Journal of chemical physics **145** (2016), no. 9, 094107.

[158] Vilhjálmur Ásgeirsson, Benedikt Orri Birgisson, Ragnar Bjornsson, Ute Becker, Frank Neese, Christoph Riplinger, and Hannes Jónsson, *Nudged elastic band method for molecular reactions using energy-weighted springs combined with eigenvector following*, Journal of Chemical Theory and Computation **17** (2021), no. 8, 4929–4945, PMID: 34275279.

[159] Davide Mandelli and Michele Parrinello, *A modified nudged elastic band algorithm with adaptive spring lengths*, The Journal of Chemical Physics **155** (2021), no. 7, 074103.

[160] E Weinan, Weiqing Ren, and Eric Vanden-Eijnden, *String method for the study of rare events*, Physical Review B **66** (2002), no. 5, 052301.

[161] E Weinan, Weiqing Ren, and Eric Vanden-Eijnden, *Simplified and improved string method for computing the minimum energy paths in barrier-crossing events*, Journal of Chemical Physics **126** (2007), no. 16, 164103.

[162] Daniel Sheppard, Rye Terrell, and Graeme Henkelman, *Optimization methods for finding minimum energy paths*, The Journal of Chemical Physics **128** (2008), no. 13, 134106.

[163] Li Xie, Haiyan Liu, and Weitao Yang, *Adapting the nudged elastic band method for determining minimum-energy paths of chemical reactions in enzymes*, The Journal of chemical physics **120** (2004), no. 17, 8039–8052.

[164] José A. Garrido Torres, Paul C. Jennings, Martin H. Hansen, Jacob R. Boes, and Thomas Bligaard, *Low-scaling algorithm for nudged elastic band calculations using a surrogate machine learning model*, Physical review letters **122** (2019), no. 15, 156001.

[165] Jorge Nocedal and Stephen J. Wright, *Numerical optimization*, Springer New York, NY, 1999.

[166] Erik Bitzek, Pekka Koskinen, Franz Gähler, Michael Moseler, and Peter Gumbsch, *Structural relaxation made simple*, Phys. Rev. Lett. **97** (2006), 170201.

[167] Feliciano Giustino, *Electron-phonon interactions from first principles*, Reviews Of Modern Physics **89** (2017), no. 1, 015003.

[168] Takanori Koitaya and Jun Yoshinobu, *The quantum nature of C–H···metal interaction: Vibrational spectra and kinetic and geometric isotope effects of adsorbed cyclohexane*, The Chemical Record **14** (2014), no. 5, 848–856.

[169] Yoshitada Morikawa, Hisao Ishii, and Kazuhiko Seki, *Theoretical study of n-alkane adsorption on metal surfaces*, Phys. Rev. B **69** (2004), 041403.

[170] Matheus Jacobs, Jannis Krumland, Ana M. Valencia, Haiyuan Wang, Mariana Rossi, and Caterina Cocchi, *Ultrafast charge transfer and vibronic coupling in a laser-excited hybrid inorganic/organic interface*, Advances in Physics: X **5** (2020), no. 1, 1749883.

[171] Christopher E. Patrick and Feliciano Giustino, *Unified theory of electron-phonon renormalization and phonon-assisted optical absorption*, Journal of Physics: Condensed Matter **26** (2014), no. 36, 365503.

[172] Anna Kaczmarek, Motoyuki Shiga, and Dominik Marx, *Quantum effects on vibrational and electronic spectra of hydrazine studied by "on-the-fly" ab initio ring polymer molecular dynamics*, The Journal of Physical Chemistry A **113** (2009), no. 10, 1985–1994, PMID: 19199678.

[173] Wei Chen, Francesco Ambrosio, Giacomo Miceli, and Alfredo Pasquarello, *Ab initio electronic structure of liquid water*, Phys. Rev. Lett. **117** (2016), 186401.

[174] Yu Kay Law and Ali A. Hassanali, *Role of quantum vibrations on the structural, electronic, and optical properties of 9-methylguanine*, The Journal of Physical Chemistry A **119** (2015), no. 44, 10816–10827, PMID: 26444383.

[175] Takanori Koitaya, Kozo Mukai, Shinya Yoshimoto, and Jun Yoshinobu, *Energy level alignment of cyclohexane on Rh(111) surfaces: The importance of interfacial dipole and final-state screening*, The Journal of Chemical Physics **138** (2013), no. 4, 044702.

[176] K.-P. Bohnen, A. Eichler, and J. Hafner, *First principles calculations of surface phonons on rh(111)*, Surface Science **368** (1996), no. 1, 222 – 225, Vibrations at Surfaces.

[177] J. W. Arblaster, *Crystallographic properties of rhodium*, Platinum Metals Review **41** (1997), no. 4, 184–189.

[178] A. Togo and I. Tanaka, *First principles phonon calculations in materials science*, Scr. Mater. **108** (2015), 1–5.

[179] Karen Fidanyan, *Modified Phonopy-FHI-aims interface*, `https://github.com/fidanyan/phonopy`, 2019, Accessed: 2022-07-01.

[180] Laboratory of Computational Science and Modelling, EPFL Lausanne, Switzerland, *GLE4MD*, `http://gle4md.org`, Accessed: 2022-08-31.

[181] K. Wandelt and J. E. Hulse, *Xenon adsorption on palladium. I. The homogeneous (110), (100), and (111) surfaces*, The Journal of Chemical Physics **80** (1984), no. 3, 1340–1352.

[182] Paul S. Bagus, Klaus Hermann, and Christof Wöll, *The interaction of C6H6 and C6H12 with noble metal surfaces: Electronic level alignment and the origin of the interface dipole*, The Journal of Chemical Physics **123** (2005), no. 18, 184109.

[183] Florian Knoop, Thomas A. R. Purcell, Matthias Scheffler, and Christian Carbogno, *Anharmonicity measure for materials*, Phys. Rev. Materials **4** (2020), 083809.

[184] J. B. Neaton, Mark S. Hybertsen, and Steven G. Louie, *Renormalization of molecular electronic levels at metal-molecule interfaces*, Phys. Rev. Lett. **97** (2006), 216405.

[185] J. M. Garcia-Lastra, C. Rostgaard, A. Rubio, and K. S. Thygesen, *Polarization-induced renormalization of molecular levels at metallic and semiconducting surfaces*, Phys. Rev. B **80** (2009), 245427.

[186] Reinhard J. Maurer, Victor G. Ruiz, Javier Camarillo-Cisneros, Wei Liu, Nicola Ferri, Karsten Reuter, and Alexandre Tkatchenko, *Adsorption structures and energetics of molecules on metal surfaces: Bridging experiment and theory*, Progress in Surface Science **91** (2016), no. 2, 72 – 100.

[187] Andrea Grisafi and Michele Ceriotti, *Incorporating long-range physics in atomic-scale machine learning*, The Journal of Chemical Physics **151** (2019), no. 20, 204105.

[188] Zhen-Fei Liu, David A. Egger, Sivan Refaely-Abramson, Leeor Kronik, and Jeffrey B. Neaton, *Energy level alignment at molecule-metal interfaces from an optimally tuned range-separated hybrid functional*, The Journal of Chemical Physics **146** (2017), no. 9, 092326.

[189] Oliver T. Hofmann, Viktor Atalla, Nikolaj Moll, Patrick Rinke, and Matthias Scheffler, *Interface dipoles of organic molecules on Ag(111) in hybrid density-functional theory*, New Journal of Physics **15** (2013), no. 12, 123028.

[190] Michael F. Toney, Jason N. Howard, Jocelyn Richer, Gary L. Borges, Joseph G. Gordon, Owen R. Melroy, David G. Wiesler, Dennis Yee, and Larry B. Sorensen, *Voltage-dependent ordering of water molecules at an electrode–electrolyte interface*, Nature **368** (1994), no. 6470, 444–446.

[191] Yujin Tong, François Lapointe, Martin Thämer, Martin Wolf, and R. Kramer Campen, *Hydrophobic water probed experimentally at the gold electrode/aqueous interface*, Angewandte Chemie International Edition **56** (2017), no. 15, 4211–4214.

[192] Javier Carrasco, Jiří Klimeš, and Angelos Michaelides, *The role of van der Waals forces in water adsorption on metals*, The Journal of Chemical Physics **138** (2013), no. 2, 024708.

[193] Michele Ceriotti, Wei Fang, Peter G. Kusalik, Ross H. McKenzie, Angelos Michaelides, Miguel A. Morales, and Thomas E. Markland, *Nuclear quantum effects in water and aqueous systems: Experiment, theory, and current challenges*, Chemical Reviews **116** (2016), no. 13, 7529–7550, PMID: 27049513.

[194] K. Laasonen, M. Sprik, M. Parrinello, and R. Car, *"Ab initio" liquid water*, The Journal of chemical physics **99** (1993), no. 11, 9080–9089.

[195] Dominik Marx, Mark E. Tuckerman, Jürg Hutter, and Michele Parrinello, *The nature of the hydrated excess proton in water*, Nature **397** (1999), no. 6720, 601–604.

[196] Dominik Marx, Mark E. Tuckerman, and Michele Parrinello, *Solvated excess protons in water: quantum effects on the hydration structure*, Journal of Physics: Condensed Matter **12** (2000), no. 8A, A153–A159.

[197] Sergei D. Ivanov, Alexander Witt, Motoyuki Shiga, and Dominik Marx, *Communications: On artificial frequency shifts in infrared spectra obtained from centroid molecular dynamics: Quantum liquid water*, The Journal of chemical physics **132** (2010), no. 3, 031101.

[198] Sergei Izvekov and Gregory A. Voth, *Ab initio molecular dynamics simulation of the Ag(111)-water interface*, The Journal of Chemical Physics **115** (2001), no. 15, 7196–7206.

[199] Axel Groß and Sung Sakong, *Ab initio simulations of water/metal interfaces*, Chemical Reviews **122** (2022), no. 12, 10746–10776.

[200] Gui-Chang Wang, Shu-Xia Tao, and Xian-He Bu, *A systematic theoretical study of water dissociation on clean and oxygen-preadsorbed transition metals*, Journal of Catalysis **244** (2006), no. 1, 10–16.

[201] Yilin Cao and Zhao-Xu Chen, *Theoretical studies on the adsorption and decomposition of H2O on Pd(111) surface*, Surface Science **600** (2006), no. 19, 4572–4583.

[202] Abhijit A. Phatak, W. Nicholas Delgass, Fabio H. Ribeiro, and William F. Schneider, *Density functional theory comparison of water dissociation steps on Cu, Au, Ni, Pd, and Pt*, The Journal of Physical chemistry c **113** (2009), no. 17, 7269–7276.

[203] José L. C. Fajín, M. Natália D. S. Cordeiro, Francesc Illas, and José R. B. Gomes, *Descriptors controlling the catalytic activity of metallic surfaces toward water splitting*, Journal of Catalysis **276** (2010), no. 1, 92–100.

[204] Osamu Sugino, Ikutaro Hamada, Minoru Otani, Yoshitada Morikawa, Tamio Ikeshoji, and Yasuharu Okamoto, *First-principles molecular dynamics simulation of biased electrode/solution interface*, Surface Science **601** (2007), no. 22, 5237–5240.

[205] Minoru Otani, Ikutaro Hamada, Osamu Sugino, Yoshitada Morikawa, Yasuharu Okamoto, and Tamio Ikeshoji, *Structure of the water/platinum interface – a first principles simulation under bias potential*, Physical Chemistry Chemical Physics **10** (2008), no. 25, 3609–3612.

[206] Tamio Ikeshoji, Minoru Otani, Ikutaro Hamada, and Yasuharu Okamoto, *Reversible redox reaction and water configuration on a positively charged platinum surface: first principles molecular dynamics simulation*, Phys. Chem. Chem. Phys. **13** (2011), 20223–20227.

[207] Yumin Qian, Ikutaro Hamada, Minoru Otani, and Tamio Ikeshoji, *Inhibition of water dissociation on a pitted Pt(111) surface: First principles study*, Catalysis Today **202** (2013), 163–167, Electrocatalysis.

[208] Steffen Wilke, Morrel H. Cohen, and Matthias Scheffler, *Local isoelectronic reactivity of solid surfaces*, Phys. Rev. Lett. **77** (1996), 1560–1563.

[209] Ralph G. Pearson, *Acids and bases: Hard acids prefer to associate with hard bases, and soft acids prefer to associate with soft bases.*, Science **151** (1966), no. 3707, 172–177.

[210] A. Michaelides, V. A. Ranea, P. L. de Andres, and D. A. King, *General model for water monomer adsorption on close-packed transition and noble metal surfaces*, Phys. Rev. Lett. **90** (2003), 216102.

[211] R. S. Mulliken, *Electronic population analysis on LCAO–MO molecular wave functions. II. Overlap populations, bond orders, and covalent bond energies*, The Journal of Chemical Physics **23** (1955), no. 10, 1841–1846.

[212] G. P. Kerker, *Efficient iteration scheme for self-consistent pseudopotential calculations*, Physical Review B **23** (1981), no. 6, 3082.

Declaration of Authorship

I declare that I have completed the thesis independently using only the aids and tools specified. I have not applied for a doctor's degree in the doctoral subject elsewhere and do not hold a corresponding doctor's degree. I have taken due note of the Faculty of Mathematics and Natural Sciences PhD Regulations, published in the Official Gazette of Humboldt-Universität zu Berlin no. 42/2018 on 11/07/2018.

Hamburg, September 27, 2022